

# Constraints on the behavior of trace elements in the actively-forming TAG deposit, Mid-Atlantic Ridge, based on LA-ICP-MS analyses of pyrite

Hannah L.J. Grant<sup>a,\*</sup>, Mark D. Hannington<sup>a,b</sup>, Sven Petersen<sup>a</sup>, Matthias Frische<sup>a</sup>, Sebastian H. Fuchs<sup>a</sup>

<sup>a</sup> GEOMAR Helmholtz Center for Ocean Research Kiel, Wischhofstrasse 1-3, 24148 Kiel, Germany

<sup>b</sup> Department of Earth and Environmental Sciences, University of Ottawa, Advanced Research Complex, 25 Templeton Street, Ottawa K1N 6N5, Canada



## ARTICLE INFO

Editor: D.B. Dingwell

### Keywords:

TAG deposit

Pyrite

Trace elements

Seafloor massive sulfides

Laser ablation ICP-MS

Hydrothermal fluid

## ABSTRACT

The distribution of trace ore elements in different paragenetic stages of pyrite has been documented for the first time in the sub-seafloor of the actively-forming TAG massive sulfide deposit. Trace element distributions have been determined by in-situ laser ablation inductively-coupled plasma mass spectrometry (LA-ICP-MS) of pyrite formed at different stages of mineralization, and at different temperatures constrained by previously published fluid inclusion analyses. The data reveal a strong dependence on paragenetic stage, with distinct low- and high-temperature enrichments. Porous pyrite (and marcasite) formed at low temperatures ( $< 300\text{ }^{\circ}\text{C}$ ) in the outer margins of the deposit is enriched in As, Ag, Tl, Pb, Sb, Mo, W, Zn, Ga, Ge, Cd, In, Te, Au, Mn, V, and U. Coarse-grained pyrite formed at higher temperatures ( $> 350\text{ }^{\circ}\text{C}$ ) at the base of the hydrothermal mound and in the stockwork zone is enriched in Co, Se, Bi, Cu, Ni, and Sn. A number of different sub-types of pyrite also have characteristic trace element signatures; e.g., the earliest pyrite formed at the highest temperatures is always enriched in Co and Se compared to later stages. Ablation profiles for Co, Se, and Ni are smooth and indicate that these elements are present mainly in lattice substitutions rather than as inclusions of other sulfides. Profiles for As, Sb, Tl, and Cu can be either irregular or smooth, indicating both lattice substitutions and inclusions. Lead and Ag have mostly smooth profiles, but because Pb cannot substitute directly into the pyrite lattice, it is interpreted to be present as homogeneously distributed micro- or nano-scale particles. The behavior of the different trace elements mainly reflects their aqueous speciation in the hydrothermal fluids at different temperatures, and for some elements like Co and Se, strong partitioning into the pyrite lattice at elevated temperatures. Adsorption onto pyrite surfaces controls the distribution of a number of redox-sensitive elements (i.e., Mo, V, Ni, U), particularly in the upper part of the mound which is infiltrated by cold seawater. Where micro- or nano-scale inclusions of chalcopyrite, sphalerite, galena, or sulfosalts are present, there is still a strong temperature dependence on the inclusion population (e.g., more abundant chalcopyrite in the highest-temperature pyrite), suggesting that the inclusions were co-precipitated with pyrite rather than overgrown. However, at the deposit scale, the trace element distributions are also strongly controlled by remobilization and chemical zone refining, as previously documented in bulk geochemical profiles.

The results show that pyrite chemistry is a remarkably good model of the chemistry of the entire hydrothermal system. For many trace elements, the concentrations in pyrite are highly predictive in terms of the conditions of mineral formation over a wide range of temperatures, from the stockwork zone to the cooler outer margins of the deposit. Calculated minimum concentrations of the trace elements in the fluids needed to account for the observed concentrations in pyrite show good agreement with measured vent fluid concentrations, particularly Pb, As, Mo, Ag, and Tl. However, significantly higher concentrations are indicated for Co (and Se) than have been measured in sampled fluids, confirming the strong partitioning of these elements into high-temperature pyrite.

\* Corresponding author at: British Geological Survey, The Lyell Centre, Research Avenue South, Edinburgh, EH14 4AP, United Kingdom.

E-mail address: [hgrant@bgs.ac.uk](mailto:hgrant@bgs.ac.uk) (H.L.J. Grant).

<https://doi.org/10.1016/j.chemgeo.2018.08.019>

Received 1 June 2018; Received in revised form 13 July 2018; Accepted 24 August 2018

Available online 07 September 2018

0009-2541/ © 2018 The Authors. Published by Elsevier B.V. This is an open access article under the CC BY license (<http://creativecommons.org/licenses/by/4.0/>).

## 1. Introduction

With the widespread availability of multi-element ICP-MS data, we now know a lot about the trace ore elements in different deposit types. However, we still lack reliable models of enrichments or depletions that can be directly linked to primary depositional conditions. A growing number of studies have employed high-resolution laser ablation inductively-coupled plasma mass spectrometry (LA-ICP-MS) to determine the trace element concentrations in sulfide minerals, including many studies of volcanogenic massive sulfide (VMS) deposits (Leistel et al., 1998; Slack et al., 2005; Cook et al., 2009; Maslennikov et al., 2009, 2013; McClenaghan et al., 2009; Craddock and Bach, 2010; Dusel-Bacon et al., 2011; Ye et al., 2011; Lockington et al., 2014; Revan et al., 2014; Wohlgemuth-Ueberwasser et al., 2014; Genna and Gaboury, 2015; George et al., 2015; Belousov et al., 2016; Maslennikov et al., 2017; Dehnavi et al., 2018). Large amounts of complex data are often reported, but only a fraction can be confidently explained in terms of systematic behavior of the trace elements (e.g., Cook, 1996; Cook et al., 2009). At the same time, the manner in which trace elements occur in the host minerals (e.g., in solid solution, as submicroscopic mineral inclusions, or adsorbed onto sulfide surfaces) is often poorly constrained. Temperature-dependent partitioning between the aqueous fluid and mineral is widely cited (e.g., McIntire, 1963; Loftus-Hills and Solomon, 1967; Scott and Barnes, 1971; Auclair and Fouquet, 1987; Huston et al., 1995; Cook, 1996; Craig et al., 1998; Hannington, 2014; Seward et al., 2014), but there are few well-known or experimentally calibrated substitutions – far fewer than the number of elements that can now be analyzed by LA-ICP-MS. If the partition coefficients are very large or very small, the concentrations of the trace elements in the minerals are unlikely to be an accurate reflection of the concentrations in the fluids (e.g., Cd in sphalerite: Cook et al., 2009). In many deposits, significant modification of primary trace element distributions also can result from hydrothermal reworking, recrystallization, and metamorphism. This makes interpretation of the trace element distributions in terms of aqueous fluid-mineral equilibria difficult for most of the periodic table.

Access to vent fluids in active seafloor hydrothermal systems is now showing the most important influences on trace element distributions, including redox conditions, pH, enriched sources of elements, the availability of ligands for complexing, and the influence of processes such as phase separation, volatile partitioning, and direct magmatic contributions (Von Damm, 1990; Hannington, 2014). However, comprehensive data sets, especially for trace metals, are rare (e.g., Metz and Trefry, 2000). Several studies have explored what can be learned from LA-ICP-MS on sulfide minerals from seafloor vents (e.g., Halbach et al., 1998; Butler and Nesbitt, 1999; Houghton et al., 2004; Bogdanov et al., 2008; Lein et al., 2010; Li et al., 2012; Melekestseva et al., 2014; Wohlgemuth-Ueberwasser et al., 2015; Keith et al., 2016; Maslennikov et al., 2017; Melekestseva et al., 2017; Wang et al., 2017; Dekov et al., 2018; Yuan et al., 2018), but few have linked the trace element behavior to the compositions of the vent fluids or the complex mineral paragenesis of evolving systems from the underlying stockwork zone to the seafloor hydrothermal mound. Questions remain about the role of temperature-dependent mineral solubilities, mineral zoning, zone refining, primary versus diagenetic and secondary enrichments, inheritance of trace element fingerprints during replacement or recrystallization, and what mechanisms are most important for incorporation of trace elements in mineral lattices.

To investigate some of these questions, we analyzed sulfides from ODP drill holes through the actively-forming Trans-Atlantic Geotraverse (TAG) deposit on the Mid-Atlantic Ridge. We focused on pyrite as a phase that is present in all parts of the deposit and has formed under a range of different but well-constrained conditions from low to high temperatures. Using LA-ICP-MS we were able to analyze texturally complex and compositionally variable pyrite grains from multiple episodes of deposit growth. Co-existing marcasite, sphalerite, and chalcopyrite were also analyzed. We show that systematic behavior of trace elements in pyrite is closely linked to primary depositional conditions and hydrothermal fluid compositions in a predictive way that can also inform the interpretation of trace element distribution in ancient VMS deposits.

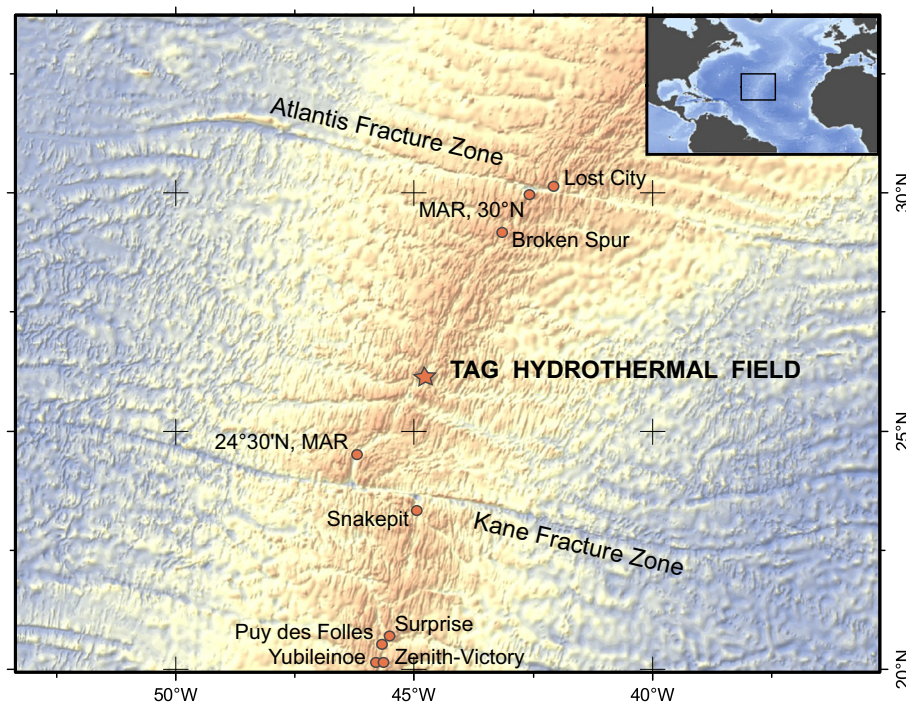


**Fig. 1.** Bathymetry of the TAG segment of the Mid-Atlantic Ridge. The star indicates the location of the TAG hydrothermal field. Other vent fields and sulfide deposits in the region are also shown. Bathymetry is from GeoMapApp (2017), and hydrothermal vent locations from Beaulieu et al. (2013) and Beltenev et al. (2017).

## 2. TAG hydrothermal mound

The TAG hydrothermal mound is located at 26°08.2'N, 44°49.6'W on the TAG segment of the Mid-Atlantic Ridge (Fig. 1). The 40 km-long TAG segment is 9 km wide and > 4200 m deep at its northern and southern ends, narrowing to 6 km and 3600 m deep on a central high at 26°10'N (Rona, 1980; Sempere et al., 1990). The rift valley is asymmetrical with the higher and steeper eastern wall rising through a series of benches bounded by steep, westward-dipping faults up to 1 km long and several hundred meters wide (Thompson et al., 1985; Tivey et al., 2003). The TAG hydrothermal field covers an area of at least 5 km by 5 km close to the eastern wall of the central axial valley and is located on the hanging wall of an active detachment fault (Humphris et al., 2015). It was discovered in 1972 during the NOAA Trans-Atlantic Geotraverse project (Scott et al., 1974) and is one of the most comprehensively studied seafloor hydrothermal systems (Thompson et al., 1985; Lisitsin et al., 1989; Zonenshain et al., 1989; Purdy et al., 1990; Rona et al., 1993a, 1993b; Edmond et al., 1995; Krasnov et al., 1995; Edmonds et al., 1996; Gamo et al., 1996; Humphris et al., 1995a; Reves-Sohn et al., 2004; Roman and Singh, 2007; Pontbriand and Sohn, 2014). Three main areas of past and present hydrothermal activity have been mapped: low-temperature venting and Mn- and Fe-oxide deposits on the eastern rift valley wall (2400 to 3100 m: Scott et al., 1974), relict massive sulfide mounds (*Mir* and *Alvin* zones at 3400 to 3600 m: Rona et al., 1993b), and the currently active high-temperature mound on the rift valley floor (3620–3700 m: Humphris et al., 1995a). The earliest hydrothermal activity in the TAG field is represented by low-temperature Mn-oxides having a minimum age of 125,000 years (Lalou et al., 1993). High-temperature hydrothermal activity in the relict *Mir* zone began approximately 100,000 years ago (Lalou et al., 1993). The presently active mound began forming about 40,000 to 50,000 years ago on 100,000-year-old crust (Lalou et al., 1998). Distinct pulses of high-temperature activity, every 5000 to 6000 years over the past 20,000 years, are recorded by U-Th ages in mound talus; between these pulses, the mound cooled completely (Rona et al., 1993a). Dating of chimney sulfides indicates the latest reactivation of high-temperature venting began ~70 years ago after a hiatus of 4000 years (Lalou et al., 1998).

The active mound is roughly circular, and measures 200 m in diameter and about 50 m in height (Fig. 2). Two distinct terraces at 3642–3650 m and 3650–3655 m water depth are interpreted to represent separate phases of mound growth (Humphris and Kleinrock,

1996; Kleinrock et al., 1996; Humphris and Tivey, 2000). The actively venting high-temperature Black Smoker Complex (BSC) sits on a 23 m-wide and 10 m-high cone consisting of brecciated blocks of massive pyrite, chalcopyrite and anhydrite surrounded by talus from the frequent collapse of sulfide chimneys (Thompson et al., 1985; Rona et al., 1993a; Humphris et al., 1995a). The margins of the active mound are steep-sided slopes up to 20 m high and are partially covered and surrounded by an apron of oxidized sulfide debris flow, pyrite-rich blocky talus, and metalliferous sediment (German et al., 1993; Rona et al., 1993a; Hannington et al., 1998a).

Two distinct but related fluids currently exit the mound, with compositions that have remained stable over several decades (Campbell et al., 1988; Edmond et al., 1995; Edmonds et al., 1996; Gamo et al., 1996; James and Elderfield, 1996; Metz and Trefry, 2000). High-temperature venting up to 370 °C is concentrated at the BSC (Tivey et al., 1995; Edmond et al., 1995; Parker and von Damm, 2005). However, other isolated occurrences of black smoker fluid venting indicate that high-temperature upflow is not restricted only to the BSC (Kleinrock et al., 1996). White smoker, Zn-rich fluids previously were venting from beehive-like chimneys in the 'Kremlin Area', approximately 70 m to the southeast of the BSC on the lower terrace (Edmond et al., 1995); they have now ceased venting (Sohn, 2007). The white smoker fluids were 60° to 90 °C cooler than the black smoker fluids, more acidic, and less Fe- and H<sub>2</sub>S-rich. They were considered to be products of mixing between black smoker fluid and seawater, with precipitation of Fe-sulfide within the mound accounting for the low Fe, H<sub>2</sub>S, and pH (Edmonds et al., 1996; Tivey et al., 1998). Diffuse flow of low-temperature (up to 50 °C) fluid is occurring through much of the mound surface and the surrounding sediment apron (Becker and von Herzen, 1996).

The TAG deposit is the only sediment-free, basalt-hosted, active sulfide mound complex that has been drilled from the seafloor to the bottom of its stockwork zone (a depth of 125 m below seafloor: Humphris et al., 1995a). During ODP Leg 158, 17 holes were drilled at five locations across the active mound, designated TAG-1 to TAG-5 (Fig. 2). Core was recovered from 15 holes enabling the first three-dimensional reconstruction of the mound and sub-seafloor stockwork complex (Humphris et al., 1995b; Hannington et al., 1998a; Petersen et al., 2000). Fig. 3 is a composite section of the mound and stockwork zone showing the distribution of the different mineralized zones and the locations of the samples selected for this study. Based on the thickness of the sulfide zone and extent of the underlying stockwork mineralization, the deposit was estimated to contain 2.7 million metric tons

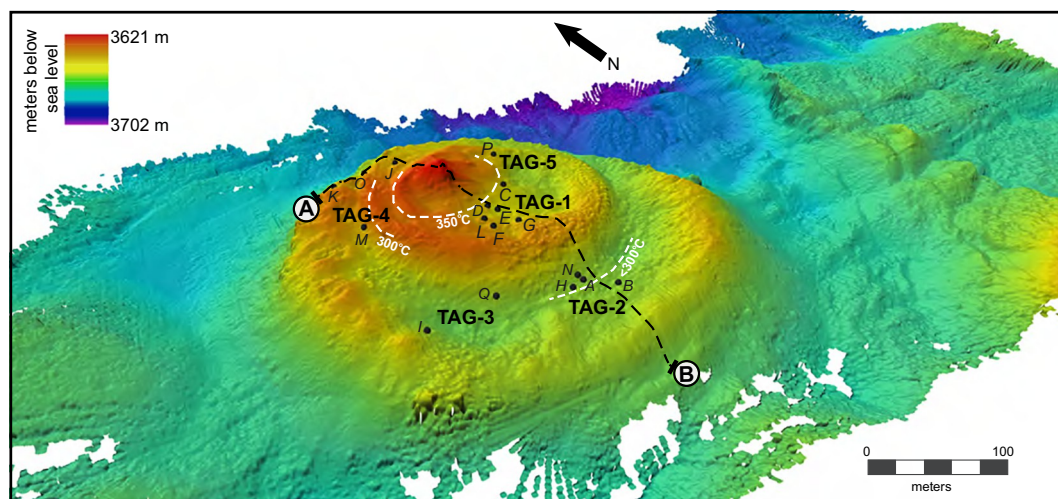


**Fig. 2.** Locations of ODP Leg 158 drill holes, with identifiers, on a bathymetric model of the TAG mound. The approximate location of the sub-seafloor cross section in Fig. 3 is shown by the black dashed line (A to B). The white dashed lines are approximate limits of temperature contours in Fig. 3. Bathymetric data (0.25 m grid resolution) is from Roman and Singh (2007) and retrieved from the Marine Geoscience Data System data repository ([www.marine-geo.org](http://www.marine-geo.org), 2017) via GeoMapApp ([www.geomapapp.org](http://www.geomapapp.org)).



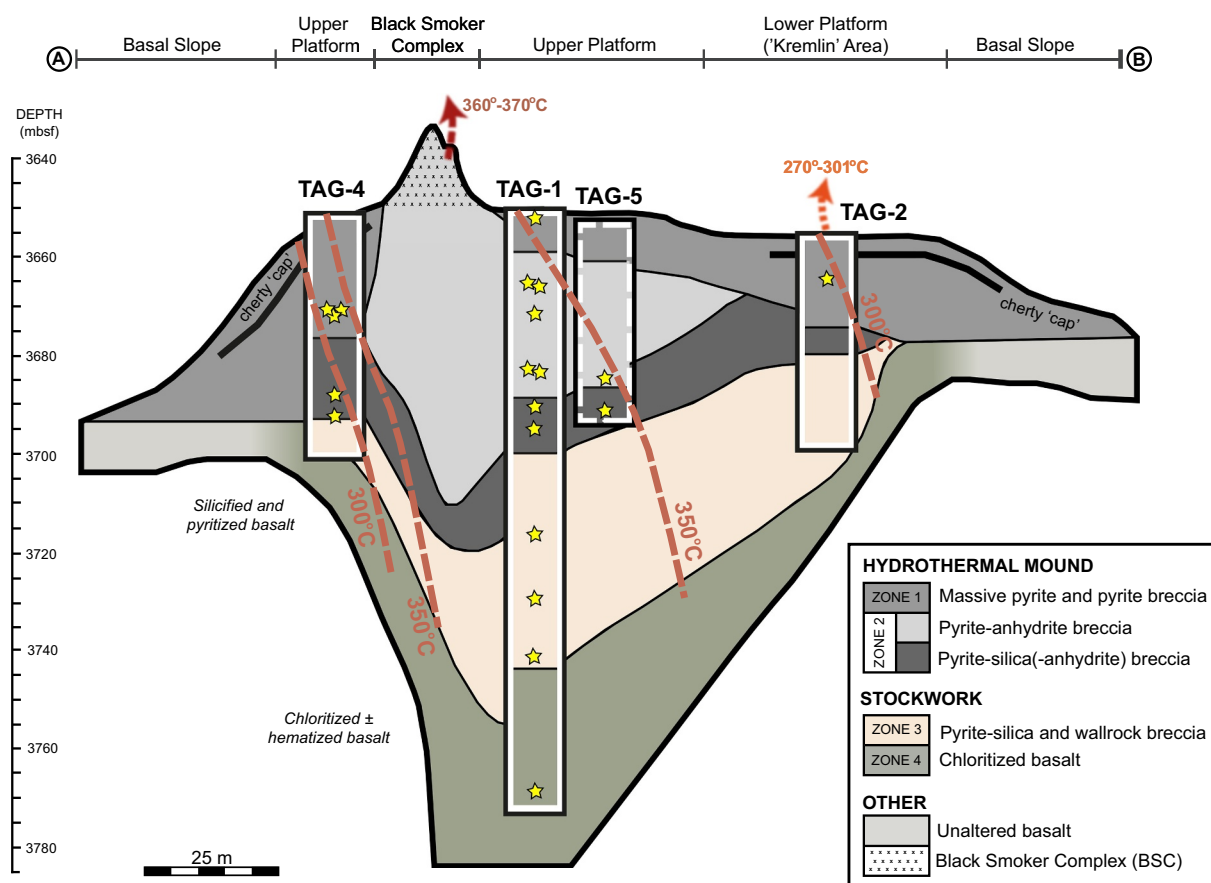


**Fig. 3.** A composite section of the internal structure of the active TAG mound and subsurface stockwork modified from Fouquet et al. (1998). The location of the section is shown in Fig. 2. TAG-5 (dashed outline) is projected onto this section. The depicted lithologies are summarized from multiple holes within each area. Yellow stars show locations of samples analyzed in this study. Different zones indicated in Table 1 are shown and include the following mineralization types (Humphries et al., 1996): massive pyrite and pyrite breccias (types 5 and 6); pyrite-anhydrite breccia (type 7); pyrite-silica (– anhydrite) breccia (type 8); pyrite-silica and wallrock breccias (type 9 and 10a); chloritized basalt (type 10b). Temperature contours are based on fluid inclusion data for quartz and anhydrite from Petersen et al. (1998, 2000) and Tivey et al. (1998); vent temperatures are from Edmond et al. (1995). The Kremlin area is now inactive. (For interpretation of the references to colour in this figure legend, the reader is referred to the web version of this article.)

(Mt) of massive and semi-massive sulfide (~2% Cu) in the mound and approximately 1.5 Mt. of mineralized breccias (~1% Cu) in the subsurface stockwork zone (Hannington et al., 1998a).

### 3. Mineralized zones

Details of the TAG drilling are summarized here from Humphris et al. (1995a), Humphries et al. (1995b), Fouquet et al. (1998), Knott et al. (1998), and Petersen et al. (1998, 2000). The deposit comprises four main zones, with a number of different mineralization types originally defined by Humphris and Kleinrock (1996) (Table 1). They comprise: i) a hydrothermally re-worked talus pile, ii) the hydrothermal mound, iii) the sub-seafloor stockwork, and iv) altered footwall. Each zone is dominated by one or more mineralization types (types 1–11) listed in Table 1. Zone 1 (0 to ~15 mbsf) consists of a thin layer of Fe-hydroxides and chert (types 1–4; Fig. 4a) overlying massive pyrite and massive pyrite breccias (types 5 and 6; Fig. 4b and c) with clasts up to 5 cm in a matrix of sandy, porous pyrite. This represents locally re-worked and partially cemented talus in the upper part of the hydrothermal mound. The core of the TAG mound (zone 2: ~15–45 mbsf) contains pyrite-anhydrite-breccia (type 7; Fig. 4d) to 30 mbsf with rounded pyrite clasts cemented by anhydrite. Between 30 and 45 mbsf, the pyrite-anhydrite breccia are strongly silicified (type 8; Fig. 4e) and include clasts of siliceous pyrite, quartz-pyrite aggregates, spongy pyrite, and granular pyrite in a quartz matrix. Anhydrite veins up to 45 cm in thickness (type 11) crosscut the breccia. Zone 3 (45–100 mbsf)

consists of pyrite-silica breccia (type 9; Fig. 4f) with gray fragments of variably mineralized and silicified wallrock and quartz-pyrite clasts in a matrix of fine-grained quartz. This represents the upper part of the quartz-rich stockwork underneath the hydrothermal mound and grades downward into silicified wallrock breccia (type 10a) containing clasts of basaltic fragments (up to 5 cm), recrystallized to quartz, pyrite and smectite (Fig. 4g). Zone 4, below 100 mbsf and to 125 mbsf, consists of altered basalt breccia (type 10b) including chloritized, paragonitized, and weakly mineralized basalt fragments up to 5 cm in size (Fig. 4h). These breccia have a matrix of quartz and pyrite, are crosscut by veins of pyrite, quartz and quartz + pyrite, and represent the lower part of the stockwork and upper hydrothermal upflow zone beneath the TAG mound.

#### 3.1. Sampled drill core

For this study we selected 20 samples from representative locations throughout the active mound and underlying stockwork zone in TAG areas 1, 2, 4, and 5. Six holes were drilled in the TAG-1 area approximately 20 m southeast of the BSC on the upper terrace of the mound, and penetrated through the sulfide mound into the stockwork zone to a maximum depth of 125 mbsf. We selected multiple samples of seven different mineralization types from TAG-1 composed of massive granular pyrite, and breccias of massive pyrite, pyrite-anhydrite, pyrite-anhydrite-silica, pyrite-silica, and silicified and chloritized wallrock (Table 3). Massive pyrite breccia, consisting of massive pyrite plus

**Table 1**  
Distribution of mineralization types in the TAG mound.

Zone	Mineralization types	Textural description	Sulfide minerals	Other minerals	TAG-1	TAG-2	TAG-3	TAG-4	TAG-5
0	1 Fe-oxides	Massive, friable, crustiform Fe-ox with high porosity	Trace sulfides	Fe-ox, am.Si	-	A,B	-	M	-
2	2 Red and gray chert	Cryptocrystalline qtz with fine-grained Fe-ox inclusions	Disseminated py (< 10%)	Fe-ox, am.Si, qtz, anh	-	A,B,H	Q	J,M	-
3	3 Gray silica	Massive, porous, fine-grained sil; locally cherty and with fine-grained inclusions of disseminated sulfides	Disseminated py (< 10%)	Fe-ox, am.Si, qtz	-	A,N	Q	M	-
4	4 Chert-sulfide bx	Clasts of red or gray chert and massive porous py in a fine-grained cherty matrix	py (> 50%) ± cpy	Fe-ox, am.Si, qtz	-	A	-	-	-
5	5 Massive sulfide (75% sulfides)	Fine-grained, dense, dendritic to colloform py, typically with > 20% pore space. Pyrite often recrystallized to coarse grained aggregates. Localized very-fine- to fine-grained porous cpy or coarse bladed cpy crystals	py (> 75%) ± sph ± cpy	am.Si, anh, qtz	C,E,F,G	A,B,H	Q	I,K,M	O,P
6	6 Massive py bx (> 75% py < 10% matrix)	Nodular py clasts in a porous, sandy py matrix with minor anh or sil matrix	py (> 75%) ± cpy	anh ± qtz	C,F,G	H	-	-	O,P
7	7 Massive py-anh bx with anh veins (> 10% anh matrix)	Angular fragments of nodular siliceous massive py in a matrix of anh	py (< 50–75%) ± cpy	anh, qtz	C,G	-	-	-	O,P
8	8 Py-sil-anh bx (> 10% qtz, anh matrix)	Qtz-py and gray siliceous clasts in a qtz-rich matrix with locally abundant anh veining	py (50–75%) ± cpy	qtz, anh	C	N	-	-	-
9	9 Py-sil bx	Gray nodular siliceous py clasts in a qtz matrix	py (50–75%) ± cpy	qtz, anh	C,E	H	-	I,K,M	O,P
10	10a Silicified wallrock bx	Coarse, siliceous wallrock fragments with disseminated py in a qtz-rich matrix	py (< 50%) ± cpy	qtz ± anh	C,E	H	-	M	P
4	10b Chloritized basalt bx	Coarse, chloritic basalt fragments; commonly with clay-altered rims	py (< 50%) ± cpy	qtz, chl, clays	E	-	-	M	-
-	11 Massive anh veins	Massive, banded or crustiform, medium- to coarse-grained anh containing py and minor cpy	py (> 20%), cpy (< 10%)	anh (> 75%)	C	-	-	-	O

Modified from ODP Leg 158 (Humphries et al., 1996). Letters refer to drillholes in Fig. 2. Abbreviations: py = pyrite, mc = marcasite, cpy = chalcopyrite, sph = sphalerite, anh = anhydrite, qtz = quartz, sil = silica, am.Si = amorphous silica, chl = chlorite, Fe-ox = Fe-oxides, bx = breccia. Excluding mineralization type 10 where the sub-types 10a and 10b represent distinctly different rock types, for discussion of this dataset, only the major mineralization type subdivisions detailed in Humphries et al. (1996) are utilized.

minor chalcopyrite and anhydrite (types 5–6), was sampled in the upper 15 m of TAG-1 core. Below 15 mbsf, three samples were selected to represent the dominant pyrite-anhydrite and matrix-supported pyrite-silica-anhydrite cemented breccias (type 7), which extend to 30 mbsf. Pyrite is commonly nodular (0.5–1.5 cm), reflecting in-situ pyrite nucleation and sequential growth producing a rounded morphology (Knott et al., 1998). Abundant pyrite and chalcopyrite in the core is associated with anhydrite veining, often as well-developed vein selvages. Below 30 mbsf, two samples of anhydrite-veined pyrite-silica breccia (type 8), one sample of pyrite-silica breccia (type 9), and a silicified wallrock breccia sample (type 10a) were selected to represent the dominant mineralization at the base of the anhydrite-rich core and the transition from the mound to seafloor stockwork. Below 45 mbsf, a pyrite-silica breccia (type 9), and two samples of silicified wallrock (type 10a) were selected to represent the transition from sulfide-bearing silicified wallrock into chloritized, silicified and pyritized wallrock breccias up to 100 mbsf. Anhydrite veining in these samples is associated with trace chalcopyrite and disseminated granular pyrite. Quartz and pyrite veining increases below 50 mbsf, and these minerals are the dominant vein fill to 100 mbsf. A chloritized wallrock sample (type 10b) from 116.17 mbsf was selected to represent the dominant chloritic and silicified wallrock below 100 mbsf which contains pyrite, quartz and quartz + pyrite veins, and minor disseminated pyrite.

Four holes were drilled next to the ‘Kremlin Area’ on the south-eastern part of the lower platform (TAG-2; Fig. 2). Hole 957H ended in silicified wallrock breccia at 54.5 mbsf, and 957B, the most south-easterly hole, ended in relatively unaltered basalt at 20 mbsf. We sampled clasts of massive porous pyrite-bearing chert from TAG-2 (type 2; Table 3). Surface and near-surface mineralization includes porous massive Zn-Fe sulfides and chimney fragments composed of sphalerite and silica. A hard cherty layer containing pyrite in a predominantly cherty matrix occurs in the top few meters of all TAG-2 holes but overall core recovery of this material was low (Humphries et al., 1995b). Massive pyrite breccias (type 5) with minor anhydrite cement and abundant gray and red chert clasts grade downhole into massive pyrite and porous, nodular pyrite breccias (type 6) by 20 mbsf. Between 20 and 30 mbsf, pyrite-silica breccias (types 8 and 9) and anhydrite veins increase in abundance. Below 30 mbsf, silicified wall rock breccia (type 10a) and chloritized basalt fragments are dominant to the bottom of the drill holes and resemble the upper part of the quartz-rich stockwork below 45 mbsf in TAG-1. Overall, there is less anhydrite veining than in drill holes from TAG-1 and TAG-5. Representative samples of each of these mineralization types were selected for study.

Four holes were drilled on the upper terrace (TAG-4; Fig. 2), 20–30 m west of the BSC through the sulfide mound, the stockwork zone, and into underlying slightly altered and chloritized basalt to a maximum depth of 51.2 mbsf. The hydrothermal mound in this area is approximately 30 m thick, and consists of sulfide-cemented talus adjacent to the main upflow zone. We sampled five distinct mineralization types from TAG-4 consisting of massive pyrite, porous massive pyrite, gray silica with fine-grained disseminated pyrite, and pyrite-silica breccia (Table 3). Core from the upper 10 m consists of in-situ massive sulfide crusts and sulfide-cemented breccias of massive porous pyrite, colloform marcasite, and sphalerite (type 5), plus red and gray chert clasts similar to those in drill holes from the same depth in the TAG-2 area. Sphalerite mainly occurs in the upper 5–10 m and sporadically to 15 mbsf. Chalcopyrite is rare. Abundant colloform pyrite and late-stage sphalerite are common in cavities and veins and are the main cement of the uppermost breccias. Below 10 mbsf, two samples of massive pyrite and porous massive pyrite were selected from massive pyrite and pyrite breccias containing minor sphalerite. These grade into pyrite-silica breccia (type 9) interspersed with sulfide-bearing chert, which are dominant at the base of the hydrothermal mound between 20 and 30 mbsf; one pyrite-silica breccia was selected to reflect this transition. Below 30 mbsf, two samples of sulfide-bearing chert (type 3) and

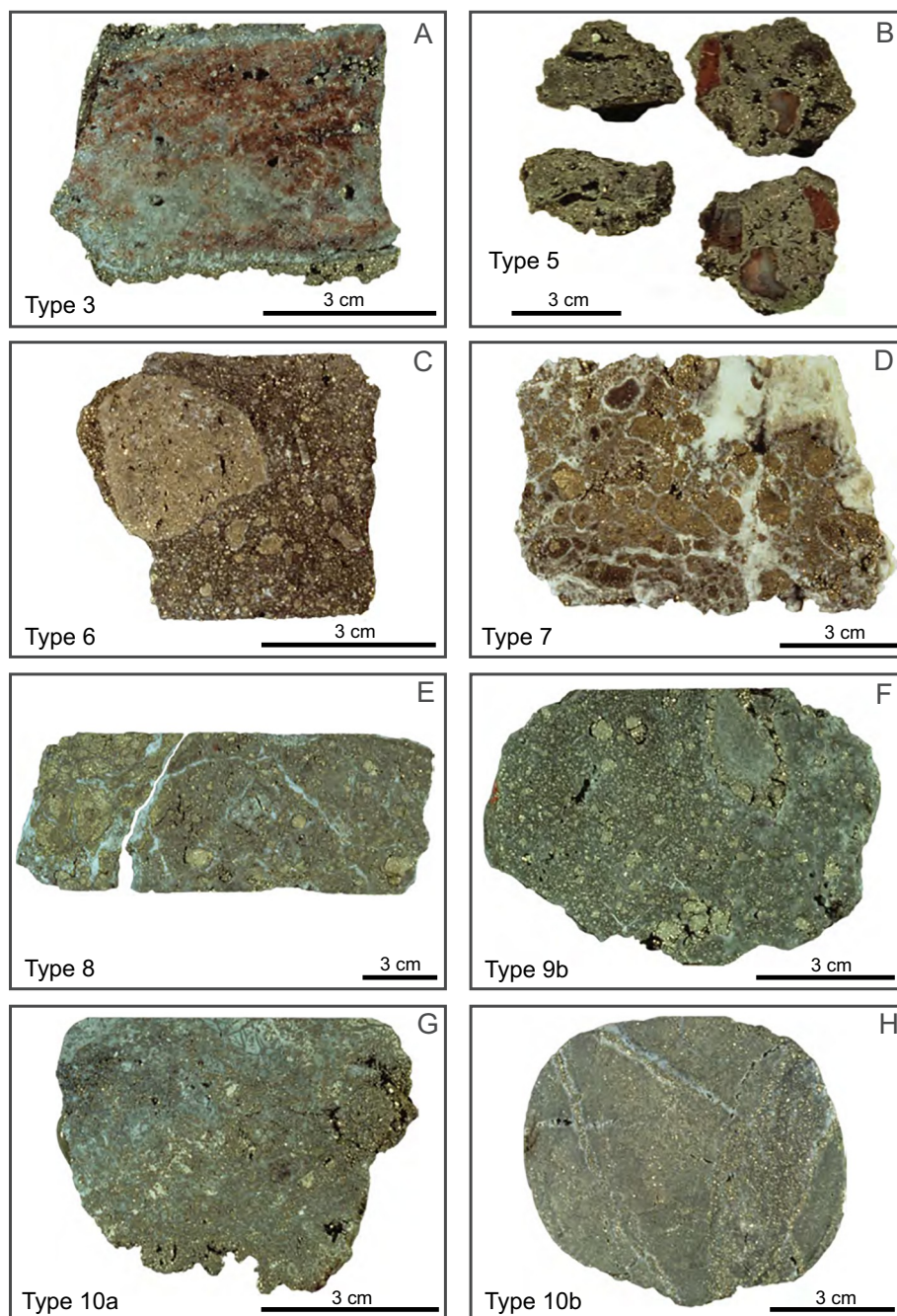


**Fig. 4.** Representative samples of drill core from the TAG mound. A) Gray chert (type 3) consisting of medium-grained gray to white granular and massive quartz with fine-grained disseminated pyrite in quartz and rimming clasts (5% pore space). TAG-4, 34.30 mbsf, zone 0. B) Porous massive pyrite (type 5) containing granular, euhedral, and colloform pyrite, plus jasper clasts with late sphalerite in open spaces (25% pore space). TAG-2, 10.19 mbsf, zone 1. C) Porous, nodular pyrite breccia (type 6) consisting of fine- to coarse-grained subhedral to euhedral pyrite in clasts and matrix, fine- to medium-grained matrix anhydrite, and minor fine-grained chalcopryite. TAG-1, 1.68 mbsf, zone 1. D) Nodular siliceous pyrite-anhydrite breccia (type 7) composed of fine- to medium-grained nodular pyrite, fine- to coarse-grained anhydrite in veins, and minor silica in pyrite-silica and wallrock clasts. Massive pyrite clasts contain very fine-grained disseminated chalcopryite coeval with pyrite. TAG-1, 21.05 mbsf, zone 2. E) Pyrite-silica-anhydrite breccia (type 8) consisting of fine- to medium-grained pyrite and very fine-grained silica in pyrite-silica clasts, fine- to medium-grained chalcopryite, and minor fine- to medium-grained anhydrite in veins, and as crustiform and dissolution textures (porosity = 5%). TAG-1, 32.35 mbsf, zone 2. F) Nodular pyrite-silica breccia (type 9) consisting of fine-grained quartz clasts in dark gray silica matrix, fine- to coarse-grained pyrite as nodular pyrite and rimming quartz fragments, and minor anhydrite. TAG-5, 40.10 mbsf, zone 2. G) Silicified wallrock breccia (type 10a) composed of very fine-grained silica and minor clays replacing basalt, and very fine- to fine-grained disseminated pyrite in 'veins' on the edge of the sample (porosity = 5%). TAG-4, 38.51 mbsf, zone 3. H) Type 10b chloritized basalt breccia with very fine-grained quartz in crosscutting veins replacing basalt, very fine-grained chlorite replacing basalt, very fine- to medium-grained pyrite disseminated in cross-cutting quartz veins, and fine- to coarse-grained euhedral anhydrite in veins on exposed broken surfaces (porosity = 7%). Minor fine-grained chalcopryite occurs in anhydrite veins with pyrite. TAG-1, 116.19 mbsf, zone 4. Sample descriptions and photographs are from Humphries et al. (1996).

silicified wallrock breccia (type 10a) cemented by massive pyrite and cut by quartz and pyrite veins were also sampled. At 42 mbsf, there is an abrupt transition to a variably chloritized basaltic footwall (type 10b). Core from the TAG-4 area differs from the rest of the active mound by the lack of anhydrite, more abundant amorphous silica, marcasite, and sphalerite, and a less-altered footwall.

Two holes were drilled on the upper terrace approximately 20–30 m to the north of the BSC (TAG-5; Fig. 2) to 59.4 mbsf. The core from this area mainly consists of brecciated massive sulfides similar to TAG-1, and the core recovery was low (Humphries et al., 1996). Between surface and 10 mbsf, nodular pyrite- and pyrite-anhydrite breccias (types 6–7) are similar to those of the anhydrite-rich zone at TAG-1. They contain minor chalcopryite in a medium- to fine-grained matrix of pyrite and anhydrite. Between 10 and 45 mbsf, two samples were selected to represent the gradual transition from massive pyrite breccias (types 5–6), and pyrite-anhydrite-breccias (type 7) to pyrite-silica

breccia (type 9) above 30 mbsf and to silicified wallrock breccia below 30 mbsf. Anhydrite is most abundant above 10–15 mbsf as open-space filling (type 7), veins and cement in nodular pyrite-anhydrite breccia in TAG-5, but it also occurs as later veins in pyrite-anhydrite breccia to 25 mbsf.

### 3.2. Subseafloor temperature regime

Petersen et al. (1998, 2000) and Tivey et al. (1998) conducted detailed fluid inclusion studies of quartz and anhydrite to investigate the vertical and horizontal temperature regime in the TAG hydrothermal system (Fig. 5). Due to its retrograde solubility, the trapping temperatures of fluid inclusions in anhydrite record only the most recent high-temperature hydrothermal venting, whereas quartz trapping temperatures record multiple hydrothermal events. Trapping temperatures of fluid inclusions in both minerals are from 187° to 390 °C, with an



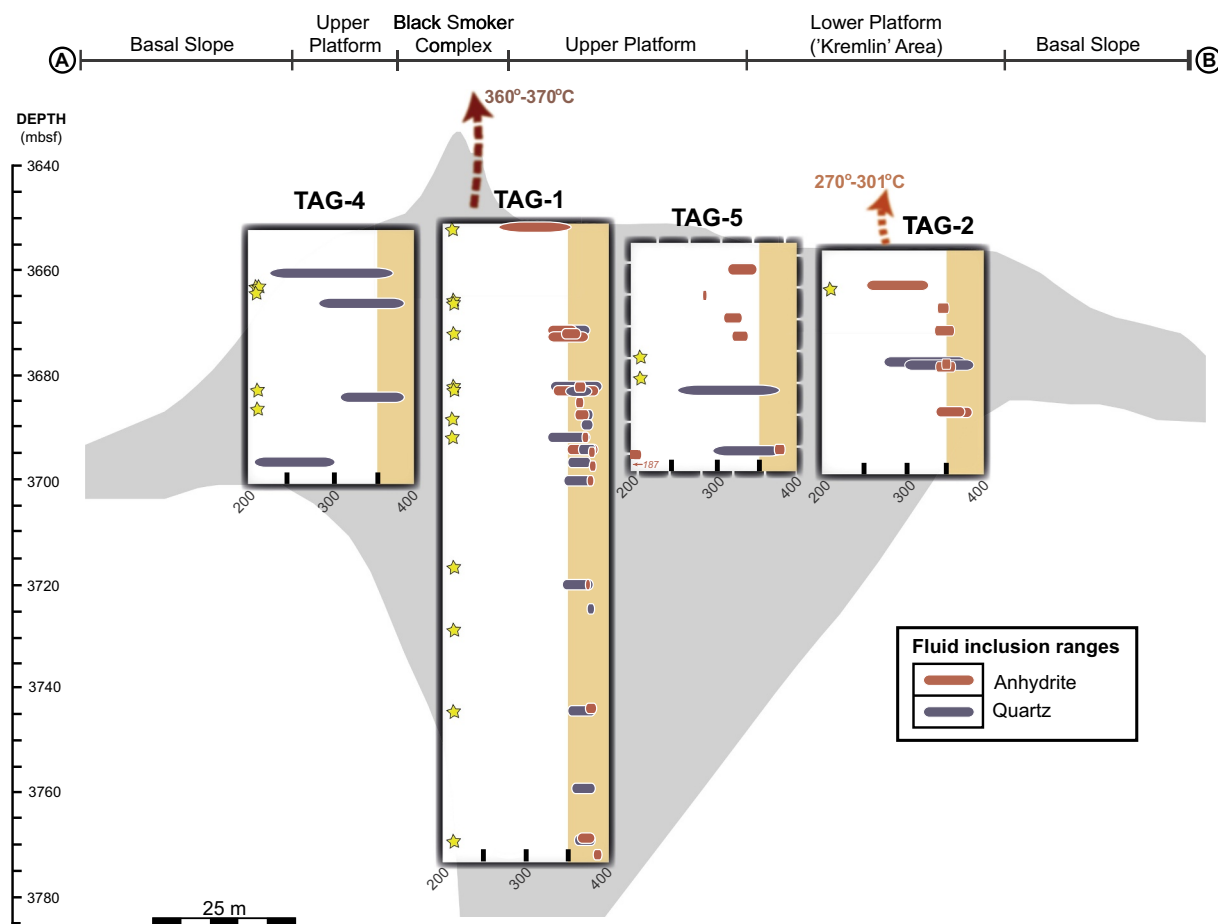


**Fig. 5.** Downhole plots showing ranges of fluid inclusion trapping temperatures compiled from Petersen et al. (1998, 2000) and Tivey et al. (1998). Data are for quartz (blue) and anhydrite (red). Yellow stars show approximate locations of samples in this study. Arrows are exit temperatures of the Black Smoker Complex and the Kremlin area from Edmond et al. (1995) and Parker and von Damm (2005). The Kremlin area is now inactive, so temperatures correspond to those at the time of mineralization. The shaded field in each plot corresponds to temperatures  $> 350^{\circ}\text{C}$ . (For interpretation of the references to colour in this figure legend, the reader is referred to the web version of this article.)

overall temperature increase with depth. In the central anhydrite-rich zone 2, fluid inclusions in anhydrite and quartz have similar ranges of trapping temperatures ( $340^{\circ}\text{--}384^{\circ}\text{C}$  and  $337^{\circ}\text{--}381^{\circ}\text{C}$ , respectively), which correspond to the recorded exit temperatures of the Black Smoker Complex ( $360\text{--}370^{\circ}\text{C}$ ; Edmond et al., 1995; Edmonds et al., 1996). Anhydrite and quartz in the stockwork (zones 3 and 4; Fig. 3) were precipitated at temperatures higher than  $375^{\circ}\text{C}$ , indicating that the hydrothermal fluids cooled conductively or mixed with ambient seawater prior to venting (Petersen et al., 2000; Tivey et al., 1998). Lower trapping temperatures close to the current and paleo-seafloor indicate local entrainment of seawater into the mound. The lack of anhydrite cement in TAG-4 drill core, the long tail of lower fluid inclusion trapping temperatures in quartz (Fig. 5), and only slightly to moderately altered basaltic basement at depth indicate that this part of the mound is outside the current high-temperature upflow (Petersen et al., 2000), although primary fluid inclusions in quartz and oxygen isotope data indicate that temperatures reached  $390^{\circ}\text{C}$  at some point in the past (Alt and Teagle, 1998; Petersen et al., 2000). Fluid inclusion trapping temperatures in quartz and anhydrite from TAG-2 are between  $266^{\circ}$  and  $375^{\circ}\text{C}$ , overlapping exit temperatures of  $270\text{--}301^{\circ}\text{C}$  previously measured in the Kremlin Area (Edmond et al., 1995). Samples from TAG-5 have trapping temperatures between  $187^{\circ}$  and  $383^{\circ}\text{C}$  (Tivey et al., 1998; Petersen et al., 2000), however, a strong down-hole temperature increase indicates additional high-temperature upflow at the northern margin of the mound outside the Black Smoker Complex (Fig. 5). Using these data, samples of the drill core chosen for LA-ICP-

MS have been assigned to three broad temperature regimes, namely the BSC, the hydrothermal mound, and the stockwork (Fig. 3).

### 3.3. Bulk geochemistry

The trace element geochemistry of the deposit has been previously documented in 168 bulk samples of sub-surface sulfide-bearing drill core (Fouquet et al., 1998; Hannington et al., 1998b; Miller, 1998: Table 2). High average Fe and S concentrations (32.6 wt% and 41.7 wt%, respectively) reflect the abundance of pyrite in all samples. Average Cu (2.7 wt%) and Zn (0.6 wt%) concentrations are lower than reported for many other mid-ocean ridge sulfide deposits, but this reflects a strong bias in sampling of active chimneys in other studies. As observed in other drilled deposits, Cu and Zn grades are almost always lower in the interiors of the mounds than in the surface chimneys (e.g., Petersen et al., 2016). The highest Cu concentrations in the drill core from TAG (2.7–3.4 wt%) are found in the massive pyrite and anhydrite breccias (types 5, 6 and 7) in the TAG-1, 2, and 5 areas. The highest Zn (1.3 wt%) occurs in massive pyrite and pyrite breccias (types 5 and 6) in the TAG-4 area. Fouquet et al. (1998) and Herzig et al. (1998) identified a group of trace elements associated with Cu that were interpreted to be of high-temperature origin (i.e., Co and Se), and other elements associated with Zn in the outermost zones of the deposit that reflect lower temperatures (i.e., Ag, As, Sb, In, Tl, Ga, Pb, Cd, Au; Table A1.1), consistent with bulk geochemical studies of many other modern and ancient seafloor sulfide deposits (e.g., Franklin et al., 2005; Hannington et al., 2005; Monecke et al., 2016).

**Table 2**  
Bulk geochemistry of the TAG mound.

	Method	n	> DL	Deposit mean	TAG-1 mean	TAG-2 mean	TAG-3 mean	TAG-4 mean	TAG-5 mean	Cherts and iron oxides Zone 0 Types 1–4	Massive Sulfides Zone 1 Types 5–6	Anhydrite zone Zone 2 Types 7–8	Pyrite- silica breccias Zone 3 Types 9	Silicified wallrock Zones 3/4 Type 10	Anhydrite veins Type 11
wt%															
Fe	1,2	167		31.8	32.0	31.2	11.1	31.5	36.9	26.3	37.6	32.7	30.3	28.6	24.5
S	2,3	152		42.1	42.9	40.8	28.9	37.6	47.6	24.1	47.1	45.6	37.6	39.5	40.2
Cu	1,2	153		2.73	3.04	2.09	3.81	1.32	3.67	6.32	3.08	2.72	1.86	1.58	3.85
Zn	1,2	112		0.47	0.04	0.53	0.39	1.26	0.11	0.26	1.02	0.05	0.33	0.01	0.02
SiO <sub>2</sub>	1,2	137		17.5	14.0	20.0	53.4	21.8	6.90	42.7	6.57	5.26	26.7	23.2	21.3
Ca	1,2	131		2.75	3.83	1.39	0.13	0.46	3.18	0.16	2.04	5.51	1.69	1.85	4.51
MnO	1,2	57		0.01	0.01	0.02	0.03	0.02	0.01	0.04	0.01	0.01	0.01	0.02	0.03
TiO <sub>2</sub>	1	41		0.09	0.04	0.37	0.03	0.09	0.04	0.03	0.08	0.03	0.06	0.29	0.65
Al <sub>2</sub> O <sub>3</sub>	1,2	56		1.12	0.44	2.66	0.12	0.67	2.23	0.31	2.07	0.34	0.51	2.19	4.47
MgO	1,2	63		0.51	0.14	2.99	0.13	0.26	0.08	0.24	0.11	0.10	0.12	3.42	11.7
Na <sub>2</sub> O	1	89		0.14	0.09	0.22	0.28	0.17	0.13	0.35	0.08	0.09	0.08	0.14	0.21
K <sub>2</sub> O	1	35		0.06	0.03	0.08	0.05	0.11	0.04	0.10	0.05	0.04	0.03	0.05	0.03
P <sub>2</sub> O <sub>5</sub>	1	52		0.06	0.01	0.10	0.06	0.18	0.01	0.34	0.02	0.01	0.02	0.01	0.02
ppm															
Au	4	87		0.45	0.15	1.04	1.11	0.49	0.29	0.11	471.2	0.17	0.25	0.05	0.05
Ag	1,2	77		11.1	1.59	43.4	9.13	16.7	3.97	19.30	16.2	1.29	4.39	0.73	0.50
As	2,4	135		39.9	33.7	32.0	20.6	61.2	41.6	38.6	51.8	39.4	28.0	21.0	20.1
Ba	1	59		107.3	84.3	60.0	90.0	176.7	112.3	206.7	102.0	86.4	91.7	78.8	80.0
Bi	1	24		21.9	27.2	11.5	36.0	6.17	18.3	8.00	11.8	18.2	35.3	20.5	47.0
Cd	1,2	77		20.0	2.07	48.4	18.3	33.6	5.21	13.60	39.1	1.32	8.67	2.50	5.00
Co	2,4	126		285.3	288.1	243.8	55.0	184.9	437.2	69.1	332.3	225.7	288.3	398.3	461.8
Ga	4,5	65		6.91	1.70	14.4	12.0	14.1	5.14	10.50	12.2	2.43	3.02	2.94	9.20
Ge	2,4	10		13.7	6.00	28.5	< 5.00	10.6	< 5.00	< 5	13.7	< 5.00	< 5.00	< 5.00	< 5.00
In	1,2	61		1.33	0.33	4.13	2.12	0.95	1.77	1.33	1.27	0.77	0.50	0.23	0.40
Mo	2,4	153		77.4	73.1	56.4	32.3	97.8	96.7	35.0	101.8	75.6	67.8	61.7	52.8
Ni	1	28		14.1	5.91	36.8	15.3	12.8	7.00	15.8	9.88	6.80	6.25	55.7	75.5
Pb	1,2	158		53.5	30.3	56.3	69.9	103.5	43.6	59.2	85.6	30.7	37.3	22.3	26.4
Sb	4,5	73		3.83	3.13	3.70	11.3	3.65	1.73	4.33	3.58	1.73	2.96	1.22	7.25
Se	2,4	97		28.7	34.3	19.4	12.0	8.56	33.6	8.50	49.9	16.2	16.1	26.8	22.0
Sn	2,4	25		5.32	4.45	12.0	5.33	1.67	1.00	4.00	2.00	2.00	5.25	3.50	11.0
Tl	4,5	65		3.33	1.75	1.78	1.22	7.63	2.92	1.47	7.17	2.24	2.56	0.90	0.53
U	4,5	65		7.94	6.72	7.12	6.03	10.5	8.36	7.84	11.2	8.14	7.53	4.61	6.05
V	1	67		25.4	8.67	59.6	21.6	46.2	16.2	74.4	14.9	8.50	10.6	40.4	113.5
W	4	0		< 4.00	< 4.00	< 4.00	< 4.00	< 4.00	< 4.00	< 4.00	< 4.00	< 4.00	< 4.00	< 4.00	< 4.00

Average values from ODP Leg 158 (Fouquet et al., 1998; Hannington et al., 1998b; Miller, 1998) by TAG areas (see text) and mineralized zones from Table 1. Analytical methods: 1) ICP-ES, 2) XRF, 3) Leco, 4) INAA, 5) ICP-MS.

#### 4. Methodology

Detailed petrography was carried out on all samples to establish the paragenesis of the sulfides and identify the different stages of pyrite growth in relation to previously published fluid inclusion data. Ten pyrite samples were etched with 70% nitric acid (HNO<sub>3</sub>) to highlight growth textures and guide transects for LA-ICP-MS across multiple pyrite generations. Samples were coated with a thin film of HNO<sub>3</sub> for 30 s, rinsed with distilled water to remove residue, and then dried. The process was repeated as required. Details of the petrographic study are provided in Table 3 and discussed below.

Prior to LA-ICP-MS analysis, pyrite grains (and other minerals) were analyzed by EPMA ( $n = 454$ ) to confirm the bulk composition and to provide data for standardization of the laser ablation results (Table B1). Iron, Cu, Zn, and S were determined on a JEOL-8200 Superprobe at the GEOMAR Helmholtz Center for Ocean Research Kiel, Germany. Operating conditions were 15 kV accelerating voltage and 50 nA current with a 50 s count time. A natural chalcopyrite standard was used for Fe, Cu, and S, and a synthetic sphalerite standard for Zn.

LA-ICP-MS analyses were performed using a 193 nm Excimer laser ablation system (Coherent, GeoLasPro) coupled to a double-focusing, high-resolution magnetic sector mass spectrometer (Nu Instruments, AttoM) in low-resolution mode (300 Res, 10% valley definition) at GEOMAR. The instrument tuning was optimized to provide a maximum ion transmission and low polyatomic cluster production (ThO/

Th  $\leq 0.02\%$ ; CuAr/Cu  $< 0.0025\%$ ) employing a very hot plasma (normalized argon index NAI  $\approx 30$ ) according to the method of Fietzke and Frische (2016). Sample ablation was performed under He carrier gas with Ar transport gas added after the ablation cell. A short pre-ablation to remove surface contaminants preceded each analysis. Spot analyses ( $n = 357$ ) were performed with 30 s ablation at a laser repetition rate of 5 Hz, a beam diameter between 16 and 44  $\mu\text{m}$ , and a fluence of  $2 \text{ J cm}^{-2}$ . A 50-s gas background was collected prior to each ablation. All analyzed spots were free of exsolution textures and visible micro-inclusions at the surface (limit of visual detection  $\sim 1 \mu\text{m}$ ). Each analysis consisted of three adjacent spot placements using a shallow sampling depth of approximately 10–12  $\mu\text{m}$ , and the raw data for all three spots were integrated together. An advantage of this approach is the lower probability that unseen inclusions below the sample surface are inadvertently analyzed. Where evidence of submicroscopic inclusions was observed during ablation, this was noted but the depth profiles retained in order to estimate the contribution of inclusions to the trace element budget. Post-analysis inspection of all sample sites visually confirmed well-formed ablation pits and accurate placement of the laser.

The following isotopes were determined by the analytical routine: <sup>51</sup>V, <sup>55</sup>Mn, <sup>57</sup>Fe, <sup>59</sup>Co, <sup>60</sup>Ni, <sup>63</sup>Cu, <sup>66</sup>Zn, <sup>71</sup>Ga, <sup>73</sup>Ge, <sup>75</sup>As, <sup>77</sup>Se, <sup>95</sup>Mo, <sup>107</sup>Ag, <sup>111</sup>Cd, <sup>115</sup>In, <sup>118</sup>Sn, <sup>121</sup>Sb, <sup>128</sup>Te, <sup>182</sup>W, <sup>197</sup>Au, <sup>205</sup>Tl, <sup>208</sup>Pb, <sup>209</sup>Bi, and <sup>238</sup>U (full results are presented in Table C1). The isotopes <sup>24</sup>Mg, <sup>27</sup>Al, and <sup>29</sup>Si were also monitored to check for potential contamination



**Table 3**  
Summary of petrographic data for samples in this study.

Section name	TAG area	Depth (mbsf)	Sub-type	Mineralization type	Pyrite type occurrence						Mineralogy														
					I	II	III	IV	V	VI	Py	Mc	Cpy	Sph	Po	Dg	Cv	Bn	Anh	Qtz	Clc	AmSi	Chl	Fe-Ox	Clay
957F-1N-1-10D	1	1.68	6a	Massive pyrite breccia	x			x	x	x	*****	**	**				*****	tr	tr					tr	
957A-3X-1-4	2	10.19	2	Red and gray chert	x			x	x	x	*****	*	tr	*			*****	tr		tr?				*	
957K-3X-1-3	4	14.61	5	Massive pyrite	x	x		x	x	x	*****	*****	tr	tr			*****	tr	tr	tr		tr	tr	tr	
957M-3R-1-11	4	14.71	5a	Porous massive pyrite				x	x	x	*****	*****	*	*			*****	*	tr	tr			tr	tr	
957C-5N-1-6	1	15.39	7a	Massive pyrite-anhydrite breccia	x		x	x	x	x	*****	**	tr	tr			*****	*	tr	tr?			tr	tr	
957M-3R-1-30	4	15.60	9a	Pyrite-silica breccia	x			x	x	x	*****	*	tr	tr			*****	tr		tr?			tr	tr	
957G-3N-1-6	1	21.05	7c	Massive pyrite-anhydrite breccia	x			x	x	x	*****	tr	*	tr			*****	tr	tr	tr			tr	tr	
957C-7N-2-1D	1	21.32	7c	Massive pyrite-anhydrite breccia	x		x	x	x	x	*****	*	*				*****	*****		*****			tr	tr	
957C-11N-2-1B	1	32.19	8	Pyrite-silica-anhydrite breccia	x			x	x	x	*****	tr	*				*****	*	*	*****			tr	tr	
957C-11N-2-1E	1	32.35	8	Pyrite-silica-anhydrite breccia	x		x	x	x	x	*****	*	*				*****	*	*	*****			tr	tr	
957M-7R-1-1	4	34.30	3	Gray silica	x			x	x	x	**	*	*		tr	tr	*	tr	tr?	*			*	*	
957P-8R-1-7	5	35.37	5a	Porous massive pyrite	x			x	x	x	*****	tr	*	*	tr		*****	*	*	*			tr	tr	
957C-13N-1-4	1	37.31	9a	Pyrite-silica breccia	x			x	x	x	*****	*	tr	*			*****	*	*	*			tr	tr	
957M-8R-1-5	4	38.51	10a	Silicified wallrock breccia	x			x	x	x	*****	*	tr	tr			*****	*	*	*			tr	tr	
957P-9R-1-1	5	40.10	9b	Nodular pyrite-silica breccia	x		x	x	x	x	*****	*	tr	tr			*****	*	*	*			tr	tr	
957C-15N-2-1D	1	43.34	10a	Silicified wallrock breccia	x		x	x	x	x	*****	*	tr	tr			*****	*	*	tr?			tr	*	
957E-6R-1-7	1	63.58	5c	Massive granular pyrite	x			x	x	x	*****	*	*	*			*****	*	*	*			tr	tr	
957E-9R-1-3	1	78.00	5c	Massive granular pyrite	x			x	x	x	*****	tr	*	tr			*****	*	*	*			*	tr	
957E-12R-1-4	1	92.00	10a	Silicified wallrock breccia	x		x	x	x	x	*****	*	*	*			*****	*	*	*****			*****	tr	
957E-17R-1-3	1	116.19	10b	Chloritized basalt breccia	x		x	x	x	x	*****	tr	*	tr			*****	*	*	tr			*****	*****	

Summary of petrographic data plus presence and absence of pyrite types in petrological sections from the TAG mound. Abundances: \*\*\*\* = dominant (> 50%), \*\*\* = major (26–50%), \*\* = abundant (11–25%), \* = minor (6–10%), \* = rare (1–5%), tr = trace. Abbreviations: Py = pyrite, Mc = marcasite, Cpy = chalcopyrite, Sph = sphalerite, Po = pyrrhotite, Dg = digenite, Bn = bornite, Anh = anhydrite, Qtz = quartz, Clc = chalcocite, asl = amorphous silica, Chl = chlorite, FeOx = Fe-oxide, Clay = undefined clays, bx = breccia, sil = silica. Mineralization types are detailed in Table 1 and pyrite types are described in Section 5.1.1.

and inclusions from surrounding silicate gangue minerals.  $^{44}\text{Ca}$  was monitored closely to confirm that no anhydrite inclusions were sampled. A NIST-SRM 610 glass standard, which has certified values for all elements of interest, was used for calibration (Wise and Watters, 2012). Fietzke and Frische (2016) have shown that fractionation effects commonly associated with different matrices are minimal for low entry of ablated material into very hot plasma used in this routine. For quality assurance, two synthetic sulfide reference materials (PGE\_Ni7b and trans\_1: Wohlge-muth-Ueberwasser et al., 2007, 2014) were also included as unknowns in each analytical run and the elements As, Fe, Sb, Ni, Te, and Se monitored. MPI-DING glasses (ATHO-G, T1-G, GOR132-G, KL2-G: Jochum et al., 2006) were also analyzed to monitor quality. Data reduction and quantification of element concentrations was carried out using the linear slope regression method of Fietzke et al. (2008). Known Fe concentrations from EMPA were used as an internal standard. Major element analyses from EMPA show the sulfides in this study were of stoichiometric composition. Detection limits were calculated in MatLab based on the measured background for each individual analysis.

## 5. Results

### 5.1. Mineral paragenesis

#### 5.1.1. Pyrite

Pyrite is present throughout the deposit and formed over a wide range of temperatures and compositions, and at different stages of mound growth. Six paragenetic types are recognized with distinct textures: sub-rounded cores (Py I), colloform (Py II), porous (Py III), granular (Py IV), euhedral (Py V), and late overgrowths (Py VI). Etching shows complex zoning from core to rim.

Sub-rounded Py I cores revealed by etching (Fig. 6a) are the remnants of early pyrite overprinted by multiple later stages of pyrite growth. This texture is common in massive and semi-massive pyrite breccias, in pyrite-rich quartz and anhydrite breccias in the interior of the mound, and in altered basalt in the stockwork zone. Fine-grained colloform Py II (Fig. 6b) is most abundant in the lower-temperature outer portion of the mound (TAG-4 area), especially in massive sulfide crusts together with colloform marcasite and fine-grained sphalerite (Fig. 6c). Colloform pyrite and marcasite are also common in cherty silica at the top of the deposit in the TAG-4 area, and in sulfide-rich chimney talus in the upper 5 m of the drill core from the TAG-1 and TAG-4 areas (cf. Humphries et al., 1996). Porous Py III (Fig. 6d) occurs mainly in nodular aggregates of massive and semi-massive pyrite in the top 15 m of the mound (TAG-1). It is characterized by abundant pore spaces, mainly filled by silica and minor Fe-oxides, which may reflect late-stage leaching or seafloor weathering. However, porous Py III is similar to the sub-rounded Py I cores, and therefore may be part of the early high-temperature pyrite paragenesis in some samples (e.g., in the TAG-1 and TAG-5 areas). Granular Py IV (Fig. 6e) is most common in subhedral aggregates within quartz and anhydrite gangue and as vein selvages in the interior of the mound below TAG-1; it is also abundant in silicified pyrite breccias from the TAG-2 and TAG-4 areas. Pyrite IV appears to be paragenetically equivalent to, or replaces porous Py III. Euhedral Py V has sharp, well-defined crystal boundaries and discrete well-formed euhedral shapes, commonly overgrowing Py III and Py IV in open spaces or at the margins of quartz veins (Fig. 6f). It occurs throughout the mound and in the lower stockwork and altered basalt to a depth of at least ~78 mbsf. Late Py VI (e.g. Fig. 6f) is mainly an overgrowth on euhedral Py V. It is found in massive pyrite breccia near the surface in the TAG-1 area, near the bottom of the mound in the TAG-1 and TAG-5 areas, and in silicified pyrite breccia in the TAG-4 area. The close association with amorphous silica suggests that Py VI was mainly deposited during a late cooling stage. Commonly, euhedral Py V and later Py VI are separated by a fine-grained Fe-oxide and/or silica band.

Porous Py III and granular Py IV are the most abundant types volumetrically throughout the deposit. The clearest temporal distinction is between the early Py I sub-rounded cores and later colloform Py II and Py VI overgrowths. Porous and colloform Py II and III commonly show partial dissolution and are replaced throughout by granular Py IV and euhedral pyrite Py V. The positions of the samples in the mound are taken as an indication of the most likely temperature regime at the time of mineralization, and the textural relationships interpreted to reflect higher- and lower temperatures of mineralization (e.g., rounded cores, replacements, overgrowths) are consistent with those observed in active vents at the surface of the mound where the temperatures are well known (e.g., Rona et al., 1993a, 1993b; Tivey et al., 1995).

#### 5.1.2. Marcasite

Marcasite is commonly intergrown with fine-grained colloform Py II as fine to coarse crustiform bands, especially in the TAG-4 area (Fig. 6b), and also as coarse bladed crystals growing into veins and open spaces in the TAG-1 area (Fig. 6g). Pyrite pseudomorphs of the original coarse bladed marcasite are also observed (Fig. 6g). Knott et al. (1998) previously noted that some coarse tabular pyrite crystals contain small oriented and unoriented cores with a strained and cracked appearance typical of the volume change that occurs during replacement of marcasite by pyrite (Murowchick, 1992). Thus, the majority of the marcasite is thought to be a remnant of earlier, relatively low-temperature mineralization overgrown and replaced by early fine-grained pyrite in the lower-temperature parts of the mound.

#### 5.1.3. Sphalerite

In all samples from the upper part of the mound, sphalerite is intergrown with colloform Py II and marcasite and also occurs as oriented inclusions and rims on recrystallized euhedral Py V (e.g. Fig. 6h and i). The lack of sphalerite in Py I, and its occurrence only as inclusions in Py III, IV, and VI, is consistent with a lower-temperature paragenesis in the outer part of the mound and (with Py V) in the latest stages of mineralization in the TAG-4 area.

#### 5.1.4. Chalcopyrite

Chalcopyrite occurs mainly as a replacement of sphalerite and pyrite (Fig. 6j) in the higher-temperature core of the mound (TAG-1 and TAG-5 areas) and also as inclusions within later pyrite euhedra (Py V).

#### 5.1.5. Other sulfides

Trace pyrrhotite and secondary Cu-sulfides are present. Galena was documented in a few core samples by Petersen et al. (2000) but was not found in any of the samples chosen for this study.

### 5.2. LA-ICP-MS data

#### 5.2.1. Pyrite

We analyzed 260 pyrite grains. The ranges of trace element concentrations fall into 4 main groups: 100–1000 ppm, 10–100 ppm, 1–10 ppm, and 0.1–1 ppm (Table 4). Elements with the highest concentration are Co (avg. 448 ppm, up to 6770 ppm) and Cu (avg. 132 ppm, up to 1900 ppm), which were above their respective detection limits in almost every analysis. Average concentrations of Zn, Pb, As, Mn, Mo, Ni, and Se are between 10 and 100 ppm, with notable outliers (up to 1893 ppm Zn, 1923 ppm Mn, and 1190 ppm As). Average concentrations of Ag, Tl, Sb, Cd, Ge, Te, and V are between 1 and 10 ppm (up to 102 ppm Ag, 152 ppm Tl, and 214 ppm Sb). Average concentrations of Bi, Au, Ga, In, Sn, V, W, and U are all < 1 ppm.

Depth profiles for Co, Se, (Fig. 7a) and Ni (Fig. 7b) in pyrite are smooth and indicate that these elements are present mainly in lattice substitutions rather than as inclusions of other sulfides (e.g. Fig. 8a). In contrast, profiles for Zn are irregular and likely reflect abundant sphalerite micro-inclusions in pyrite (Fig. 7c). The ablation profiles for Mo are both irregular and smooth; at concentrations above ~200 ppm,



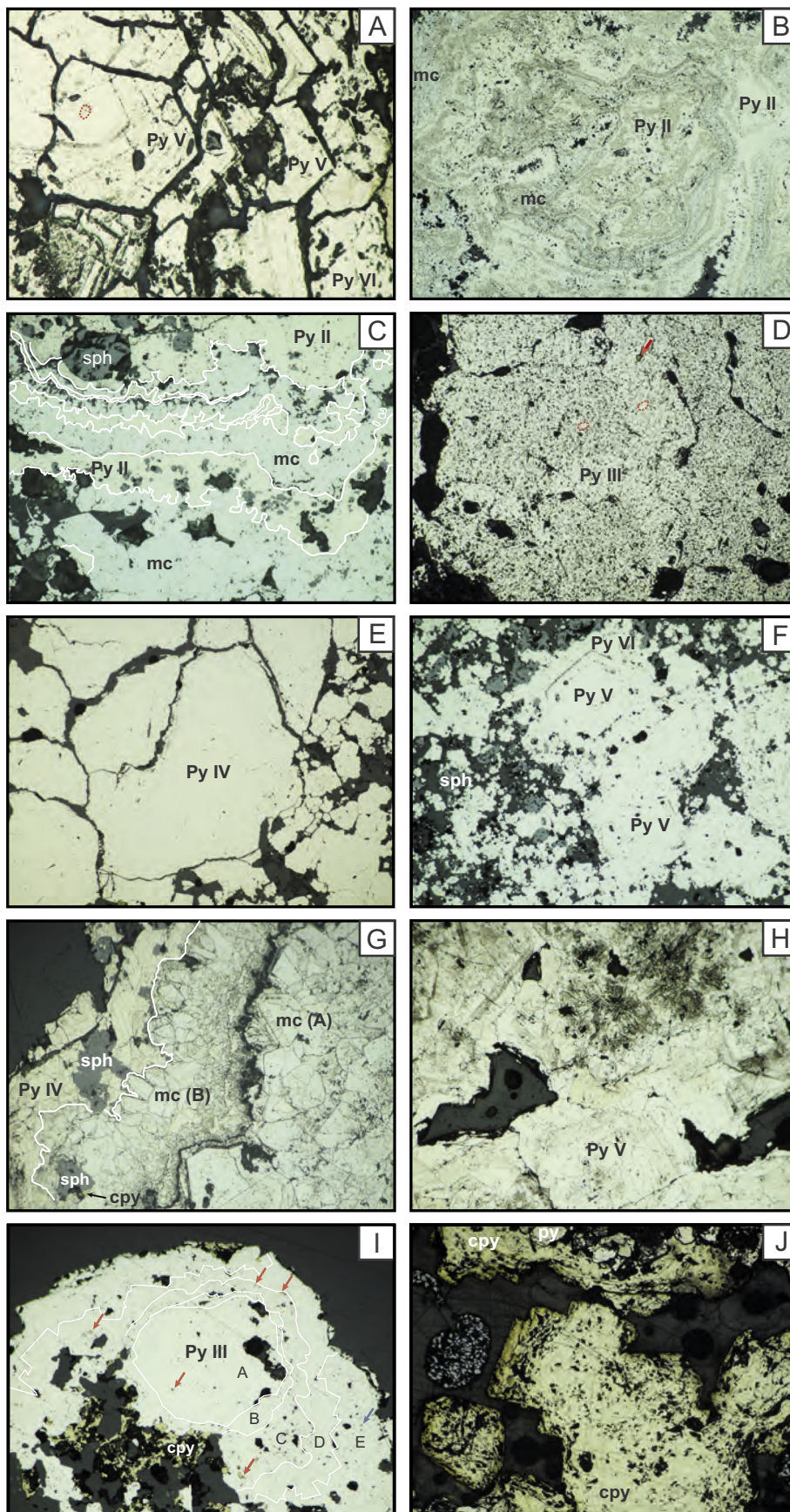


**Fig. 6.** Representative reflected light photomicrographs of sulfide textures from this study. A) Remnant Py I core after etching (outlined in red) surrounded by multiple later generations of euhedral Py V and Py VI from TAG-1. Sample 957F-1N-1-10D, Hole F, 1.68 mbsf, type 6. FOV = 0.7 mm. B) Intimately intergrown bands of colloform Py II (pale yellow) and marcasite (blue-yellow) indicated by a change in porosity between more porous marcasite and less porous Py II (TAG-4). Sample 957K-3X-1-3, 14.61 mbsf, Hole K, type 5. FOV = 0.3 mm. C) Coarse intergrown and partially recrystallized Py II (pale yellow) and marcasite (blue-yellow) from TAG-4. Pyrite contains more sphalerite inclusions than marcasite. Sample 957K-3X-1-3, 14.61 mbsf, Hole K, type 5. FOV = 0.7 mm. D) Porous and altered Py III from TAG-1. Remnant Py I cores after etching are outlined in red. A small chalcopyrite inclusion is indicated by the red arrow. Sample 957C-7N-1-1D, 21.32 mbsf, type 7. FOV = 0.7 mm. E) Brecciated clast of recrystallized granular Py IV (yellow) with remnant 120° grain boundaries (TAG-4). Sample 957M-3R-1-30, 15.6 mbsf, Hole M, type 9. FOV = 0.7 mm. F) Multiple generations of euhedral Py V (pale yellow) indicated by sphalerite inclusions (pale gray) in a matrix of quartz (dark gray) and surrounded by late Py VI overgrowths from TAG-4. Sample 957K-3X-1-3, 14.61 mbsf, Hole K, type 5. FOV = 0.7 mm. G) Multiple stages of marcasite (blue-yellow) (TAG-4). Marcasite A coarsens from right to left; the boundary between marcasite A and B is marked by finer-grained marcasite, sphalerite (dark gray), and Py I (pale-yellow). Marcasite B coarsens from right to left; well-developed blades show growth into a vein or open space. Appearance of sphalerite outlining coarse marcasite blades indicates the transition of marcasite B to pyrite. Marcasite B is finer-grained near the contact where it is replaced by Py IV. Remnant chalcopyrite (yellow) is also present. Sample 957M-3R-1-11, 14.71 mbsf, Hole M, type 5. FOV = 0.7 mm. H) Recrystallized massive pyrite (Py V) with remnant spheroidal textures (TAG-1). Cracks and strain are interpreted to reflect inversion of marcasite to pyrite (e.g., Murowchick, 1992). Sample 957G-3N-1-6, 21.05 mbsf, Hole C, type 7. FOV = 0.7 mm. I) Multiple generations of subhedral pyrite and colloform Py II (pale yellow) from TAG-4. Recrystallized, earlier subhedral porous Py III (A,B) containing chalcopyrite inclusions (red arrows) is overgrown by partially recrystallized, later colloform Py II (C). Euhedral pyrite with defined crystal faces (D) overgrows (C), and later partially recrystallized colloform pyrite (E) has overgrown (D). A rare sphalerite inclusion is indicated by the blue arrow. Sample 957M-7R-1-1, 34.30 mbsf, Hole M, type 3. FOV = 0.7 mm. J) Massive, coarse chalcopyrite (yellow) likely pseudomorphing pyrite (TAG-1). The light gray fragments are an artifact from sample preparation. Sample 957E-9R-1-3, 78 mbsf, Hole E, type 9. FOV = 0.7 mm. Abbreviations: cpy = chalcopyrite, py = pyrite, mc = marcasite, sph = sphalerite. Mineralization types are detailed in Table 1. (For interpretation of the references to colour in this figure legend, the reader is referred to the web version of this article.)



**Table 4**  
Summary of LA-ICP-MS data (in ppm) for samples in this study.

All data in ppm	Fe	Zn	Cd	Ga	In	Te	Au	W	As	Mn	V	U	Ge	Ag	Pb	Sb	Mo	Tl	Ni	Co	Se	Bi	Cu	Sn
<i>Pyrite</i>																								
Maximum	na	1893	21.3	7.18	3.05	9.84	4.50	1.00	1190	1923	8.08	9.05	20.3	102.1	580	214.4	301.3	152.2	212.8	6775	179.9	6.29	1900	4.79
Minimum	na	0.48	0.19	0.05	0.01	0.35	0.01	0.02	1.09	0.12	0.03	0.001	0.94	0.05	0.02	0.05	0.21	0.01	1.09	0.09	1.98	0.01	0.81	0.03
N	na	183	79	82	70	76	85	63	239	223	163	164	80	155	229	163	220	171	101	241	144	158	252	72
Deposit mean	na	51.0	1.29	0.56	0.16	1.93	0.42	0.10	46.0	13.1	1.01	0.31	4.43	3.42	36.9	2.73	30.4	5.22	22.0	447.7	29.1	0.45	132.0	0.37
Deposit median	na	4.0	0.59	0.23	0.06	1.56	0.26	0.05	19.4	0.76	0.36	0.07	2.88	0.75	6.5	0.41	7.9	0.67	7.3	174.0	20.8	0.14	52.2	0.21
TAG-1 mean	na	64.4	1.14	0.59	0.17	2.21	0.54	0.07	46.3	17.5	0.96	0.40	4.5	1.47	17.5	0.78	26.0	2.88	21.3	419.0	30.5	0.47	146.5	0.23
TAG-2 mean	na	53.8	1.10	–	0.20	–	1.15	0.10	50.6	36.8	4.13	0.10	13.5	36.7	119.6	2.45	120.1	14.0	–	1.10	–	0.10	215.9	0.75
TAG-4 mean	na	43.3	1.76	0.62	0.12	1.55	0.34	0.10	45.3	8.0	1.10	0.24	4.1	6.25	80.5	6.60	38.7	10.6	25.2	331.9	21.8	0.48	136.5	0.63
TAG-5 mean	na	7.4	0.57	0.32	0.05	1.28	0.18	0.19	45.5	0.62	0.54	0.06	3.34	0.52	22.5	2.01	14.9	1.44	14.5	837.5	31.9	0.28	43.1	0.14
<i>Marcasite</i>																								
Maximum	na	1338	8.53	1.50	0.28	3.53	0.61	0.31	245.6	13.2	5.38	0.65	9.77	175.5	1006	15.2	221.6	18.2	78.3	671.9	81.9	0.56	379.3	0.89
Minimum	na	1.41	0.34	0.24	0.02	0.46	0.01	0.04	1.02	0.34	0.14	0.002	3.17	0.01	0.21	0.06	0.65	0.03	4.15	0.23	2.99	0.02	1.48	0.06
N	na	21	12	9	8	4	7	8	26	26	25	22	3	19	25	21	26	22	7	22	9	8	26	5
Deposit mean	na	201.3	1.79	0.62	0.09	2.17	0.34	0.16	30.2	4.35	2.11	0.11	5.38	10.6	67.7	1.96	71.1	7.9	16.9	87.8	18.3	0.24	60.5	0.40
Deposit median	na	19.1	1.08	0.38	0.09	2.35	0.44	0.13	12.3	2.53	1.82	0.06	3.21	1.29	10.8	1.15	67.2	6.76	5.07	5.17	8.24	0.10	20.3	0.36
TAG-1 mean	na	10.0	0.65	0.32	0.09	2.35	0.53	0.06	12.4	0.85	0.34	0.29	3.21	0.82	6.80	0.70	66.8	0.52	29.2	232.6	26.9	0.39	119.3	–
TAG-2 mean	–	–	–	–	–	–	–	–	–	–	–	–	–	–	–	–	–	–	–	–	–	–	–	–
TAG-4 mean	na	221.4	2.02	0.70	0.09	1.99	0.27	0.17	35.6	5.40	2.56	0.07	6.47	11.7	79.3	2.09	72.1	8.64	7.64	20.2	7.57	0.15	38.8	0.40
TAG-5 mean	–	–	–	–	–	–	–	–	–	–	–	–	–	–	–	–	–	–	–	–	–	–	–	–
<i>Chalcopyrite</i>																								
Maximum	na	1967	14.4	183.5	52.8	12.3	2.55	0.47	13.2	4.91	11.5	5.20	75.1	56.9	56.1	2.58	18.1	0.39	40.4	251.1	852.5	2.31	na	232.3
Minimum	na	8.61	0.60	1.68	0.64	1.64	0.06	0.04	2.40	0.67	0.20	0.002	3.02	1.48	0.03	0.15	1.02	0.03	6.50	2.45	9.25	0.03	na	1.29
N	na	48	25	47	50	6	12	5	11	28	29	21	23	45	32	13	21	8	10	36	15	15	na	50
Deposit mean	na	192.1	3.85	19.2	8.61	7.49	0.79	0.20	7.21	1.61	1.76	0.48	22.1	8.98	5.74	0.67	5.36	0.17	24.5	39.8	74.1	0.46	na	42.0
Deposit median	na	43.8	2.47	7.80	6.91	8.50	0.63	0.17	6.03	1.24	0.87	0.05	15.0	4.22	1.23	0.38	3.79	0.19	30.3	21.6	16.3	0.16	na	28.0
TAG-1 mean	na	44.2	1.50	20.3	4.86	5.37	0.68	–	5.32	1.60	0.95	0.75	18.7	4.09	2.3	0.80	5.80	0.10	18.88	39.1	82.6	0.06	na	32.1
TAG-2 mean	–	–	–	–	–	–	–	–	–	–	–	–	–	–	–	–	–	–	–	–	–	–	–	–
TAG-4 mean	na	492.7	6.85	23.5	14.3	10.80	0.99	0.20	8.53	1.70	3.6	0.05	31.23	24.2	6.2	0.22	4.02	0.21	25.49	55.6	16.49	0.47	na	70.4
TAG-5 mean	na	225.6	3.25	7.4	12.7	9.03	0.67	–	9.26	1.30	0.76	0.21	22.76	9.6	31.71	0.38	5.40	0.19	30.29	2.77	21.36	1.23	na	26.0
<i>Sphalerite</i>																								
Maximum	54,302	na	2615	1135	34.5	1.77	1.08	0.39	141.1	40.8	5.28	1.08	900.2	185.4	504.5	120.6	19.3	1.36	18.9	113.8	–	0.07	3023	7.86
Minimum	4449	na	551.0	34.0	0.03	1.77	0.12	0.01	4.13	3.08	0.14	0.005	16.4	4.71	1.95	1.26	0.59	0.01	1.62	0.29	–	0.03	549.2	0.12
N	19	na	19	19	18	1	10	5	15	19	11	11	19	19	19	19	14	16	4	15	–	4	19	13
Deposit mean	24,191	na	1202	307.1	10.3	1.80	0.50	0.14	63.0	17.4	1.02	0.24	240.8	58.5	125.0	41.3	5.60	0.29	10.2	19.6	–	0.04	1364	2.75
Deposit median	13,589	na	1046	231.1	2.25	1.80	0.45	0.10	67.8	17.0	0.50	0.02	116.8	33.6	85.3	28.9	3.35	0.20	10.1	9.60	–	0.03	1286	1.40
TAG-1 mean	–	–	–	–	–	–	–	–	–	–	–	–	–	–	–	–	–	–	–	–	–	–	–	–
TAG-2 mean	5304	na	630.1	296.2	0.70	–	–	–	11.3	4.50	1.00	–	94.8	18.9	30.0	31.8	3.10	0.15	–	–	–	–	567.4	0.50
TAG-4 mean	26,413	na	1269	308.4	11.5	1.80	0.50	0.08	70.9	19.0	1.02	0.29	258.0	63.2	136.2	42.4	5.79	0.31	10.2	19.6	–	0.03	1457	2.94
TAG-5 mean	–	–	–	–	–	–	–	–	–	–	–	–	–	–	–	–	–	–	–	–	–	–	–	–

Summary of LA-ICP-MS data for all trace elements analyzed in this study. '–' indicates no data above minimum detection limits; 'na' indicates data is not applicable (e.g. Fe was used for normalizing). Data are in ppm.

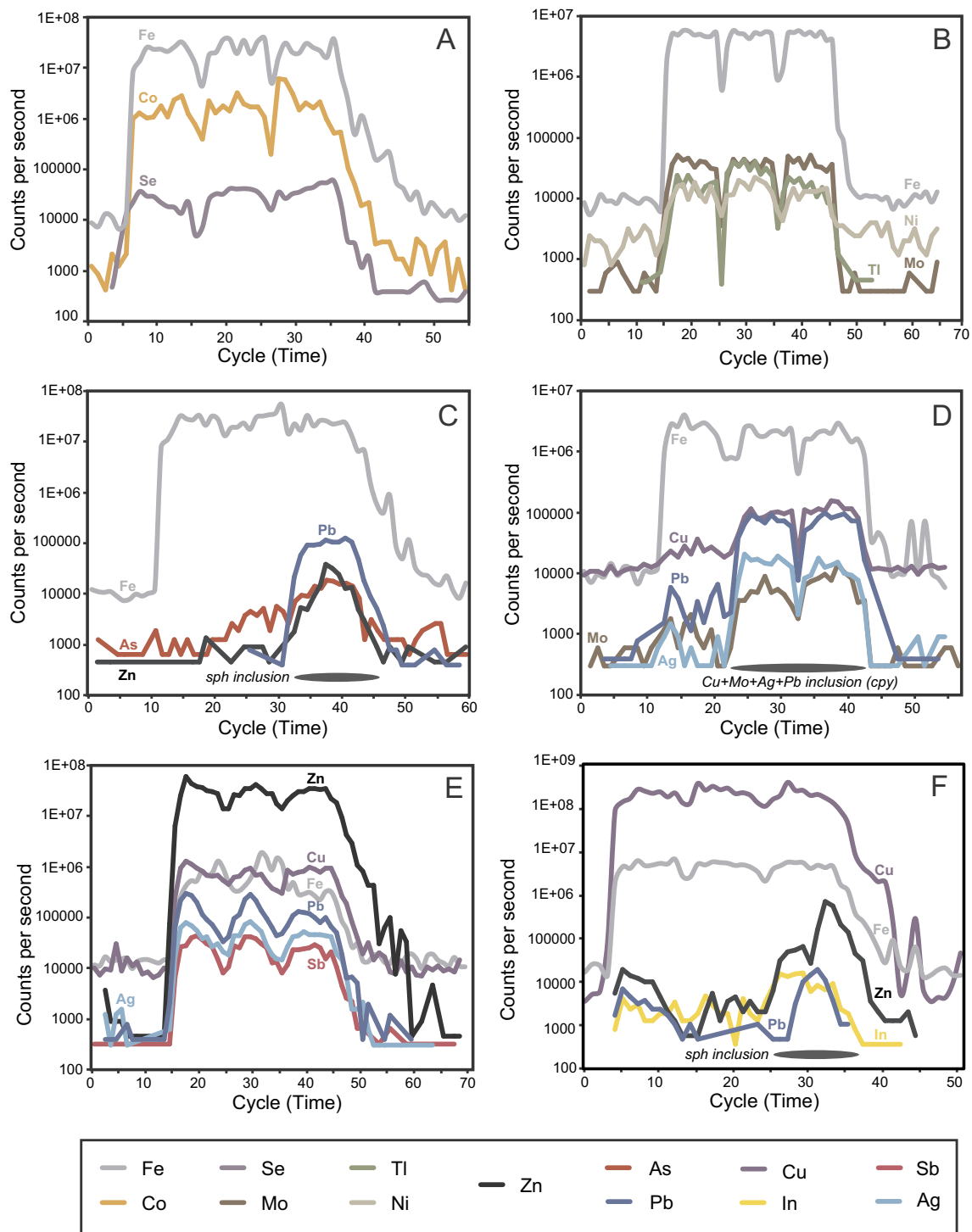


**Fig. 7.** Examples of LA-ICP-MS profiles (time-resolved) for sulfides in the TAG deposit. A) Ablation profile for Py I from sample 957C-7N-2-1D from TAG-1 (21.32 mbsf), showing smooth traces for Fe, Co, and Se. B) Ablation profile for Py IV from sample 957A-3X-1-4 from TAG-2 (10.19 mbsf), showing smooth traces for Fe, Mo, Tl, and Ni. C) Ablation profile for Py II from sample 957K-3X-1-3 from TAG-4 (14.61 mbsf), showing an inclusion of sphalerite with elevated As and Pb. D) Ablation profile for Py IV from sample 957E-9R-1-3 from TAG-5 (40.10 mbsf), showing a large inclusion of chalcopyrite plus elevated Mo, Ag, and Pb. E) Ablation profile for sphalerite from sample 957M-3R-1-11 from TAG-4 (14.71 mbsf), showing smooth traces for Zn, Fe, Cu, Pb, Ag, and Sb, likely all present as lattice substitutions. F) Ablation profile for chalcopyrite from sample 957M-3R-1-11 from TAG-4 (14.71 mbsf), showing a Pb-bearing sphalerite inclusion. The inclusion of chalcopyrite in D is one of the largest observed in the LA profiles (up to 10  $\mu\text{m}$  in size). More typical inclusions (e.g., sphalerite inclusion shown in C) are on the order of 2–4  $\mu\text{m}$ . The sizes are estimated from the ablation times and average depth of the ablation pit (10–12  $\mu\text{m}$ ).

Mo appears to be present in inclusions, associated with Ag, Tl or V (e.g. Fig. 7d), and below ~200 ppm the ablation profiles are similar to Fe and other lattice-bound elements (e.g. Fig. 7b). Ablation profiles for Cu are also irregular or smooth. The upper limit of lattice-hosted Cu in

pyrite appears to be about ~150 ppm; at higher concentrations, the ablation profiles are often spiky. Where Cu shows a positive co-enrichment with Zn, the profiles are irregular, likely indicating co-existence of chalcopyrite and sphalerite inclusions; where there is no Zn,

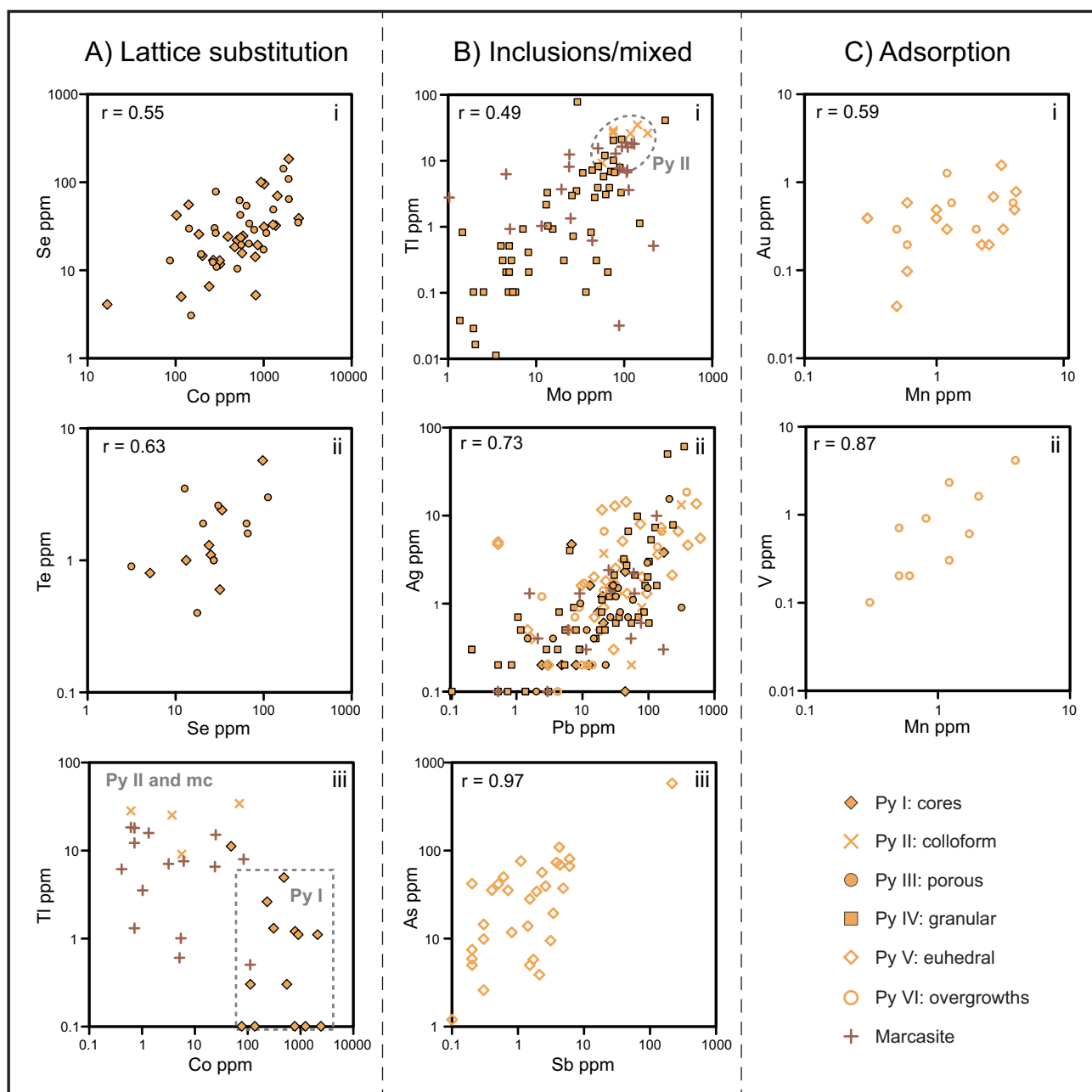


**Fig. 8.** Bivariate plots of LA-ICP-MS data for selected elements in pyrite and marcasite. A) Trace elements likely incorporated by lattice substitution. i) Co and Se in Py I and Py III. ii) Se and Te in Py I and Py III. iii) Co and Tl in Py I, Py II, and marcasite. Pyrite I contains much higher Co and less Tl compared to marcasite and Py II. B) Trace elements incorporated as both lattice substitution and inclusions. i) Mo and Tl in Py IV, Py II and marcasite. Colloform Py II forms a distinct cluster containing high Tl and Mo compared to other types of pyrite. ii) Pb and Ag in marcasite and all pyrite types. Both elements are hosted by inclusions of galena or Pb-Ag-bearing sulfosalts. Most Py I contains no Pb or Ag above detection. iii) Sb and As in Py V. Spiky ablation profiles indicate these elements are mainly hosted by inclusions in Py V. iii) Ag and As in Py II and marcasite. C) Trace elements that are considered to be mainly incorporated by adsorption. i) Mn and Au in late-stage Py V and Py IV. ii) Mn and V in latest stage Py VI overgrowths.

the ablation profiles are typically smooth. Ablation profiles for Pb and Ag are often similar to Fe, even at the highest measured concentrations (Fig. 7d). Because Pb is unlikely to substitute directly into the pyrite lattice in large quantities (see below), it is most likely hosted in pyrite as homogeneously distributed nano-scale particles. The concentrations of Pb and Ag are broadly correlated (Fig. 8a), consistent with the presence of Pb-, Ag-, and potentially Sb- and As-bearing sulfosalts or galena, particularly in colloform Py II (e.g. Fig. 8b). Colloform Py II has significant spikes in Sb, indicating the presence of Sb-bearing inclusions; however, in other pyrite types ablation profiles for Sb are smooth, even at concentrations up to the maximum measured (214 ppm),

suggesting it is lattice-bound or as nano-scale inclusions. Thallium and Mo are also correlated, indicating they may be incorporated into pyrite by similar mechanisms (Fig. 8b). The majority of the ablation profiles for Tl are smooth, particularly in Py I and Py V (Fig. 8a), and therefore likely represent Tl in the pyrite lattice. However, in Py II and Py V, there is a strong positive association of Tl with elements commonly found in sulfosalt inclusions (Ag, Sb, Pb; Table A1.2). Ablation profiles for Cd, Ga, and In indicate that they are likely attributable to micro-inclusions of sphalerite, but the profiles for As indicate that it may be either lattice-bound in pyrite or in micro-inclusions of sphalerite (e.g. Fig. 7c).



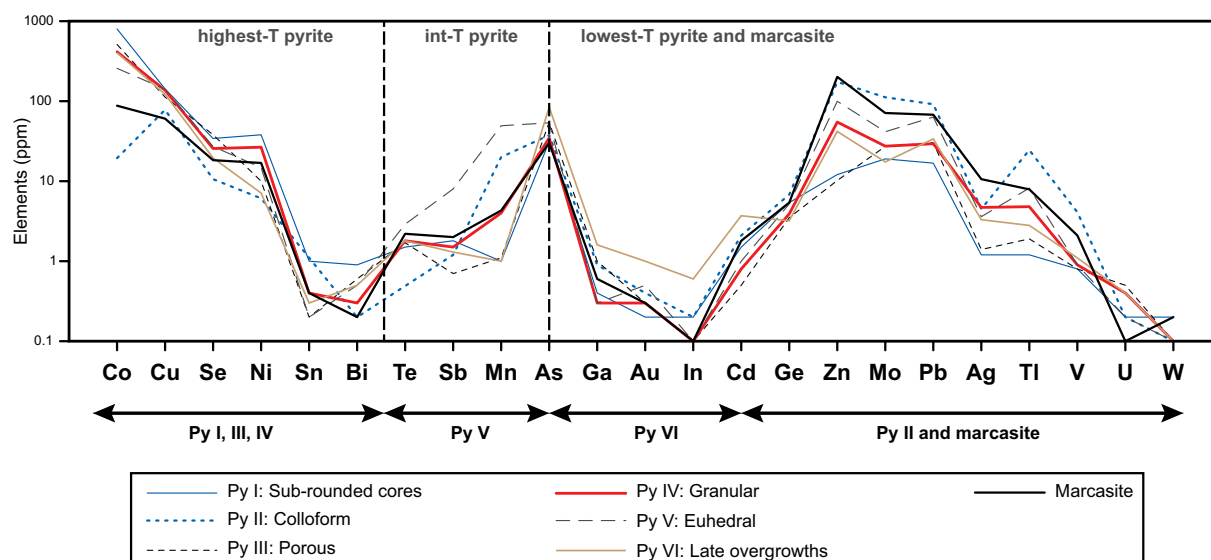


**Fig. 9.** Trace element plot showing the similar overall trace element enrichments and depletions in all pyrite but important differences between some stages of pyrite (and marcasite) growth. Pyrite interpreted to have formed at higher temperatures (Py I, III, and IV) is enriched in Co, Cu, Se, Ni, Sn, and Bi. Pyrite formed at intermediate temperatures (late Py V) is enriched in Sb, As, and Mn. Pyrite formed at the lowest temperatures (Py II and marcasite) is enriched in Zn, Mo, Pb, Ag, and Tl. Plotted values are averages for each element in each pyrite type.

The early Py I cores have the highest concentrations of Co, Cu, Ni and Se and low concentrations of Zn, Ag, Tl, and Mn, particularly in the TAG-5 area. Fine-grained colloform Py II has distinctly higher concentrations of Zn, Pb, Ag, Tl, Ge,  $\pm$  As,  $\pm$  Mn,  $\pm$  Mo,  $\pm$  V,  $\pm$  U compared to early Py I cores in the same samples, and the lowest concentrations of Co, Se, Te, and Bi (Fig. 9). Porous Py III and granular Py IV are variably enriched in Zn, Pb, Ag, Tl, Ge,  $\pm$  As,  $\pm$  Mn (Fig. 9) but also contain high Co and Se, which may have been inherited from earlier Py I. However, Py III has higher Pb and As, and Py I contains more Sn and Ni, confirming their different paragenesis. Euhedral Py V is notably enriched in Zn, Pb, Sb, As, and Mn, consistent with lower temperatures of formation and the presence of micro-inclusions of sphalerite and possibly Mn-oxides. Euhedral Py V also has the highest concentrations of Sb among all pyrite types (Fig. 9). Fig. 10 shows several transects beginning in Py I cores and crossing multiple stages of Py V and ending in Py VI. It shows the increase in Ag, Sb, and Mn and decrease in Co from core to rim, with the most recent Py VI overgrowths being strongly depleted in these elements.

#### 5.2.2. Marcasite

Twenty eight marcasite grains were analyzed in samples from the TAG-1 and TAG-4 areas. The marcasite compositions most closely resemble those of colloform Py II (Fig. 9), except for lower Mn and Tl. Marcasite is enriched in Zn (avg. 201 ppm, up to 1338 ppm), and Pb, Ag, As, Mo, and V are generally higher than in pyrite. Average concentrations of Cu, Co, and Se are low (Fig. 9). Ablation profiles for trace elements in marcasite indicate Co, Se, and Ni are likely lattice-bound, as in pyrite. Copper concentrations below  $\sim$ 115 ppm have relatively smooth ablation profiles, similar to lattice-bound Co and Fe, and above 115 ppm, Cu profiles are irregular and are associated with Zn (e.g. Table A1.3). All Zn analyses have irregular profiles in marcasite and a co-enrichment of Cd and Ga, confirming the presence of sphalerite inclusions (see below). Arsenic appears to be partly lattice-bound but also mimics the spiky Zn ablation profile in some analyses. Lead concentrations above  $\sim$ 70 ppm show irregular ablation profiles, likely from Pb- and Ag-bearing inclusions; below 70 ppm, Pb has a relatively smooth profile and may be hosted within the marcasite lattice or is present as nanoparticles. Thallium and Ag follow Pb where the ablation profiles are smooth. Otherwise, an association of Ag + Pb (and also As + Sb),

with maximum concentrations of 176 ppm Ag and 15.2 ppm Sb, likely indicates Ag + Pb (+ Sb + Tl?) sulfosalt inclusions. At concentrations above  $\sim$ 200 ppm, Mo profiles are spiky and likely indicate the presence of unknown Mo-bearing inclusions; below  $\sim$ 200 ppm, Mo is probably lattice-bound or adsorbed onto the mineral surfaces. Concentrations of Au, In, Sn, Bi, Ni, U, and W are mostly at or below detection.

#### 5.2.3. Sphalerite

Nineteen sphalerite grains were analyzed to identify the likely trace elements associated with sphalerite inclusions in pyrite. Sphalerite with visible chalcopryrite ‘disease’ was avoided. Sphalerite from the outer margins of the mound (TAG-2 and TAG-4 areas) contains 0.79 to 10.19 mol% FeS (avg. 4.39%; Table 4), and is highly enriched in Cd (avg. 1202 ppm, up to 2615 ppm) and Cu (avg. 1364 ppm, up to 3023 ppm). The maximum Cu content is within limits of CuS solubility in sphalerite (Kojima and Sugaki, 1985), and Fe and Cu show no correlation (e.g. Table A1.4) suggesting that sub-microscopic chalcopryrite inclusions were not present in most analyses. Average concentrations of Ge, Ga, and Pb are in the range of 100–1000 ppm, with up to 900 ppm Ge, 1135 ppm Ga, and 505 ppm Pb. Average concentrations of Ag, As, Mn, In, Sb, Co, and Ni are in the range 10–100 ppm with outliers of 185 ppm Ag and 141 ppm As. Average concentrations of Mo, Sn, and V are in the range of 1–10 ppm. Bismuth, Au, W, Tl, and U concentrations are  $< 1$  ppm on average; Se was not detected and only one analysis reported 1.8 ppm Te. Lead, Ag, As, Sb enrichment most often reflect inclusions of galena and/or Pb-bearing sulfosalts, but some smooth ablation profiles also indicate these elements may be lattice-bound or present as nano-scale inclusions of galena and sulfosalts (Fig. 7e). Manganese, Cd, Ga, Ge, and In are present in the sphalerite lattice. They have mostly smooth ablation profiles, although analyses of chalcopryrite (see below) confirm that Ga, Ge, In, and Sn may also be present in very fine-grained inclusions of chalcopryrite. Gallium is negatively correlated with Mn and Fe and positively correlated with Zn and Cd. Concentrations of In in sphalerite correlate negatively with Fe (the highest In is in low-Fe sphalerite; Fig. 13), and the ablation profiles closely match those of Cu, which may indicate a coupled Cu-In substitution for Zn (e.g., Schwarz-Schampera and Herzig, 2002; Cook et al., 2011). Trace Sn correlates with In and Cu in sphalerite, and also may be partly present in chalcopryrite inclusions.

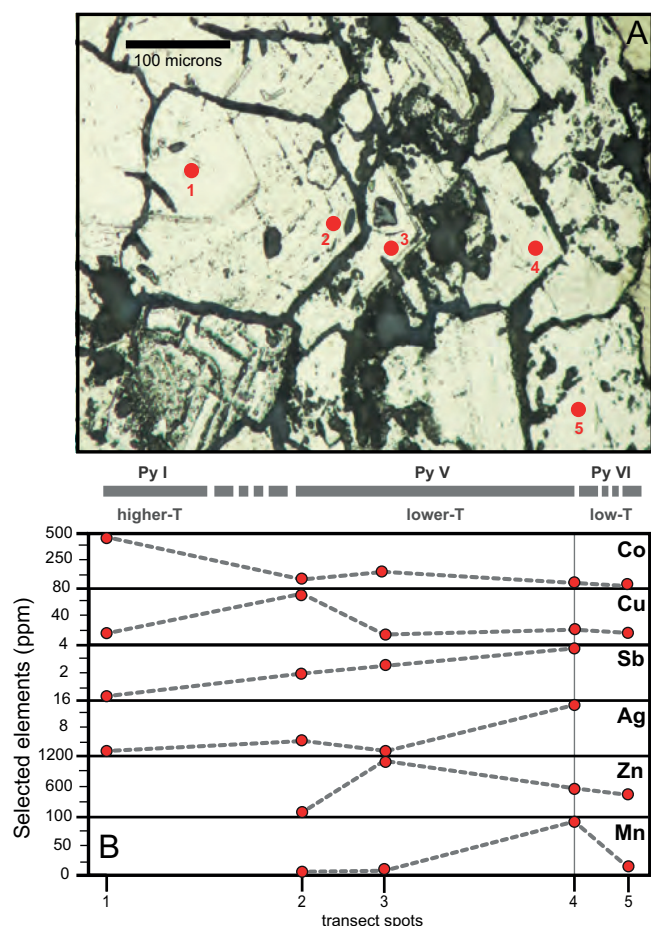


**Fig. 10.** Laser ablation ICP-MS transect across Py I, Py V and Py VI showing changes in element concentrations in different zones. A) Photograph of transect and sampling locations from sub-rounded Py I across multiple generations of euhedral Py V (sample 957F-1N-1-10D from 1.68 mbsf in the TAG-1 area; type 6a). B) Scaled transect for concentrations of selected elements in A, showing decreasing Cu and Co and increasing Sb, Ag, and Mn from the core zone (Py I) to the outer zones (Py V and VI). The vertical solid gray line highlights that after spot 4 trace element concentrations of Co, Cu, Zn, and Mn substantially decrease or are below detection (Ag and Sb). Spot sizes range from 24 to 32  $\mu\text{m}$ , and the transect is approximately 400  $\mu\text{m}$  long.

#### 5.2.4. Chalcopyrite

Fifty chalcopyrite grains in samples from the TAG-1, TAG-4, and TAG-5 areas were analyzed. The average concentration of Zn is 192 ppm, with a maximum of 1967 ppm. Two samples with 1348 and 1422 ppm Zn have smooth ablation profiles similar to Cu and Fe, implying lattice-bound Zn similar to that described by Huston et al. (1995). The concentrations are at the high end of known Zn solubility in chalcopyrite (Kojima and Sugaki, 1985), but the other trace elements that would be expected in sphalerite inclusions (i.e., Cd or Ga) were not present in abundance. Other samples clearly have sphalerite inclusions (Fig. 7f). Average concentrations of Co, Se, Ni, Sn, Ga, and Ge are in the range of 10–100 ppm, with up to 251 ppm Co, 852 ppm Se, 40 ppm Ni, 232 ppm Sn, 184 ppm Ga, and 75 ppm Ge. Average concentrations of Ag, In, As, Cd, Mn, In, Mo, Te, U, and V are in the range of 1–10 ppm, although concentrations of Ag and In reach 56.9 ppm and 52.8 ppm, respectively. Average concentrations of Bi, Au, Sb, Tl, U, and W are < 1 ppm. The ablation profiles of Co, Se, Te, Mo, Ge, In, and Sn are all smooth, indicating that they are present mainly as substitutions in the mineral lattice (e.g., Co and Sn for Fe; In for Cu: Huston et al., 1995). Most of the Ag and As is also hosted in solid solution in chalcopyrite (e.g., Ag for Cu; As for Fe: Cabri, 1992; Huston et al., 1995; Grant et al., 2015; George et al., 2016).

#### 5.2.5. Downhole trace element distributions in pyrite

The downhole distribution of selected trace elements is shown in Fig. 11, and summarized by pyrite type in Fig. 12. Early Py I cores from the upper 15 m of the outer portions of the mound (TAG-4 area) contain trace Pb, Zn, Cu, Ag, and Mn, and less Co, Se, and Bi compared to samples from the interior of the mound to the base of the stockwork zone. Colloform Py II is restricted to the upper part of the TAG-4 area and has variable trace element contents within single samples, particularly inclusion-hosted Cu, Zn, Pb, Tl, and Ag. Porous Py III is restricted to below ~15 mbsf in the interior of the mound and stockwork zone and also has variable trace element contents depending on location and depth in the mound; Co, Se, As, Mo, Ni, and minor Te increase from ~15 mbsf to the base of the mound (especially in TAG-5), and then Co, Se, and Ni increase to the base of the stockwork zone (Fig. 12). Manganese and Tl also decrease in Py III from the upper mound to the base of the mound but are rarely detected in the stockwork zone. Granular Py IV is enriched in Zn, Sb, Tl, Pb, and Ag in the outer portions of the mound (TAG-2 and 4 areas) but contains higher Co, Se and Ni in the interior of the mound and base of the stockwork zone. In Py V, there is also an increase in Co, Se, and Ni at the base of the mound, where low-temperature and seawater-saturated conditions are no longer present, accompanied by a decrease in Zn, Mn, and Pb-Ag-Sb-bearing sulfosalt inclusions. Pyrite VI overgrowths show similar trace element enrichments depending on its location in the mound; Zn, Cd, and Pb decrease in abundance from the top to base of the mound, and Co and Se increase downhole (Fig. 12). Lead, Ag, Mo, V, and Sb are concentrated in Py VI in the more distal and lower-temperature parts of the mound (i.e., TAG-4 area).

## 6. Discussion

The pyrite chemistry is a remarkably good model of the chemistry of the entire deposit, and the detailed paragenesis allows us to comment on the timing and conditions of enrichment of the trace elements. The trends are broadly similar to the downhole variations in bulk geochemistry described by Fouquet et al. (1998) and Herzig et al. (1998). Sub-seafloor variations in trace element concentrations compared to surface samples are confirmed by comparison with published data on pyrite from the surface of the TAG mound (Fig. A1). Early-formed, Py I cores are enriched in elements associated with the highest-temperature stages of mound growth and are geochemically distinct from the other types of pyrite. Colloform Py II and marcasite are enriched in elements associated with lower-temperature hydrothermal upflow. However, recrystallization, replacement, and overgrowths, which reflect the waxing and waning of hydrothermal fluid flow through the mound and stockwork complex, can either expel trace elements or lead to inheritance from one paragenetic stage to another (e.g., Large et al., 2007). By comparison with earlier stages, porous Py III is relatively depleted in trace elements and inclusion-poor, whereas granular Py IV and euhedral Py V are variably enriched in trace elements and inclusions depending on where in the deposit they formed. Late overgrowths of Py VI appear to be mainly enriched in elements from a recent waning stage of hydrothermal activity associated with the deposition of abundant amorphous silica.

Elements associated with the highest-temperature upflow today, particularly Co and Se, and to a lesser extent Mo and As, are enriched in the earliest preserved pyrite. The concentrations increase from the top to the bottom of the stockwork zone. Numerous studies have shown that Co and particularly Se are strongly partitioned into pyrite at high temperatures (> 300 °C) and moderately to strongly reduced conditions (e.g., Yamamoto et al., 1984; Huston et al., 1995; Auclair and Fouquet, 1987; Hannington et al., 1999a, 1999b; Maslennikov et al., 2009, 2017; Revan et al., 2014; Genna and Gaboury, 2015; Keith et al., 2016). Low concentrations of other trace elements in this pyrite suggest that they were either depleted in the earliest high-temperature fluids, were never precipitated (i.e., the fluids did not cool to the point of saturation and

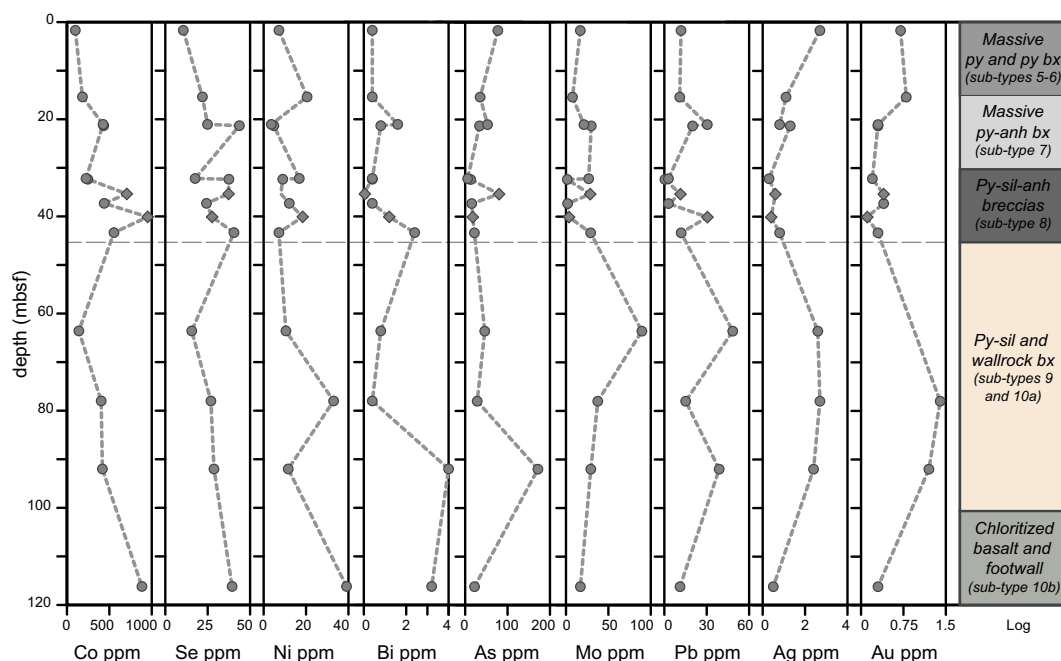


**Fig. 11.** Downhole plots of the average concentrations of selected trace elements in pyrite (all types) from the TAG-1 and TAG-5 areas. Circles indicate samples from TAG-1 and diamonds samples from TAG-5 (Table 3). Mineralization types in the log are detailed in Table 1.

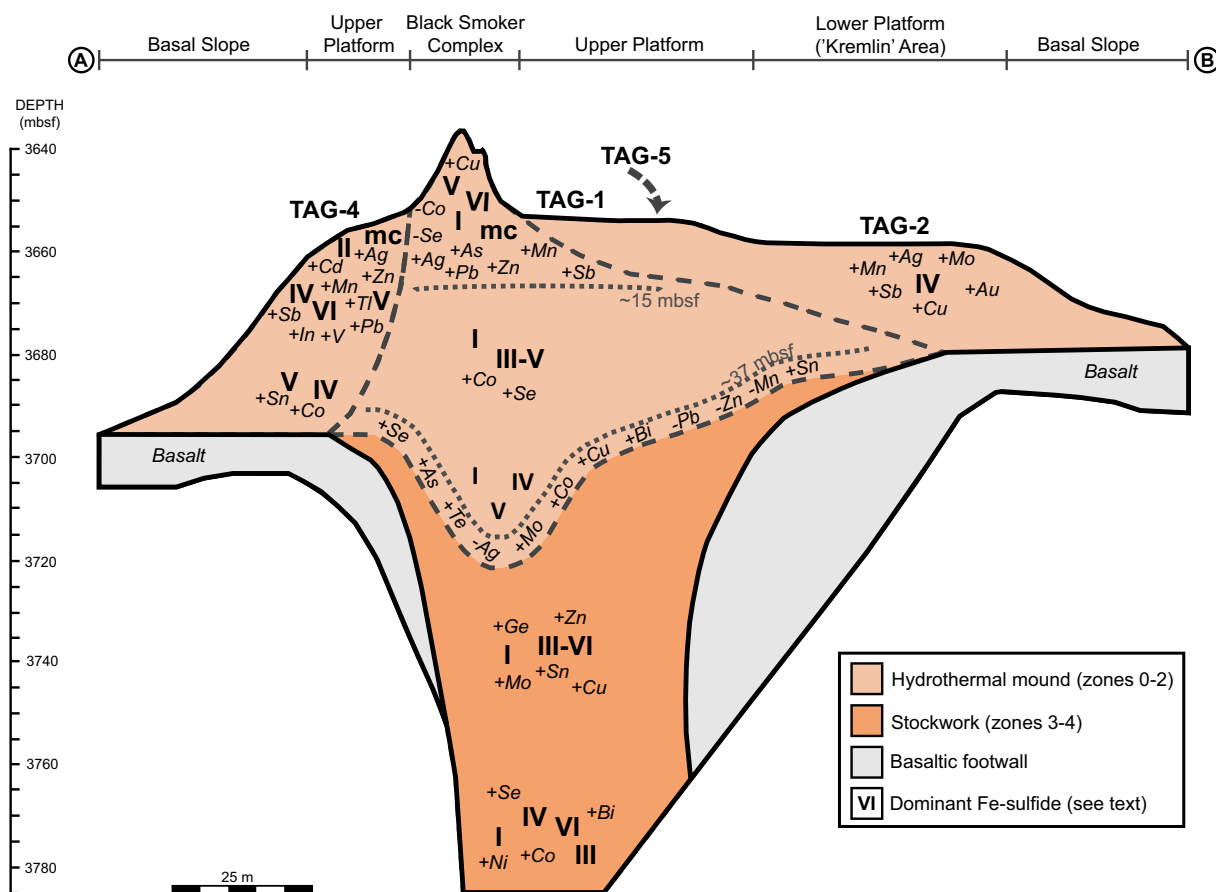


**Fig. 12.** Summary of the location of dominant pyrite types in the TAG deposit and notable enrichments and depletions in trace elements determined by LA-ICP-MS. Elements enriched in pyrite at low-temperatures (Sb, Mn, As, Au, In, Cd, Zn, Mo, Pb, Ag, Tl, V) have their highest concentrations in the upper ~15 mbsf and increase laterally outwards towards the margins of the mound. Elements enriched in pyrite at higher temperatures (Co, Cu, Se, Ni, and Bi) increase in concentration from the surface to base of the mound and decrease laterally outwards. In a narrow zone at the base of the mound (transition from the mound to the stockwork), pyrite shows distinct trace element enrichments (Sn, Se, As, Te, Mo, Co, and Bi) and depletions (Pb, Zn, Mn, and Ag). Cobalt, Cu, Se, Ni, and Bi increase from the base of the mound to the bottom of the stockwork zone.



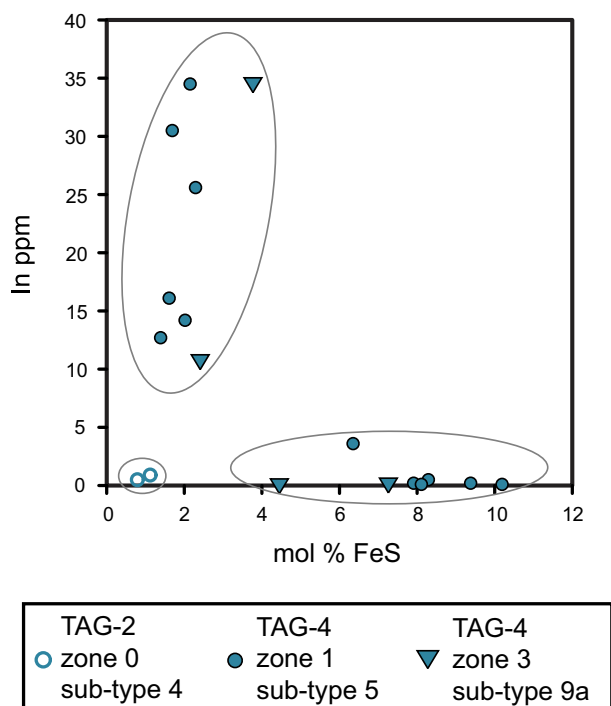


**Fig. 13.** Variations from LA-ICP-MS data of In in sphalerite versus mol % FeS. Three populations are observed: In-bearing but low Fe-sphalerite, low-In and higher-Fe sphalerite, and sphalerite from TAG-2 which is low in both, mol % FeS and In.

the elements were lost to the high-temperature vents), or were stripped from the pyrite during later hydrothermal stages. Some of the coarse-grained pyrite has a large secondary porosity, and low concentrations of trace elements may be due to leaching and strong remobilization. During multiple episodes of zone-refining at TAG (i.e., over-refining, described by Hannington et al., 1998a), recrystallization of lower-

temperature and inclusion-rich pyrite and marcasite liberated trace elements such as Mn, Zn, Cd, Pb, Ag, and Ga that were reincorporated into sulfides at the cooler outer margins of the deposit. Silver shows a distinctly bimodal distribution in pyrite; it is enriched in pyrite from the lower-temperature outer parts of the mound but also in pyrite from the higher-temperature interior of the deposit, reflecting different aqueous complexing of silver at different temperatures (e.g., Hannington et al., 1995: see below).

Elements associated with lower-temperatures are abundant in pyrite with colloform textures (Py II) and in co-existing marcasite, especially in the top 15 m of the deposit (Table 3). The colloform textures are interpreted to indicate rapid, non-equilibrium precipitation, primarily as a result of hydrothermal fluid and seawater mixing (e.g., Large et al., 2007, 2009; Maslennikov et al., 2009, 2017). Marcasite, in particular, is rarely formed at temperatures above ~240 °C (Murowchick and Barnes, 1986). As a result Py II and marcasite are typically inclusion-rich and have high concentrations of trace elements compared to more crystalline, coarser-grained Fe-sulfides (Fig. 9). A notable feature of colloform pyrite, marcasite, and also euhedral Py V, are high Mn concentrations compared to other pyrite stages. These minerals had the greatest exposure to seawater and contain the most Mn and V. Due to the high solubility of Mn in reduced hydrothermal fluids, migrating solutions have the potential to transport Mn farther than many other trace elements, where it may be precipitated directly at low temperature or adsorbed onto surfaces of colloform Fe-sulfides (e.g., Gammons and Seward, 1996; Large et al., 2007). Other trace elements commonly adsorbed from seawater, such as V and U, are also enriched (e.g., Butler and Nesbitt, 1999; Melekestseva et al., 2014; Keith et al., 2016; Melekestseva et al., 2017; Wang et al., 2017). Manganese in late euhedral Py V was likely also scavenged from hydrothermal fluid by slowly growing pyrite crystals in late stage open spaces, particularly near the top of the deposit (Fig. 8c).

#### 6.1. Trace element correlations and principal components analysis

Pearson correlation coefficients for the trace elements in pyrite

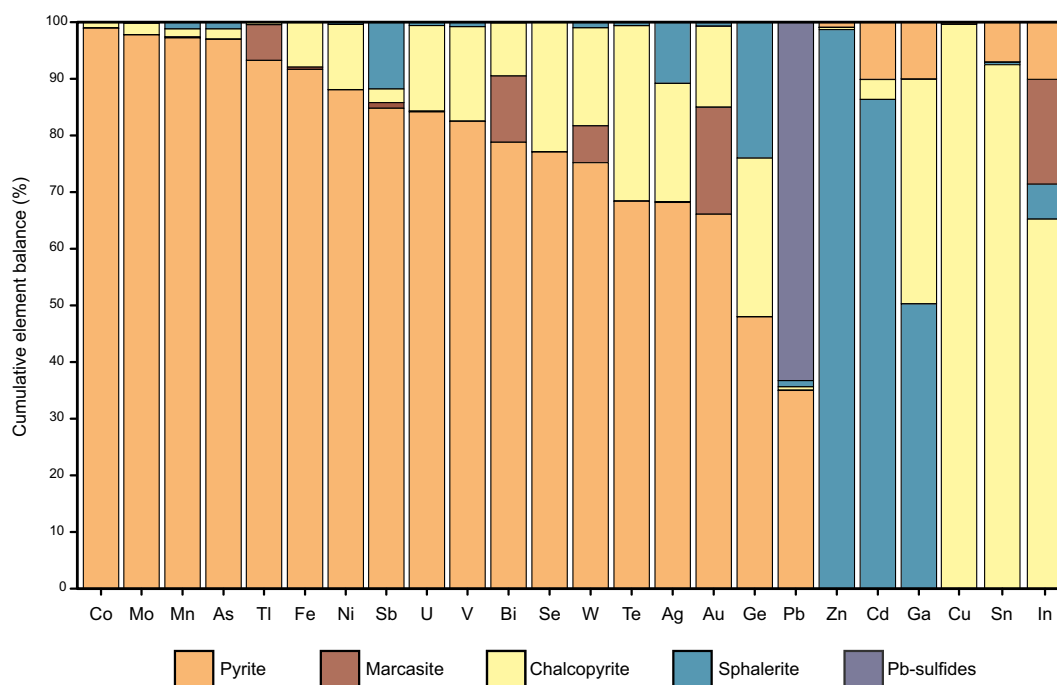


**Fig. 14.** Relative proportions of trace elements in TAG sulfides. Elements are ordered according to the dominant sulfide occurrence (> 50% = dominant) and in decreasing abundance from left to right. The proportions of the trace elements in each mineral were calculated from the LA-ICP-MS data and a normative re-calculation of bulk geochemical assays from ODP Leg 158 (Table 7).

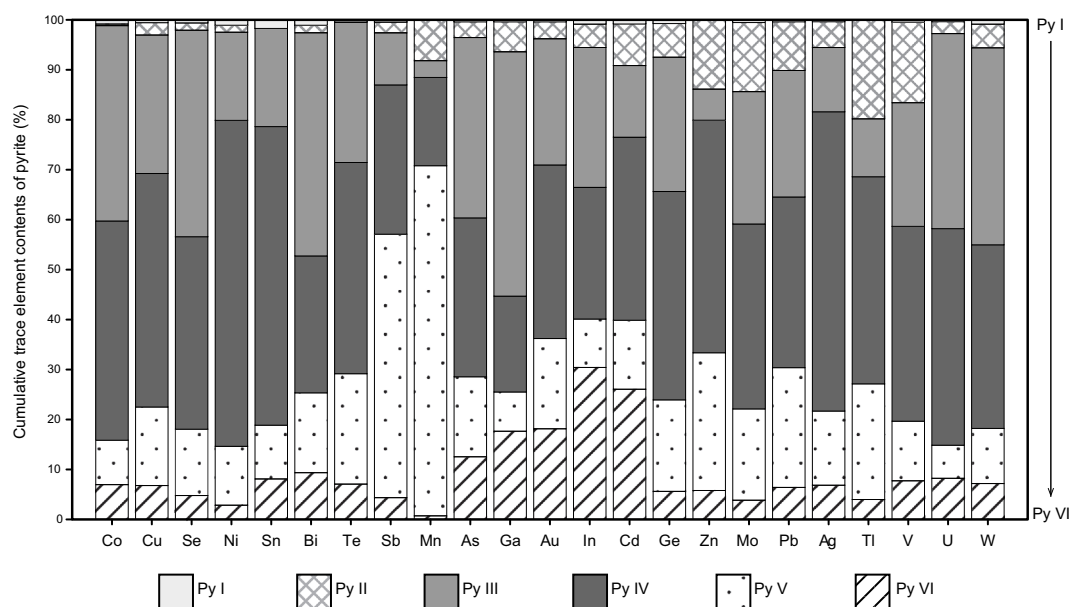


**Fig. 15.** Relative proportions of trace elements in each pyrite stage based on LA-ICP-MS analysis of the different pyrite types and weighted by pyrite type abundance. For each individual trace element, average concentrations for each pyrite type were calculated, multiplied by the % abundance of each pyrite type as estimated from petrography (Table 9), and expressed as a percentage of the total contents of each individual trace element in pyrite overall, weighted by pyrite type abundance. Data are tabulated in Table D1.

show a correlation between Co and Se, reflecting the chemistry of the early Py I cores. Molybdenum has a significant correlation with V and Mn, reflecting the chemistry of colloform Py II and the strong redox behavior of these elements (e.g., Monecke et al., 2016). There is also a positive correlation of Zn, Cd, In, and Ga which belong to the population of trace elements associated with inclusions, especially in Py II and Py V. Lead, Ag, Ge, and to a lesser extent As, Sb, and Tl are strongly correlated, reflecting the chemistry of galena and sulfosalt inclusions in Py II, Py IV, and Py V. Tin is correlated with In and Ge in Py I but also with Ga, Te, and Au, typical of late Py VI overgrowths. There is a weak positive correlation of Bi with In, Co, and Se, but the Bi concentrations are generally very low in all pyrite types.

Principal components analysis (PCA) identifies the high- and low-temperature groupings of elements observed in both the bulk geochemical data and in the pyrite LA-ICP-MS data. These include positive loadings on Factor 1 for Co, Se, and S in the bulk sulfide geochemistry, and negative loadings for Sb, Mn, As, Ga, In, Cd, Zn, Pb, Tl, Au, Ag, and V (Table 5). Germanium, Ni, and SiO<sub>2</sub> in the bulk samples form a distinct group with positive loadings on Factor 2, reflecting the higher-temperature silicification in the interior of the mound, whereas negative loadings for As, Tl, Mo, Mn, and U in the bulk samples reflect lower-temperature mineralization. Positive loadings on Factor 3 for Zn, Cd, and Tl correspond to sphalerite and marcasite mineralization; negative loadings for Ge, In, As, Sb, Mn, Au, V, and U correspond to low-temperature pyrite. Positive loadings on Factor 4 for Cu, Ge, and In corresponds to higher-temperature chalcopyrite mineralization (Table 5). The same factors are evident in the PCA of the pyrite laser ablation data (Table 6): positive loadings for Zn, Cd, Ga, In, Ag, Pb, Tl, Au, Mo, and V (lower-temperature Py II) and negative loadings for Se and Co on Factor 1 (high-temperature Py I); positive loadings for Ge, Pb, Ag, and Tl on Factor 2 (lower-temperature Py II, V and VI) and a separate grouping for Au, In, and Ga associated with later overgrowths (Py VI); positive loadings for Mo, Tl, V, U, W, and Ni on Factor 3 (seawater-dominated elements in low-temperature Py II and Py V); positive loadings for Ag, Au, Pb, Mn, Tl, and Sb on Factor 4 (lower-temperature Py II and Py V), and Co, Se, Bi, Sb, and As on Factor 5 (porous Py III from the center of the mound).

**Table 5**

Results of principal components analysis of bulk-geochemical data summarized in Table 2.

	Factor 1	Factor 2	Factor 3	Factor 4
Eigenvalue	8.39	4.30	2.71	2.55
Variance %	34.32	21.07	13.33	9.98
Cumulative %	34.32	55.39	68.72	78.70
Fe	0.04	−0.45	0.01	−0.19
Zn	−0.31	−0.07	0.35	−0.01
Cd	−0.32	−0.04	0.31	0.03
Ga	−0.32	−0.02	−0.04	0.20
Ge	−0.11	0.25	−0.22	0.29
In	−0.12	−0.13	−0.20	0.40
As	−0.13	−0.31	−0.23	−0.12
Sb	−0.36	−0.09	−0.16	0.04
Ag	−0.37	0.11	−0.05	0.11
Pb	0.30	−0.09	0.07	0.02
Tl	−0.21	−0.21	0.40	−0.04
Mo	−0.03	−0.41	0.11	0.09
Mn	−0.17	−0.25	−0.18	−0.17
Au	−0.31	0.04	−0.21	0.17
Ni	−0.06	0.29	−0.06	−0.12
V	−0.29	−0.02	−0.33	0.05
U	0.01	−0.27	−0.30	−0.13
Co	0.28	−0.13	−0.13	−0.16
Se	0.19	−0.15	−0.11	0.01
Cu	0.06	−0.17	−0.13	0.44
S	0.20	−0.36	0.20	0.15
Ca	0.15	0.09	0.06	0.57
SiO <sub>2</sub>	−0.10	0.45	−0.05	−0.27

Combined datasets of Fouquet et al. (1998), Hannington et al. (1998a, 1998b), and Miller (1998). Factor loadings are ordered according to the percentage of the total variance in the dataset.

## 6.2. Mineral and trace element balances

The proportions of the different trace elements in pyrite (and in other sulfide minerals) were calculated from a combination of the LA-ICP-MS data and a normative recalculation of the bulk geochemical assays from ODP Leg 158 (Table 7 and Fig. 14). Pyrite hosts > 60% of

**Table 6**

Results of principal components analysis of the pyrite LA-ICP-MS data summarized in Table 4.

	Factor 1	Factor 2	Factor 3	Factor 4	Factor 5	Factor 6
Eigenvalue	3.25	2.20	1.79	1.52	1.45	1.38
Variance %	12.99	8.80	7.15	6.08	5.82	5.51
Cumulative %	12.99	21.79	28.94	35.02	40.84	46.34
Zn	0.21	0.07	0.06	0.27	0.01	0.03
Cd	0.23	−0.04	0.06	0.27	0.00	−0.21
Ga	0.28	−0.40	0.05	−0.02	0.03	−0.23
Ge	0.19	0.16	−0.19	−0.16	−0.07	0.25
In	0.20	−0.52	−0.10	−0.08	−0.10	−0.06
As	0.19	0.09	−0.13	0.05	0.37	0.13
Sb	0.11	0.11	−0.03	−0.09	0.44	0.03
Ag	0.26	0.14	−0.28	−0.28	0.05	0.33
Pb	0.30	0.14	−0.05	−0.23	0.19	0.12
Tl	0.21	0.14	0.20	−0.23	0.04	−0.11
Mn	0.08	−0.01	0.01	−0.25	−0.25	−0.02
Au	0.30	−0.34	−0.15	−0.26	−0.22	−0.02
Mo	0.31	0.08	0.25	−0.04	0.30	−0.19
Ni	−0.06	−0.13	0.32	0.05	0.04	0.42
W	0.11	−0.10	0.19	−0.08	−0.23	0.24
V	0.27	0.03	0.42	0.20	0.06	0.13
U	0.14	−0.01	0.19	0.25	0.01	−0.14
Te	−0.14	−0.22	0.01	−0.06	0.19	0.22
Co	−0.19	−0.25	−0.12	0.11	0.32	0.14
Se	−0.26	−0.20	−0.08	−0.04	0.27	0.03
Bi	0.03	−0.36	0.02	−0.06	0.33	−0.02
Sn	0.15	−0.08	−0.31	0.41	−0.12	0.19
Cu	0.22	0.02	−0.35	0.43	−0.03	0.15

Factor loadings are ordered according to the percentage of the total variance in the dataset.

the total As, Sb, Pb, Tl, Au, Ge, Cd, In, Ga, Mo, Te, V, U, W, and Mn, and > 95% of the Co, Se, Ni, Sn, and Bi, but it accounts for only a small proportion of Zn and Cu (0.9 and 0.3%, respectively). Marcasite accounts for significant Au, plus In, Sb, Tl, and W. Chalcopyrite is the dominant sulfide host for Sn and In, plus notable Ge, Ag, Ni, Te, Au, and Ga. Irregular ablation traces for Zn indicate that within chalcopyrite, co-associated Ga (Table A1.4) is most likely in sphalerite inclusions, however recent work by George et al. (2018) shows that chalcopyrite can host tens of ppm Ga in the presence of recrystallized sphalerite. Sphalerite accounts for nearly all of the Cd, but only 50% of the Ga and < 25% of the Ge and In. The proportions of the trace elements in different stages of pyrite growth were estimated from the modal abundance of pyrite in the different paragenetic stages (Table 9) and are summarized in Fig. 15. The results illustrate the timing of different trace element enrichments and depletions through the growth of the deposit. The earliest Py I accounts for < 1% of the total trace element budget of pyrite, even though concentrations of Co and Se in Py I are high (Fig. 15). Low-temperature colloform Py II accounts for 6% of the trace element budget. The most abundant pyrite types, porous Py III and granular Py IV, account for 26% and 39% of the total trace element load, including the highest proportions of Cu, Co, Se, Ni, Sn, Bi, Te, As, Ga, Ge, Mo, Ag, U and W (Table D1). Late-stage euhedral Py V accounts for 19%, including 70% of the Mn and 53% of Sb. The latest Py VI accounts for only 9% of the trace elements in pyrite. These data indicate that relatively few trace elements are deposited in the earliest stages of deposit growth, except for Co and Se, which are strongly partitioned into pyrite at high temperatures. Most trace elements may be lost to the high-temperature hydrothermal discharge at this stage. The majority of trace elements are deposited in pyrite during the main stage of mineralization (Py III and IV), even though pyrite is abundant in earlier and later stages, and only certain elements linked to seawater are enriched in pyrite during the latest stages.

### 6.3. Mechanisms of incorporation of trace metals

Enrichments of As, Sb, Tl, Mo, Zn, Ga, Ge, Cd, In, Au, Pb, Ag, Sb,

**Table 7**  
Calculated proportions of trace elements in sulfides in the TAG mound.

	Total (%)	Sulfide fraction (%)	Fe	Zn	Cd	Ga	In	Te	Au	W	As	Mn	V	U	Ge	Ag	Pb	Sb	Mo	Tl	Ni	Co	Se	Bi	Cu	Sn
Py	65.1	88.8	91.7	0.9	10.1	10.0	10.1	68.4	66.1	75.2	97	97.3	82.5	84.2	48.0	68.2	35.0	84.8	97.8	93.3	88.1	98.9	77.1	78.8	0.3	7.0
Mc	0.3	0.36	0.4	< 0.01	0.02	0.01	18.5	0.03	18.9	6.5	0.04	0.16	< 0.01	0.13	0.02	0.14	0.04	1.0	0.03	6.3	0.03	0.02	0.03	11.7	< 0.01	0.01
Cpy	7.6	10.4	7.9	0.4	3.5	39.7	65.3	31.0	14.3	17.3	1.8	1.4	16.7	15.1	28.0	20.9	0.6	2.4	2.0	0.4	11.5	1.0	22.9	9.4	99.4	92.5
Sph	0.6	0.88	0.04	98.7	86.4	50.3	6.2	0.6	0.7	1.0	1.2	1.2	0.8	0.6	24.0	10.8	1.1	11.8	0.2	0.05	0.4	0.04	bdl	0.1	0.03	0.5
Po	< 0.1	< 0.1	0.01	—	—	—	—	—	—	—	—	—	—	—	—	—	—	—	—	—	—	—	—	—	—	—
Cv	< 0.1	< 0.1	—	—	—	—	—	—	—	—	—	—	—	—	—	—	—	—	—	—	—	—	—	—	0.2	—
Bn	< 0.1	< 0.1	—	—	—	—	—	—	—	—	—	—	—	—	—	—	—	—	—	—	—	—	—	—	0.1	—
Dg	< 0.1	< 0.1	—	—	—	—	—	—	—	—	—	—	—	—	—	—	—	—	—	—	—	—	—	—	0.05	—
Pb-S	< 0.1	< 0.1	—	—	—	—	—	—	—	—	—	—	—	—	—	—	63.3	—	—	—	—	—	—	—	—	—

Calculated proportions of trace elements in each mineral based on normative abundances (calculated from Table 2). Sulfur was assigned in the following order: first anhydrite, then chalcopyrite, sphalerite, pyrrhotite, and galena. Remaining sulfur was then assigned to pyrite and marcasite. The calculation assumes that all Ca is present in anhydrite, all Cu is in Cu-(Fe-) sulfides, all Zn is in sphalerite, and all Pb is in galena. Stoichiometric compositions were used for each mineral. The proportion of marcasite to pyrite was estimated from the petrographic study (Table 3). Using the average compositions of the trace elements in different minerals from LA-ICP-MS data, a mass balance was calculated for each element. The results are summarized in Fig. 15. Abbreviations: Py = pyrite, Mc = marcasite, Cpy = chalcopyrite, Sph = sphalerite, Po = pyrrhotite, Cv = covellite, Bn = bornite, Dg = digenite, Pb-S = galena, bdl = all analyses below detection limit.



**Table 8**  
Summary of possible trace element substitutions in different minerals of the TAG mound.

	Pyrite and Marcasite	Sphalerite	Chalcopyrite
Direct lattice substitution	$[\text{Co}^{2+}, \text{Mo}^{2+}, \text{Ni}^{2+}] \leftrightarrow [\text{Fe}^{2+}]$ $[\text{Se}^{2-}, \text{Te}^{2-}] \leftrightarrow [\text{S}^{2-}]$	$[\text{Fe}^{2+}, \text{Cd}^{2+}, \text{Mn}^{2+}, \text{Co}^{2+}, \text{Mo}^{2+}, \text{Pb}^{2+}, \text{Ni}^{2+}] \leftrightarrow [\text{Zn}^{2+}, \text{Fe}^{2+}]$ $[\text{Fe}^{2+}, \text{Cd}^{2+}] \leftrightarrow [\text{Zn}^{2+}]$ $[\text{Mn}^{2+}, \text{Co}^{2+}, \text{Mo}^{2+}, \text{Pb}^{2+}, \text{Ni}^{2+}] \leftrightarrow [\text{Fe}^{2+}]$	$[\text{Co}^{2+}, \text{Sn}^{2+}, \text{In}^{2+}, \text{Ni}^{2+}, \text{Mo}^{2+}] \leftrightarrow [\text{Fe}^{2+}]$ $[\text{Ag}^{+}, \text{Au}^{+}] \leftrightarrow [\text{Cu}^{+}]$ $[\text{Se}^{2-}, \text{Te}^{2-}] \leftrightarrow 2[\text{S}^{2-}]$
Coupled substitution	$[\text{Ti}^{+}, \text{Cu}^{+}, \text{Au}^{+}] + [\text{As}^{3+}, \text{Sb}^{3+}] \leftrightarrow 2[\text{Fe}^{2+}]$	$[\text{Ag}^{+}, \text{Cu}^{+}, \text{Ti}^{+}, \text{Au}^{+}] + [\text{In}^{3+}, \text{As}^{3+}, \text{Ga}^{3+}, \text{Sn}^{3+}] \leftrightarrow 2[\text{Zn}^{2+}]$ $2[\text{Ag}^{+}, \text{Cu}^{+}, \text{Ti}^{+}, \text{Au}^{+}] + [\text{Fe}^{2+}, \text{Cd}^{2+}, \text{Mn}^{2+}, \text{Co}^{2+}, \text{Mo}^{2+}, \text{Pb}^{2+}, \text{Ni}^{2+}] \leftrightarrow 2[\text{Zn}^{2+}]$	$[\text{Ga}^{3+}, \text{As}^{3+}, \text{Bi}^{3+}] + [\text{Ag}^{+}, \text{Au}^{+}] \leftrightarrow 2[\text{Fe}^{2+}]?$ $[\text{Ge}^{4+}]? \leftrightarrow 2[\text{Fe}^{2+}]?$
Substitution and inclusions (mixed)	$\text{Cu}^{+}, \text{Ti}^{+}, \text{Mo}^{2+}, \text{Sb}^{3+}, \text{As}^{3+}$	$2[\text{Ag}^{+}, \text{Cu}^{+}, \text{Ti}^{+}, \text{Au}^{+}] + [\text{Ge}^{4+}] \leftrightarrow 3[\text{Zn}^{2+}]$	$\text{Ag}^{+}, \text{Pb}^{2+}, \text{Zn}^{2+}, \text{Ni}^{2+}, \text{As}^{3+}$
Inclusions only	$\text{Zn}^{2+}, \text{Cd}^{2+}, \text{Ga}^{3+}, \text{Ge}^{4+}, \text{Au}^{2+}$ (sphalerite)	$\text{Au}^{+}, \text{Ag}^{+}, \text{Cu}^{+}, \text{Pb}^{2+}, \text{Sb}^{3+}, \text{Ge}^{4+}$	$\text{Zn}^{2+}, \text{Cd}^{2+}, (\text{Ga}^{3+}, \text{Ge}^{4+}?)$ sphalerite
Adsorption	$\text{U}^{5+/6+}, \text{V}^{5+}$ ( $\text{Au}^{+?}$ ), $\text{Mn}^{2+}$	( $\text{U}^{5+/6+}, \text{V}^{5+}?$ ) $\text{Mn}^{2+}$	$\text{Mn}^{2+}$ ( $\text{U}^{5+/6+}, \text{V}^{5+}?$ )

**Bold type indicates the most abundant element in a certain sulfide phase, and italics indicate a trace component. See Section 6.3 for discussion. Suggested substitutions are from Scott and Barnes (1971), Roberts (1982), Harris et al. (1984), Fouquet et al. (1988), Cabri (1992), Huston et al. (1995, 1996), Butler and Nesbitt (1999), Todd et al. (2003), Maslennikov et al. (2009), Cook et al. (2009, 2011, 2015), Cook et al. (2012), Grant et al. (2015), Wohlgemuth-Ueberwasser et al. (2015), George et al. (2016), Maslennikov et al. (2017), Wang et al. (2017), Wu et al. (2016), George et al. (2018).**

Mn, V, and U in the lowest-temperature Py II, Py VI, V and marcasite are interpreted to reflect a combination of lattice-bound elements (As, Sb, Tl, Mo), elements in micro-inclusions of sphalerite (Zn, Ga, Ge, Cd, In, Au; Table A1.2), elements in micro-inclusions of sulfosalts or galena (Pb, Ag, Sb), and elements adsorbed onto Fe-sulfide surfaces (Mn, V, U, Au?). Enrichments of Co, Cu, Se, Ni,  $\pm$  Sn,  $\pm$  Te, and  $\pm$  Bi in higher-temperature Py I, III, and IV are interpreted to reflect a combination of lattice-bound elements (Co, Se,  $\pm$  Te,  $\pm$  Ni) and elements in micro-inclusions of chalcopyrite (Cu,  $\pm$  Sn,  $\pm$  Te,  $\pm$  Bi; Table A1.5). Some of the processes inferred for the incorporation of these elements in pyrite and other sulfides are summarized in Table 8. Divalent  $\text{Co}^{2+}$ ,  $\text{Mo}^{2+}$ , and  $\text{Ni}^{2+}$  directly substitute for  $\text{Fe}^{2+}$  in pyrite (e.g. Maslennikov et al., 2009). Monovalent  $\text{Cu}^{+}$  and  $\text{Tl}^{+}$ , trivalent  $\text{As}^{3+}$ , and potentially  $\text{Sb}^{3+}$ , participate in coupled substitutions with two  $\text{Fe}^{2+}$  cations (Huston et al., 1995).  $\text{Se}^{2-}$  and  $\text{Te}^{2-}$  substitute for sulfur (e.g. Maslennikov et al., 2009, Maslennikov et al., 2017).  $\text{Pb}^{2+}$  is least likely to be incorporated into the Fe-sulfide crystal lattice because of its large ionic potential (Z/r ratio), and Pb is mainly present as micro-inclusions of galena or Pb-bearing sulfosalts.

Elements that are mainly present in micro-inclusions are most likely to be controlled by the solubility of the inclusion phase. Elements that are contained in chalcopyrite (e.g. Bi) were likely incorporated in pyrite that formed at high temperatures where chalcopyrite was forming; those contained in sphalerite (e.g., Cd and Ga) were incorporated in pyrite only at temperatures below sphalerite saturation. Other elements probably reflect saturation of complex sulfosalts at different temperatures; for example, Hackbarth and Petersen (1984) showed that low-temperature sulfosalts are generally enriched in Sb, Pb, and Ag, whereas higher-temperature end-members are commonly enriched in As and Cu. This is consistent with the higher As and Cu contents of Py V compared to Py II. Whereas large micro-inclusions are easily identified in LA-ICP-MS profiles (Fig. 7), nanoparticles (< 200 nm) are smaller than the smallest increment of ablation and thus present a smooth profile indistinguishable from a lattice substitution. Particles of this size can be important carriers of trace elements in sulfides (e.g., Palenik et al., 2004; Deditius et al., 2011; Hough et al., 2011; Mikhlin et al., 2011) and may be identified by co-enrichment of elements that occur together in specific mineral phases (e.g., Cd and Zn in sphalerite) or would not be expected to substitute directly into the pyrite structure (e.g., Pb in pyrite). The extent to which nanoparticles follow equilibrium processes remains uncertain. However, it is assumed that, like larger inclusions, their formation is dependent on aqueous solubility of the metals in the fluids from which they formed (Deditius et al., 2011; Gartman and Luther III, 2013), and therefore offer a means to constrain both fluid chemistry and temperatures of mineralization where pyrite is the only well-constrained mineral.

At the lowest-temperatures of pyrite formation (colloform Py II, late euhedral Py V, and marcasite), the incorporation of trace elements may be largely controlled by surface processes, especially elements with strong redox behavior (e.g., Au, V, Mo, Ni, U). Adsorption of charged ions occurs at sites of high positive or negative charge density caused by structural abnormalities such as lattice defects or distortions and fracture planes (Bebie et al., 1998a; Gregory et al., 2014), and is promoted by pH changes that can destabilize aqueous complexes of metals such as during hydrothermal fluid and seawater mixing. Pyrite surfaces are thought to have strong reducing capabilities and, once fixed, the very low solubility of some redox-sensitive elements such as V and U ensures that they are retained by the pyrite (Wersin et al., 1994; Butler and Nesbitt, 1999). Divalent cations such as  $\text{Pb}^{2+}$ ,  $\text{Zn}^{2+}$ , and  $\text{Cd}^{2+}$  and the monovalent  $\text{Au}^{+}$  cation also have been shown to adsorb strongly onto pyrite surfaces (Jean and Bancroft, 1986; Widler and Seward, 2002; Wesolowski et al., 2004).

If we assign different elements to different mechanisms of incorporation – Co, Se, and Ni, (direct lattice substitution); Zn, Cd, Ga, Ge, In, Sn, Au, Pb, Ag, and Bi (inclusions), Te, Mo, Tl, As, Cu, and Sb (both lattice substitution and inclusions); Mn, W, V, U (adsorption) – we

**Table 9**

Summary of mode of occurrence of trace elements in pyrite of different types. See Fig. 15 and section 6.3 for discussion).

%	Py I	Py II	Py III	Py IV	Py V	Py VI
Pyrite type abundance	< 1.0	4	31	43	14	7
Lattice substitution	78.6	6.1	69.4	60.5	38.7	57.4
Inclusions	3.6	47.2	5.9	12.3	22.4	12.0
Mixed	17.6	42.6	24.4	26.5	32.4	30.3
Adsorption	0.2	4.1	0.3	0.7	6.5	0.4

Different elements were assigned to different mechanisms of substitution: Co, Se, and Ni (direct lattice substitution); Zn, Cd, Ga, Ge, In, Sn, Au, Pb, Ag, and Bi (inclusions); Mo, Tl, As, Cu, Te, and Sb (mixed lattice substitution and inclusions); Mn, W, V, and U (adsorption). The proportions of all elements by mechanisms of substitution were determined for each individual trace element by calculating average concentrations for each element by pyrite type, and expressing the trace element contents for each substitution method (e.g. all Co, Se, and Ni hosted by lattice substitution in Py I) as a percentage of the total overall trace element concentrations for each pyrite type.

can make a first-order estimate of the relative importance of each mechanism based on the abundances in each pyrite type (Table 9). Pyrite formed at the highest temperatures (Py I, III, IV) has the greatest proportion of trace elements as lattice substitutions: 61 to 79% of trace elements in these pyrite stages are hosted as lattice substitutions. In low-temperature colloform Py II, only 6% of the total trace elements are hosted as lattice substitutions, compared to 47% as inclusions. Total trace element concentrations in Py V and Py VI are lower overall but mainly hosted by lattice substitution. Pyrite II and Py V incorporate the largest proportion of trace elements by surface adsorption (4 and 6%, respectively).

#### 6.4. Implications for aqueous complexing of trace metals

All of the mechanisms for incorporation of trace elements into pyrite share a dependence on the original aqueous complexing of the metals in the fluids. The major base metals, Cu, Zn, and Pb, and trace elements In, Cd, Mn, and Ag are transported as neutral to weakly-charged chloride complexes in high-temperature saline hydrothermal fluids (Gammons and Seward, 1996; Wood and Samson, 1998; Suleimenov and Seward, 2000; Schwarz-Schampera and Herzig, 2002; Wood and Samson, 2006; Bazarkina et al., 2010). At lower temperatures, aqueous chloride complexes of other metals such as Pb, Ag, In, and Mn, are also stable. Manganese solubility is the highest. The enrichment of Co in early Py I and in Py III at the base of the mound and in the high-temperature stockwork zone is consistent with aqueous transport mainly as chloride complexes in acidic, reduced, saline fluids above 300 °C (Liu et al., 2011; Migdisov et al., 2011). Both Cu and Co show a dramatic decline in the stability of their aqueous chloride complexes below 250 °C (Mountain and Seward, 2003; Liu et al., 2011). The enrichment of Se in pyrite is mainly controlled by the  $\Sigma\text{Se}/\text{S}$  ratio of the hydrothermal fluid, but the strong temperature and pH dependence of the dissociation of  $\text{H}_2\text{Se}$  results in near complete removal of Se from the fluid phase above 300 °C (Huston et al., 1995; Hannington et al., 1999b; Layton-Matthews et al., 2008). The high temperature required to mobilize Se means that it will also be highly immobile in pyrite even after extensive recrystallization (e.g., Large et al., 2007; Thomas et al., 2011; Genna and Gaboury, 2015). Nickel concentrations in most of the TAG pyrite are unexpectedly low, considering the mafic footwall of the deposit. Nickel is only present in the high-temperature Py I cores and granular Py IV and is depleted in lower-temperature stages, as has been noted in other seafloor massive sulfides (e.g., Houghton et al., 2004; Maslennikov et al., 2009). This may reflect the lower solubility of Ni as chloride complexes compared to Co at the same temperature (Liu et al., 2012). In contrast, Mo is found in pyrite throughout the TAG deposit, including in low-temperature marcasite and pyrite (Py II and Py V) and higher-

temperature paragenetic stages (e.g., Py I and Py III). High Mo concentrations in granular Py IV from the top of the mound may be inherited from earlier marcasite. Molybdenum occurs in multiple oxidation states in hydrothermal fluids and is transported as a range of pH- and redox-sensitive oxyanions under different conditions (e.g.,  $\text{H}_2\text{MoO}_4^0$ ,  $\text{HMoO}_4^-$  or  $\text{MoO}_4^{2-}$ ; Seyfried Jr. et al., 2003; Minubayeva and Seward, 2010; Williams-Jones and Migdisov, 2014), which could account for Mo enrichment in all stages of pyrite.

The somewhat different behavior of As and Sb in TAG pyrite suggests differences in aqueous speciation as well as differences in partitioning into the pyrite structure. Antimony concentrations are highest in lower-temperature (< ~250 °C) pyrite towards the cooler outer margins of the deposit in the TAG-2 and TAG-4 areas. Arsenic is found in pyrite throughout the deposit. Arsenic and Sb are mainly transported as neutral hydroxide complexes [e.g.,  $\text{Sb}(\text{OH})_3^0$  and  $\text{As}(\text{OH})_3^0$ ] in low-sulfur hydrothermal solutions (Wood and Samson, 1998), although reduced sulfur and thioarsenite or thioantimonite species [i.e.,  $\text{H}_3(\text{As,Sb})\text{S}_3$  and  $(\text{As,Sb})(\text{HS})_3$ ] may contribute at low temperatures (Seward et al., 2014). Pokrovski et al. (2006) also found that mixed hydroxide-chloride complexes, particularly for Sb, may be important. Like Mo, this may account for the wide range of enrichments in different stages of pyrite growth. Germanium also forms oxyanions, such as  $\text{H}_2\text{GeO}_4^0$  and is transported under conditions similar to Mo, As, and Sb (Wood and Samson, 1998, 2006). Compared to Mo and As, which partition strongly into pyrite at all temperatures, Ge partitions more strongly into sphalerite and chalcopyrite (Fig. 14). Transport of Ge is dominated by neutral to weakly-charged hydroxide complexes [e.g.,  $\text{GaOH}^+$ ,  $\text{Ga}(\text{OH})_3^0$ ], even in hydrothermal fluids that contain reduced sulfur (Wood and Samson, 2006). Gallium partitions preferentially into sphalerite and chalcopyrite, and is particularly associated with Zn, Cd, and In. At low temperatures,  $\text{Ga}^{2+}$  substitutes for  $\text{Zn}^{2+}$  in sphalerite (e.g. Cook et al., 2009), and in the TAG deposit is concentrated in sphalerite inclusion-bearing pyrite at the cooler outer margins, particularly in the TAG-4 area. Indium forms chloride complexes with a large stability range, for example compared to Sn (especially  $\text{InCl}_4^-$ ; Seward et al., 2000), and thus In is incorporated into both chalcopyrite inclusions in high-temperature pyrite and in sphalerite inclusions in lower-temperature pyrite. Tin is most effectively transported as a chloride complex in acidic, reduced hydrothermal fluids at high temperatures (Heinrich and Eadington, 1986; Heinrich, 1990) and is most abundant in pyrite containing micro-inclusions of chalcopyrite, in particular at the transition from stockwork to hydrothermal mound. This is similar to the behavior of Sn observed in many ancient seafloor massive sulfide deposits (e.g. Huston et al., 1995; Hannington et al., 1999a; Grant et al., 2015). Although Bi is present at very low concentrations, it was detected in high-temperature Py I cores and chalcopyrite from the base of the mound. This is consistent with its transport mainly as hydroxide complexes that require temperatures up to 400 °C (Tooth et al., 2013).

Silver may be transported both as chloride and bisulfide complexes depending on the temperature, redox conditions and availability of ligands (Seward, 1976; Gammons and Seward, 1996). In seafloor hydrothermal systems, Ag is mainly transported as a chloride complex ( $\text{AgCl}_2^-$ ) at high temperatures, similar to Cu, In, and Sn, and as a bisulfide complex [ $(\text{Ag}(\text{HS})_2^-)$ ] at low temperatures (e.g., Hannington, 1993; Huston et al., 1996; Grant et al., 2015), spanning the full range of mineralization temperatures documented at TAG. Lower-temperature and more oxidized conditions (e.g., in the TAG-2 area at the top of the mound) favor the precipitation of Ag in micro-inclusions of sulfosalts or galena in Py II, Py V, and marcasite, whereas higher-temperature and more reduced conditions favor incorporation in chalcopyrite by lattice substitution (Huston et al., 1996; Grant et al., 2015). The presence of up to 4.5 ppm Au in pyrite from the TAG 2 area mainly reflects low-temperature transport under weakly acidic to acidic pHs and destabilization of  $\text{AuHS}^0$  complexes by mixing and cooling (Williams-Jones and Migdisov, 2014). High concentrations of Tl in marcasite, colloform

**Table 10**

Estimated minimum concentrations of trace elements in TAG end-member hydrothermal fluid based on pyrite mass balances.

	TAG		EPR	Seawater
	Based on pyrite	Measured	Average	
mg/kg				
Fe	297	297	93	3.E-05
Cu	0.08	7	2.2	0.0002
Zn	0.03	3.1	6.9	0.0003
µg/kg				
Pb	15	21	64	0.0027
Co	185	152	7.8	0.0012
As	19	5	19	1.70
Mo	13	14	4.0	10
Se	12	–	5.7	0.10
Ni	9	–	81	0.53
Mn	5.4	36	–	0.072
Tl	2.2	3.0	6.5	0.014
Ge	1.8	–	–	0.0004
Ag	1.4	5.5	4.0	0.0022
Sb	1.1	–	1.1	0.20
Te	0.8	–	–	5.E-05
Cd	0.53	8.0	9.0	0.079
V	0.42	–	–	2.15
Ga	0.23	17	–	0.0002
Bi	0.19	–	–	4.2E-06
Au	0.17	–	0.08	3.E-05
Sn	0.15	–	–	0.0006
U	0.13	–	–	3.20
In	0.06	0.25	–	0.0001
W	0.04	–	–	0.10

Estimated minimum trace element concentrations of end-member hydrothermal fluids needed to precipitate 1 kg of pyrite with the composition listed in Table 4. Using a Fe concentration in the hydrothermal fluid of 297 mg/kg (average from VentDB; Mottl, 2012), the quantity of fluid required to precipitate 1 kg of pyrite was calculated. The amount of each trace element in 1 kg of pyrite (based on pyrite LA-ICP-MS data in Table 4) was then divided by the quantity of fluid required to account for the trace element load of the pyrite. Data for TAG high-temperature fluids are from Edmond et al. (1995), Edmonds et al. (1996), Charlou et al. (1996), Gamo et al. (1996), and Metz and Trefry (2000). EPR data is from Von Damm et al. (1985) and Hannington et al. (2016). Seawater trace element concentrations are from Li (1991).

pyrite (Py II), and euhedral pyrite (Py V) are consistent with observations in other seafloor hydrothermal systems and are considered a strong indication of low temperatures of formation (100°–250 °C; e.g., Wang et al., 2017). At TAG, there is little or no Tl in the higher-temperature pyrite stages (Py I and Py III) and notable enrichment only in Py II in the TAG-4 area. In saline hydrothermal fluids, below < 200 °C, Tl is transported as the free ion  $Tl^+$  and the neutral species  $TlCl^0$ , however at the temperatures (> 200 °C) inferred for most parts of the deposit (Fig. 5), the dominant Tl species is  $TlCl^0$  (Bebie et al., 1998b).

#### 6.5. Pyrite chemistry as a proxy for fluid compositions

Pyrite chemistry has been widely studied as a proxy for fluid compositions in hydrothermal ore deposits since the first trace metal analyses were possible (e.g., Se, Ni, and Co in pyrite: Loftus-Hills and Solomon, 1967) and more recently in ancient VMS deposits and some black smoker systems (e.g., Auclair and Fouquet, 1987; Huston et al., 1995; Mills, 1995; Houghton et al., 2004). In a simple calculation using the measured Fe concentration of the end-member fluid at TAG, we estimated the amount of fluid needed to precipitate 1 kg of pyrite and then calculated the minimum concentrations of the other elements in the fluid required to account for their concentration in the pyrite (Table 10). The assumptions are that all of the Fe in the fluids is precipitated in pyrite and that the precipitation efficiency is the same for all elements (i.e., all elements are equally partitioned into pyrite in

proportion to their concentrations in the fluid). Calculated fluid concentrations that are higher than expected imply a partition coefficient > 1. The calculations show good agreement with measured vent fluid concentrations for Mo, Ag, Sb, Tl, and Au, which suggests that most of these elements in the TAG fluids are deposited only in pyrite. Higher than expected concentrations of Co, As, and Se (compared to EPR end-member fluid) are partly explained by higher concentrations of Co in the TAG fluids but also likely reflect the strong partitioning of all three elements into pyrite. Estimated concentrations of Cu, Zn, Cd, and Pb needed to precipitate these elements in pyrite are lower than the measured concentrations in the fluids because these elements are partitioned into other minerals. Lower than expected concentrations of Ni, Mn, Ag, Ga, and In implies that most of these elements are also in other minerals or that dissolution and remobilization has affected their concentrations, as previously suggested for fluid compositions at other vent sites (e.g., Metz and Trefry, 2000). Elements for which there are few published vent fluid measurements (e.g., Ge, Te, V, Bi, Sn, W, and U) all yield estimated concentrations in the fluid of 1 ppb or less.

#### 7. Conclusions

The increasing complexity and volume of trace element data on minerals obtained by LA-ICP-MS has challenged the interpretation of results. This study has focused on a single phase with well-constrained conditions of formation to unravel some of the systematic behavior of trace elements in an active seafloor hydrothermal deposit. Pyrite in drill core from the TAG mound and stockwork records the entire paragenetic history of the deposit, from high-temperature black smoker venting, to mineralization in the underlying mound and stockwork zone, and the effects of zone refining. Because it is fairly robust, pyrite also retains more of its original trace element fingerprint during hydrothermal reworking or recrystallization (e.g., Craig and Vokes, 1993; Vaughan and Craig, 1997). Evidence of the early high-temperature evolution of the TAG system is preserved in Co and Se-rich cores of larger pyrite grains; later enrichments in Ga and Tl are an important clue to lower-temperature mineralizing events (cf. Wang et al., 2017). We have shown that secondary pyrite can inherit the trace element signature of earlier marcasite, but some of the less refractory trace elements may be leached from early pyrite during zone refining. Minor and trace element concentrations almost always show consistent enrichments and depletions related to temperature- and redox-dependent aqueous complexing, strong partitioning involving lattice substitutions or surface adsorption, or trapping of micro- or nano-scale inclusions formed at different temperatures, as suggested in previous studies (e.g., Auclair and Fouquet, 1987; Hannington et al., 2005; Hannington, 2014; Monecke et al., 2016). For many trace elements, the concentrations in pyrite reflect temperature-dependent aqueous complexing of the metals and the solubility of the inclusion phases. Cobalt and Se are partitioned into pyrite by lattice substitution across a wide temperature range, but especially at high temperatures (> 300 °C). Some elements, such as Sb, have a bimodal distribution as substitutions in crystal lattices at high temperature and in Pb-Ag-bearing sulfosalts or galena at lower temperature (< 300 °C). Micro- to nano-scale inclusions account for many of the trace metal enrichments in pyrite formed at lower-temperatures. Germanium, In, Sn, Te, and Ag are preferentially included in chalcopyrite; Cd, In, and Ga are strongly partitioned into sphalerite. Concentrations of trace elements that are present in micro- or nano-scale inclusions appear to closely reflect mineral saturation conditions, even if the particular phases cannot be seen, and therefore provide a qualitative geothermometer for pyrite deposition. The common practice of isolating and removing inclusions from LA-ICP-MS data may result in the loss of crucial information about the distribution and abundance of the trace elements in the bulk sulfides and the corresponding fluids. Redox-sensitive trace elements (U, V, Mn, and to some extent Ni and Mo) are fixed by surface adsorption onto pyrite in proportion to the amount of sub-seafloor mixing with seawater. The TAG pyrite data



provide an important baseline against which enrichments and depletions of trace metals in other deposits can be more meaningfully compared. Taking into consideration the different controls, the chemistry of pyrite has the potential to be highly predictive in terms of the conditions of mineral formation over a wide range of temperatures, informing particular stages of ore formation that may lead to enrichment of economically important by-product elements (e.g., Co in VMS and other ore deposit types: Monecke et al., 2016) or highlighting cryptic metal zonation, which has been an important tool in stratigraphic reconstructions of ancient VMS systems (e.g., Cu/Cu + Zn, Pb/Zn + Pb ratios: e.g., Franklin et al., 1981, 2005).

## Acknowledgements

This project was funded by the Cluster of Excellence “The Future Ocean” within the framework of the Excellence Initiative by the Deutsche Forschungsgemeinschaft (DFG) on behalf of the German Federal and State governments. HLJG also acknowledges an Inge-Lehmann-Fonds award from GEOMAR. We thank numerous GEOMAR staff for assistance during this study: D. Rau and M. Thöner for assistance with LA-ICP-MS and microprobe analyses, A. Krätschell and S. Graber for help with data presentation, and J. Clarke for writing a MatLab script for calculation of detection limits. The insightful comments from one anonymous reviewer are greatly appreciated. Declarations of interest: none.

## Appendix A. Supplementary data

Supplementary data to this article can be found online at <https://doi.org/10.1016/j.chemgeo.2018.08.019>.

## References

- Alt, J.C., Teagle, D.A.H., 1998. Probing the TAG hydrothermal mound and stockwork: oxygen-isotopic profiles from deep ocean drilling. In: Herzig, P.M., Humphris, S.E., Zierenberg, R.A. (Eds.), *Proc. ODP Sci. Results*, 158: College Station, TX (Ocean Drilling Program)pp. 285–295.
- Auclair, G., Fouquet, Y., 1987. Distribution of selenium in high-temperature hydrothermal sulfide deposits at 13°N, East Pacific Rise. *Can. Mineral.* 25, 577–587.
- Bazarkina, E.F., Pokrovski, G.S., Zotov, A.V., Hazemann, J.-L., 2010. Structure and stability of cadmium chloride complexes in hydrothermal fluids. *Chem. Geol.* 276, 1–17.
- Beaulieu, S.E., Baker, E.T., German, C.R., Maffei, A., 2013. An authoritative global database for active submarine hydrothermal vents. *Geochim. Geophys. Geosyst.* 14, 4892–4905.
- Bebie, J., Schoonen, M.A.A., Fuhrmann, M., Strongin, D.R., 1998a. Surface charge development on transition metal sulfides: an electrokinetic study. *Geochim. Cosmochim. Acta* 62, 633–642.
- Bebie, J., Seward, T.M., Hovey, J.K., 1998b. Spectrophotometric determination of the stability of thallium (I) chloride complexes in aqueous solution up to 200 °C. *Geochim. Cosmochim. Acta* 62, 1643–1651.
- Becker, K., von Herzen, R.P., 1996. Pre-drilling observations of conductive heat flow at the TAG active mound using ALVIN. In: Humphris, S.E., Herzig, P.M., Miller, D.J. (Eds.), *Proc. ODP Init. Repts.*, 158. College Station, TX (Ocean Drilling Program)pp. 23–29.
- Belousov, I., Large, R.R., Meffre, S., Danyushevsky, L.V., Steadman, J., Beardsmore, T., 2016. Pyrite compositions from VHMS and orogenic Au deposits in the Yilgarn Craton, Western Australia: Implications for gold and copper exploration. *Ore Geol. Rev.* 79, 474–499.
- Beltenev, V.E., Lazareva, L.I., Cherkashev, G.A., Ivanov, V.I., Rozhdestvenskaya, V.A., Kuznetsov, I.I., Laiba, A.A., Narkevskiy, E.V., 2017. New hydrothermal sulfide fields of the Mid-Atlantic Ridge: Yubileinoe (20°09'N) and Surprise (20°45.4'N). *Dokl. Earth Sci.* 476, 1010–1015.
- Bogdanov, Y.A., Lein, A.Y., Maslennikov, V.V., Li, S., Ulyanov, A.A., 2008. Mineralogical-geochemical features of sulfide ores from the Broken Spur hydrothermal field. *Oceanology* 48, 679–700.
- Butler, L.B., Nesbitt, R.W., 1999. Trace element distributions in the chalcopyrite wall of a black smoker chimney: insights from laser ablation inductively-coupled plasma mass spectrometry (LA-ICP-MS). *Earth Planet. Sci. Lett.* 167, 335–345.
- Cabri, L.J., 1992. The distribution of trace precious metals in minerals and mineral products. *Mineral. Mag.* 56, 289–308.
- Campbell, A.C., Palmer, M.R., Klinkhammer, G.P., Bowers, T.S., Edmond, J.M., Lawrence, J.R., Casey, J.F., Thompson, G., Humphris, S., Rona, P., Karons, J.A., 1988. Chemistry of hot springs on the Mid-Atlantic Ridge. *Nature* 335, 514–518.
- Charlou, J.-L., Fouquet, Y., Donval, J.P., Auzende, J.M., Baptiste, P.J., Stievenard, M., Michel, S., 1996. Mineral and gas chemistry of hydrothermal fluids on an ultrafast spreading ridge: East Pacific Rise, 17° to 19°S (Nadur cruise, 1993) phase separation processes controlled by volcanic and tectonic activity. *J. Geophys. Res.* 101 (B7), 15,899–15,919.
- Cook, N.J., 1996. Mineralogy of the sulphide deposits at Sulitjelma, northern Norway. *Ore Geol. Rev.* 11, 303–338.
- Cook, N.J., Ciobanu, C.L., Pring, A., Skinner, W., Shimizu, M., Danyushevsky, L., Saini-Eidukat, B., Melcher, F., 2009. Trace and minor elements in sphalerite: a LA-ICP-MS study. *Geochim. Cosmochim. Acta* 73, 4761–4791.
- Cook, N.J., Ciobanu, C.L., Williams, T., 2011. The mineralogy and mineral chemistry of indium in sulphide deposits and implications for mineral processing. *Hydrometallurgy* 108, 226–228.
- Cook, N.J., Ciobanu, C.L., Brugger, J., Etschmann, B., Howard, D.L., de Jonge, M.D., Ryan, C., Paterson, D., 2012. Determination of the oxidation state of Cu in substituted Cu-In-Fe-bearing sphalerite via mu-XANES spectroscopy. *Am. Mineral.* 97, 476–479.
- Cook, N.J., Etschmann, B., Ciobanu, C.L., Geraki, K., Howard, D., Williams, W., Rae, N., Pring, A., Chen, G., Johannessen, B., Brugger, J., 2015. Distribution and substitution mechanism of Ge in a Ge-(Fe)-bearing sphalerite. *Fortschr. Mineral.* 5, 117–132.
- Craddock, P.R., Bach, W., 2010. Insights into magmatic-hydrothermal processes in the Manus back-arc basin as recorded by anhydrite. *Geochim. Cosmochim. Acta* 74, 5514–5536.
- Craig, J.R., Vokes, F.M., 1993. Post-recrystallisation mobilisation phenomena in metamorphosed stratabound sulphide ores. *Mineral. Mag.* 57, 3–19.
- Craig, J.R., Vokes, F.M., Solberg, T.N., 1998. Pyrite: physical and chemical textures. *Mineral. Deposita* 34, 82–101.
- Deditius, A.P., Utsunomiya, S., Reich, M., Kesler, S.E., Ewing, R.C., Hough, R., Walshe, J., 2011. Trace nanoparticles in pyrite. *Ore Geol. Rev.* 42, 32–46.
- Dehnavi, A.S., McFarlane, C.R.M., Lentz, D.R., Walker, J.A., 2018. Assessment of pyrite composition by LA-ICP-MS techniques from massive sulfide deposits of the Bathurst Mining Camp, Canada: from textural and chemical evolution to its application as a vectoring tool for the exploration of VMS deposits. *Ore Geol. Rev.* 92, 656–671.
- Dekov, V.W., Garbe-Schönberg, D., Kamenov, G.D., Guéguen, B., Bayon, G., Bindi, L., Asael, D., Fouquet, Y., 2018. Redox changes in a seafloor hydrothermal system recorded in hematite-chalcopyrite chimneys. *Chem. Geol.* 483, 351–371.
- Dusel-Bacon, C., Slack, J.F., Koenig, A.E., Foley, N.K., Oscarson, R.L., Gans, K.D., 2011. Whole-rock and sulfide-minerals geochemical data from volcanogenic massive sulfide deposits of the Boninfield District, East Central Alaska. In: USGS Open File 2011-1171, pp. 47.
- Edmond, J.M., Campbell, A.C., Palmer, M.R., Klinkhammer, G.P., German, C.R., Edmonds, H.N., Elderfield, H., Thompson, G., Rona, P., 1995. Time series studies of vent fluids from the TAG and MARK sites (1986, 1990) Mid-Atlantic Ridge: a new solution chemistry model and a mechanism for Cu/Zn zonation in massive sulphide ore bodies. In: Parson, L.M., Walker, C.L., Dixon, D.R. (Eds.), *Hydrothermal Vents and Processes*. Geological Society of London Special Publication, pp. 77–86.
- Edmonds, H.N., German, C.R., Green, D.R.H., Huh, Y., Gamo, T., Edmond, J.M., 1996. Continuation of the hydrothermal fluid chemistry time series at TAG, and the effects of ODP drilling. *Geophys. Res. Lett.* 23, 3487–3489.
- Fietzke, J., Frische, M., 2016. Experimental evaluation of elemental behavior during LA-ICP-MS: influences of plasma conditions and limits of plasma robustness. *J. Anal. At. Spectrom.* 31, 234–244.
- Fietzke, J., Liebetrau, V., Gunther, D., Gürs, K., Hametner, K., Zumholtz, K., Hansteen, T.H., Eisenhauer, A., 2008. An alternative data acquisition and evaluation strategy for improved isotope ratio precision using LA-MC-ICP-MS applied to stable and radiogenic strontium isotopes in carbonates. *J. Anal. At. Spectrom.* 23, 955–961.
- Fouquet, Y., Auclair, G., Cambon, P., Etoubeau, J., 1988. Geological setting and mineralogical and geochemical investigations on sulfide deposits near 13°N on the East Pacific Rise. *Mar. Geol.* 84, 145–178.
- Fouquet, Y., Henry, K., Knott, R., Gambon, P., 1998. Geochemical section of the TAG hydrothermal mound. In: Herzig, P.M., Humphris, S.E., Zierenberg, R.A. (Eds.), *Proc. ODP Sci. Results*, 158: College Station, TX (Ocean Drilling Program)pp. 363–387.
- Franklin, J.M., Gibson, H.L., Jonasson, I.R., Galley, A.G., 2005. Volcanogenic massive sulfide deposits. *Econ. Geol.* 100, 523–560.
- Franklin, J.M., Sangster, D.M., Lydon, J.W., 1981. Volcanic-associated massive sulfide deposits. *Econ. Geol.* 75, 485–627.
- Gammons, C.H., Seward, T.M., 1996. Stability of manganese(II) chloride complexes from 25 to 300 °C. *Geochim. Cosmochim. Acta* 60, 4295–4311.
- Gamo, T., Chiba, H., Masuda, H., Edmonds, H.N., Fujioka, K., Kodama, Y., Nanba, H., Sano, Y., 1996. Chemical characteristics of hydrothermal fluids from the TAG mound of the mid-Atlantic Ridge in August 1994: implications for spatial and temporal variability of hydrothermal activity. *Geophys. Res. Lett.* 23, 3483–3486.
- Gartman, A., Luther III, G.W., 2013. Comparison of pyrite (FeS<sub>2</sub>) synthesis mechanisms to reproduce natural FeS<sub>2</sub> nanoparticles found at hydrothermal vents. *Geochim. Cosmochim. Acta* 120, 447–458.
- Genna, D., Gaboury, D., 2015. Deciphering the hydrothermal evolution of a VMS system by LA-ICP-MS using trace elements in pyrite: an example from the Bracemac-McLeod deposits, Abitibi, Canada, and implications for exploration. *Econ. Geol.* 110, 2087–2108.
- George, L.L., Cook, N.J., Ciobanu, C.L., 2016. Partitioning of trace elements in co-crystallized sphalerite-galena-chalcopyrite hydrothermal ores. *Ore Geol. Rev.* 77, 97–116.
- George, L.L., Cook, N.J., Ciobanu, C.L., Wade, B.P., 2015. Trace and minor elements in galena: a reconnaissance LA-ICP-MS study. *Am. Mineral.* 100, 548–569.
- George, L.L., Cook, N.J., Crowe, B.B.P., Ciobanu, C.L., 2018. Trace elements in hydrothermal chalcopyrite. *Mineral. Mag.* 82, 59–88.
- German, C.R., Higgs, N.C., Thomson, J., Mills, R., Elderfield, H., Blusztajn, J., Fleer, A.P., Bacon, M.P., 1993. A geochemical study of metalliferous sediment from the TAG hydrothermal mound, 26°08'N, Mid-Atlantic Ridge. *J. Geophys. Res.* 98, 9683–9692.

- Grant, H.L.J., Layton-Matthews, D., Peter, J.M., 2015. Distribution and controls on silver mineralization in the Hackett River Main Zone, Nunavut, Canada: an Ag- and Pb-enriched Archean volcanogenic massive sulfide deposit. *Econ. Geol.* 110, 943–982.
- Gregory, D., Meffre, S., Large, R., 2014. Comparison of metal enrichment in pyrite from boulders from a metal-enriched and metal-poor estuary. *Am. Mineral.* 99, 633–644.
- Hackbarth, C.J., Petersen, U., 1984. A fractional crystallization model for the deposition of argentic tetrahedrite. *Econ. Geol.* 79, 448–460.
- Halbach, P., Blum, M., Münch, U., Plüger, W., Garbe-Schönberg, D., Zimmer, M., 1998. Formation and decay of a modern massive sulfide deposit in the Indian Ocean. *Mineral. Deposita* 33, 302–309.
- Hannington, M.D., 1993. Formation of atacamite during weathering of sulfides on the modern seafloor. *Can. Mineral.* 31, 945–956.
- Hannington, M.D., 2014. Volcanogenic massive sulfide deposits. In: Scott, S.D. (Ed.), *Treatise on Geochemistry*, Second Edition. vol. 13. Elsevier, pp. 463–488.
- Hannington, M.D., Bleeker, W., Kjarsgaard, I., 1999a. Sulfide mineralogy, geochemistry, and ore genesis of the Kidd Creek Deposit: part I. north, central, and south orebodies. *Econ. Geol. Monogr.* 10, 163–224.
- Hannington, M.D., Bleeker, W., Kjarsgaard, I., 1999b. Sulfide mineralogy, geochemistry, and ore genesis of the Kidd Creek Deposit: part II. the Bornite Zone. *Econ. Geol. Monogr.* 10, 225–266.
- Hannington, M.D., de Ronde, C.E.J., Petersen, S., 2005. Sea-floor tectonics and submarine hydrothermal systems. *Econ. Geol.* 100, 111–141.
- Hannington, M.D., Galley, A.G., Herzig, P.M., Petersen, S., 1998a. Comparison of the TAG mound and stockwork complex with Cyprus-type massive sulfide deposits. In: Herzig, P.M., Humphris, S.E., Zierenberg, R.A. (Eds.), *Proc. ODP Sci. Results*, 158: College Station, TX (Ocean Drilling Program)pp. 389–415.
- Hannington, M.D., Herzig, P.M., Petersen, S., Gregorie, D.C., Belanger, P., 1998b. Data report: major and trace element geochemistry of shipboard samples from site 957, TAG hydrothermal field, Mid-Atlantic Ridge. In: Herzig, P.M., Humphris, S.E., Zierenberg, R.A. (Eds.), *Proc. ODP Sci. Results*, 158: College Station, TX (Ocean Drilling Program)pp. 27–39.
- Hannington, M.D., Tivey, M.K., Larocque, A.C.L., Petersen, S., Rona, P.A., 1995. The occurrence of gold in sulfide deposits of the TAG hydrothermal field, Mid-Atlantic Ridge. *Can. Mineral.* 33, 1285–1310.
- Hannington, M.D., Harðardóttir, V., Garbe-Schönberg, D., Brown, K.L., 2016. Gold enrichment in active geothermal systems by accumulating colloidal suspensions. *Nat. Geosci.* 9 (4), 299–302.
- Harris, D.C., Cabri, L.J., Nobiling, R., 1984. Silver-bearing chalcopyrite, a principal source of silver in the Izok Lake massive-sulfide deposit: confirmation by electron- and proton-microprobe analyses. *Can. Mineral.* 28, 189–206.
- Heinrich, C.A., 1990. The chemistry of hydrothermal tin (-tungsten) ore deposition. *Econ. Geol.* 85, 457–481.
- Heinrich, C.A., Eadington, P.J., 1986. Thermodynamic predictions of the hydrothermal chemistry of arsenic, and their significance for the paragenetic sequence of some cassiterite-arsenopyrite-base metal sulfide deposits. *Econ. Geol.* 81, 511–529.
- Herzig, P.M., Petersen, S., Hannington, M.D., 1998. Geochemistry and sulfur-isotope composition of the TAG hydrothermal mound, Mid-Atlantic Ridge, 26°N. In: Herzig, P.M., Humphris, S.E., Zierenberg, R.A. (Eds.), *Proc. ODP Sci. Results*, 158: College Station, TX (Ocean Drilling Program)pp. 47–70.
- Hough, R.M., Noble, R.R.P., Reich, M., 2011. Natural gold nanoparticles. *Ore Geol. Rev.* 42, 55–61.
- Houghton, J.L., Shanks III, W.C., Seyfried Jr., W.E., 2004. Massive sulfide deposition and trace element remobilization in the Middle Valley sediment-hosted hydrothermal system, northern Juan de Fuca Ridge. *Geochim. Cosmochim. Acta* 68, 2863–2873.
- Humphris, S.E., Herzig, P.M., Miller, D.J., Alt, J.C., Becker, K., Brown, D., Brugmann, G., Chiba, H., Fouquet, F., Gemmell, J.B., Guerin, G., Hannington, M.D., Holm, N.G., Honnorez, J.J., Petersen, P., Reysenbach, A.-L., Rona, P.A., Smith, S., Sturz, A.A., Tivey, M.K., Zhao, X., 1995a. The internal structure of an active sea-floor massive sulphide deposit. *Nature* 377, 713–716.
- Humphris, S.E., Herzig, P.M., Miller, D.J., et al., 1995b. *Proc. ODP, Init. Repts.*, 158: College Station, TX (Ocean Drilling Program). <https://doi.org/10.2973/odp.proc.ir.158.1996>.
- Humphris, S.E., Kleinrock, M.C., 1996. Detailed morphology of the TAG active hydrothermal mound: Insights into its formation and growth. *Geophys. Res. Lett.* 23, 3443–3446.
- Humphris, S.E., Tivey, M.K., 2000. A synthesis of geological and geochemical investigations of the TAG hydrothermal field: insights into fluid-flow and mixing processes in a hydrothermal system. In: Dilek, Y., Moores, E.M., Elthon, D., Nicolas, A. (Eds.), *Ophiolites and Oceanic Crust: New Insights from Field Studies and the Ocean Drilling Program: Geological Society of America Special Paper* 349, Boulder, Colorado, pp. 213–235.
- Humphris, S.E., Tivey, M.K., Tivey, M.A., 2015. The Trans-Atlantic Geotraverse hydrothermal field: a hydrothermal system on an active detachment fault. *Deep-Sea Res. II Top. Stud. Oceanogr.* 121, 8–16.
- Huston, D.L., Jablonski, W., Sie, S.-H., 1996. The distribution and mineral hosts of silver in eastern Australian volcanogenic massive sulphide deposits. *Can. Mineral.* 34, 529–546.
- Huston, D.L., Sie, S.-H., Suter, G.F., Cooke, D.R., 1995. Trace elements in sulfide minerals from Eastern Australian volcanic-hosted massive sulfide deposits: part I. proton microprobe analyses of pyrite, chalcopyrite, and sphalerite, and part II. selenium levels in pyrite: comparison with  $\delta^{34}\text{S}$  values and implications for the source of sulfur in volcanogenic hydrothermal systems. *Econ. Geol.* 90, 1167–1196.
- James, R.H., Elderfield, H., 1996. Chemistry of ore-forming fluids and mineral formation rates in an active hydrothermal sulfide deposit on the Mid-Atlantic Ridge. *Geology* 24, 1147–1150.
- Jean, G.E., Bancroft, G.M., 1986. Heavy metal adsorption by sulphide mineral surfaces. *Geochim. Cosmochim. Acta* 50, 1455–1463.
- Jochum, K.P., Stoll, B., Herwig, K., Willbold, M., Hofmann, A.W., Amini, M., Aarburg, S., Abouchami, W., Hellebrand, E., Mocek, B., Raczek, I., Stracke, A., Alard, O., Bouman, C., Becker, S., Dücking, M., Brätz, H., Klemm, R., de Bruijn, D., Canil, D., Cornell, D., de Hoog, C.-J., Dalpe, C., Danyushevsky, L.V., Eisenhauer, A., Gao, Y., Snow, J.E., Groschopf, N., Gunther, D., Latkoczy, C., Guillong, M., Hauri, E.H., Höfer, H.E., Lahaye, Y., Horz, K., Jacob, D.E., Kasemann, S.E., Kent, A.J.R., Ludwig, T., Zack, T., Mason, P.R.D., Meixner, A., Rosner, M., Misawa, K., Nash, B.P., Pfänder, J., Premo, W.R., Sun, W.D., Tiepolo, M., Vannucci, R., Vennemann, T., Wayne, D., Woodhead, J.D., 2006. MPI-DING reference glasses for in-situ microanalysis: New reference values for element concentrations and isotope ratios. *Geochim. Geophys. Geosyst.* 7. <https://doi.org/10.1029/2005GC001060>.
- Keith, M., Häckel, F., Haase, K.M., Schwarz-Schampera, U., Klemm, R., 2016. Trace element systematics of pyrite from submarine hydrothermal vents. *Ore Geol. Rev.* 72, 728–745.
- Kleinrock, M.C., Humphris, S.E., The Deep-TAG Team, 1996. Detailed structure and morphology of the TAG active hydrothermal mound and its geotectonic environment. In: Humphris, S.E., Herzig, P.M., Miller, D.J. (Eds.), *Proc. ODP Init. Repts.*, 158. College Station, TX (Ocean Drilling Program)pp. 15–21.
- Knott, R., Fouquet, Y., Honnorez, J., Petersen, S., Bohn, M., 1998. Petrology of hydrothermal mineralization: a vertical section through the TAG mound. In: Herzig, P.M., Humphris, S.E., Zierenberg, R.A. (Eds.), *Proc. ODP Sci. Results*, 158: College Station, TX (Ocean Drilling Program)pp. 5–26.
- Kojima, S., Sugaki, A., 1985. Phase relations in the Cu-Fe-Zn-S system between 500 °C and 300 °C under hydrothermal conditions. *Econ. Geol.* 80, 158–171.
- Krasnov, S.G., Cherkashev, G.A., Stepanova, T.V., Batuyev, B.N., Krotov, A.G., Malin, B.V., Maslov, M.N., Markov, V.F., Poroshina, I.M., Samovarov, M.S., Ashadze, A.M., Lazareva, L.I., Ermolayev, I.K., 1995. Detailed geological studies of hydrothermal fields in the North Atlantic. In: Parson, L.M., Walker, C.L., Dixon, D.R. (Eds.), *Hydrothermal Vents and Processes. Geological Society of London Special Publications*, pp. 43–64.
- Lalou, C., Reyss, J.-L., Brichet, E., 1998. Age of sub-bottom sulfide samples at the TAG active mound. In: Herzig, P.M., Humphris, S.E., Zierenberg, R.A. (Eds.), *Proc. ODP Sci. Results*, 158: College Station, TX (Ocean Drilling Program)pp. 111–117.
- Lalou, C., Reyss, J.-L., Brichet, E., Arnold, M., Thompson, G., Fouquet, Y., Rona, P.A., 1993. New age data for Mid-Atlantic Ridge hydrothermal sites: TAG and Snakepit chronology revisited. *J. Geophys. Res.* 96, 9705–9713.
- Large, R.R., Danyushevsky, L.V., Hollit, C., Maslennikov, V.V., Meffre, S., Gilbert, S., Bull, S., Scott, R., Emsbo, P., Thomas, H., Singh, B., Foster, J., 2009. Gold and trace element zonation in pyrite using a laser imaging technique: Implications for the timing of gold in orogenic and Carlin-style sediment-hosted deposits. *Econ. Geol.* 104, 635–668.
- Large, R.R., Maslennikov, V.V., Robert, F., Danyushevsky, L.V., Chang, Z., 2007. Multistage sedimentary and metamorphic origin of pyrite and gold in the giant Sukhoi Log deposit, Lena Gold Province, Russia. *Econ. Geol.* 102, 1233–1267.
- Layton-Matthews, D., Peter, J.M., Scott, S.D., Leybourne, M.I., 2008. Distribution, Mineralogy, and geochemistry of selenium in felsic volcanic-hosted massive sulfide deposits of the Finlayson Lake district, Yukon Territory, Canada. *Econ. Geol.* 103, 61–88.
- Lein, A.Y., Bogdanov, Y.A., Maslennikov, V.V., Li, S., Ulyanova, N.V., Maslennikova, S.P., Ulyanov, A.A., 2010. Sulfide minerals in the Menez Gwen nonmetallic hydrothermal field (Mid-Atlantic Ridge). *Lithol. Miner. Resour.* 45, 305–323.
- Leistel, J.M., Marcoux, E., Deschamps, Y., Joubert, M., 1998. Antithetic behavior of gold in the volcanogenic massive sulphide deposits of the Iberian Pyrite Belt. *Mineral. Deposita* 33, 82–97.
- Li, X., Maslennikov, V.V., Lein, A.Y., Ulyanov, A.A., 2012. Associations of trace elements in the sulfides of black smokers from the Broken Spur, Menez Gwen, and Snake Pit hydrothermal fields. *Mosc. Univ. Geol. Bull.* 67, 8–17.
- Li, Y.-H., 1991. Distribution patterns of elements in the oceans: a synthesis. *Geochim. Cosmochim. Acta* 55, 3233–3240.
- Lisitsin, A.P., Bogdanov, Y.A., Zonenshayn, L.P., Kuz'min, M.I., Sagalevich, A.M., 1989. Hydrothermal phenomena in the Mid-Atlantic Ridge at lat. 26°N (TAG hydrothermal field). *Int. Geol. Rev.* 31, 1183–1189.
- Liu, W., Borg, S.J., Testemale, D., Etschmann, B., Hazemann, J.-L., Brugger, J., 2011. Speciation and thermodynamic properties for cobalt chloride complexes in hydrothermal fluids at 35–440 °C and 600 bar: an in-situ XAS study. *Geochim. Cosmochim. Acta* 75, 1227–1248.
- Liu, W., Migdisov, A., Williams-Jones, A.E., 2012. The stability of aqueous nickel(II) chloride complexes in hydrothermal solutions: results of UV-visible spectroscopic experiments. *Geochim. Cosmochim. Acta* 94, 276–290.
- Lockington, J.A., Cook, N.J., Ciobanu, C.L., 2014. Trace and minor elements in sphalerite from metamorphosed sulphide deposits. *Mineral. Mag.* 108, 873–890.
- Loftus-Hills, G., Solomon, M., 1967. Cobalt, nickel, and selenium in sulphides as indicators of ore genesis. *Mineral. Deposita* 2, 228–242.
- Maslennikov, V.V., Maslennikova, S.P., Large, R.R., Danyushevsky, L., 2009. Study of Trace Element zonation in vent chimneys from the Silurian Yaman-Kasy volcanic-hosted massive sulfide deposit (Southern Urals, Russia) using laser ablation-inductively coupled plasma mass spectrometry (LA-ICPMS). *Econ. Geol.* 104, 111–141.
- Maslennikov, V.V., Maslennikova, S.P., Large, R.R., Danyushevsky, L., Herrington, R.J., Ayupova, N.R., Zaykov, V.V., Lein, A.Y., Tseluyko, A.S., Melekestseva, I.Yu., Tsalalina, S.G., 2017. Chimneys in Paleozoic massive sulfide mounds of the Urals VMS deposits: Mineral and trace element comparison with modern black, grey, white, and clear smokers. *Ore Geol. Rev.* 85, 64–106.
- Maslennikov, V.V., Maslennikova, S.P., Large, R.R., Danyushevsky, L., Herrington, R.J., Stanley, C.J., 2013. Tellurium-bearing minerals in zoned sulfide chimneys from Cu-Zn massive sulfide deposits of the Urals, Russia. *Mineral. Petrol.* 107, 67–99.

- McClenaghan, S.H., Lentz, D.R., Martin, J., Diegor, W.G., 2009. Gold in the Brunswick No. 12 volcanogenic massive sulfide deposit, Bathurst Mining Camp, Canada: evidence from bulk ore analysis and laser ablation ICP-MS data on sulfide phases. *Mineral. Deposita* 44, 523–557.
- McIntire, W.L., 1963. Trace element partition coefficients – a review of theory and applications to geology. *Geochim. Cosmochim. Acta* 27, 1209–1264.
- Melekestseva, I.Y., Maslennikov, Y.V., Tret'yakov, G.A., Nimis, P., Beltenev, V.E., Rozhdvestenskaya, I.I., Maslennikova, S.P., Belogub, E.V., Danyushevsky, L.V., Large, R.R., Yuminov, A.M., Sadyk'ov, S.A., 2017. Gold- and silver-rich massive sulfides from the Semenov-2 hydrothermal field, 13°31.13' N, Mid-Atlantic Ridge: a case of magmatic contribution? *Econ. Geol.* 112, 741–773.
- Melekestseva, I.Y., Tret'yakov, G.A., Nimis, P., Yuminov, A.M., Maslennikov, Y.V., Maslennikova, S.P., Kotlyarov, V.A., Beltenev, V.E., Danyushevsky, L.V., Large, R., 2014. Barite-rich massive sulfides from the Semenov-1 hydrothermal field (Mid-Atlantic Ridge, 13°30.87' N): Evidence for phase separation and magmatic input. *Mar. Geol.* 349, 37–54.
- Metz, S., Trefry, J.H., 2000. Chemical and mineralogical influences on concentrations of trace metals in hydrothermal fluids. *Geochim. Cosmochim. Acta* 64, 2267–2279.
- Migdisov, A.A., Zevin, D., Williams-Jones, A.E., 2011. An experimental study of cobalt (II) complexation in  $\text{Cl}^-$  and  $\text{H}_2\text{S}$ -bearing hydrothermal solutions. *Geochim. Cosmochim. Acta* 75, 4065–4079.
- Mikhlin, Y., Romanchenko, A., Likhatski, M., Karacharov, A., Erenburg, S., Trubina, S., 2011. Understanding the initial stages of precious metal precipitation: Nanoscale metallic and sulfidic species of gold and silver on pyrite surfaces. *Ore Geol. Rev.* 42, 47–54.
- Miller, D.J., 1998. Data report: geochemical analyses of massive sulfide and sediment samples from the TAG hydrothermal mound. In: Herzig, P.M., Humphris, S.E., Zierenberg, R.A. (Eds.), *Proc. ODP Sci. Results*, 158: College Station, TX (Ocean Drilling Program) pp. 41–46.
- Mills, R.A., 1995. Hydrothermal deposits and metalliferous sediments from TAG, 26°N Mid-Atlantic Ridge. In: Parson, L.M., Walker, C.L., Dixon, D.R. (Eds.), *Hydrothermal Vents and Processes*. Geological Society of London Special Publication, pp. 77–86.
- Minubayeva, Z., Seward, T.M., 2010. Molybdenic acid ionization under hydrothermal conditions to 300°C. *Geochim. Cosmochim. Acta* 74, 4365–4374.
- Monecke, T., Petersen, S., Hannington, M.D., Grant, H.L.J., Samson, I., 2016. The Minor Element endowment of modern sea-floor massive sulfides and comparison with deposits hosted in ancient volcanic successions. *Rev. Econ. Geol.* 18, 245–306.
- Mottl, M.J., 2012. *VENT Data Collections*. EarthChem Library <https://doi.org/10.1594/IEDA/100207>.
- Mountain, B.W., Seward, T.M., 2003. Hydrosulfide/sulfide complexes of copper(I): Experimental confirmation of the stoichiometry and stability of  $\text{Cu}(\text{HS})_2^{2-}$  to elevated temperatures. *Geochim. Cosmochim. Acta* 67, 3005–3014.
- Murowchick, J.B., 1992. Marcasite inversion and petrographic determination of pyrite ancestry. *Econ. Geol.* 87, 1141–1152.
- Murowchick, J.B., Barnes, H.L., 1986. Marcasite precipitation from hydrothermal solutions. *Geochim. Cosmochim. Acta* 50, 2615–2629.
- Palenik, C.S., Utsunomiya, S., Reich, M., Kesler, S.E., Wang, L., Ewing, R.C., 2004. “Invisible” gold revealed: Direct imaging of gold nanoparticles in a Carlin-type deposit. *Am. Mineral.* 89, 1359–1366.
- Parker, C.M., von Damm, K.L., 2005. Time series fluid compositions from the TAG hydrothermal Mound, MAR: 1986–2004. In: American Geophysical Union, Fall Meeting 2005, abstract, #OS22A-07.
- Petersen, S., Herzig, P.M., Hannington, M.D., 1998. Fluid inclusion studies as a guide to the temperature regime within the TAG hydrothermal mound, 26°N, Mid-Atlantic Ridge. In: Herzig, P.M., Humphris, S.E., Zierenberg, R.A. (Eds.), *Proc. ODP Sci. Results*, 158: College Station, TX (Ocean Drilling Program) pp. 163–178.
- Petersen, S., Herzig, P.M., Hannington, M.D., 2000. Third dimension of a presently forming VMS deposit: TAG hydrothermal mound, Mid-Atlantic Ridge, 26°N. *Mineral. Deposita* 35, 233–259.
- Petersen, S., Krättschell, A., Augustin, N., Jamieson, J.W., Hein, J.R., Hannington, M.D., 2016. News from the seabed - geological characteristics and resource potential of deep-sea mineral resources. *Mar. Policy* 70, 175–187.
- Pokrovski, G.S., Borisova, A.Y., Roux, J., Hazemann, J.L., Petdang, A., Tella, M., Testemale, D., 2006. Antimony speciation in saline hydrothermal fluids: a combined X-ray absorption fine structure spectroscopy and solubility study. *Geochimica et Cosmochimica Acta* 70, 4196–4214.
- Pontbriand, C.W., Sohn, R.A., 2014. Microearthquake evidence for reaction-driven cracking within the Trans-Atlantic Geotraverse active hydrothermal deposit. *J. Geophys. Res. Solid Earth* 119, 822–839.
- Purdy, G.M., Sempere, J.-C., Schouten, H., Goldsmith, R., 1990. Bathymetry of the Mid-Atlantic Ridge, 24°–31°N: a map series. *Mar. Geophys. Res.* 12, 247–252.
- Revan, M.K., Genc, Y., Maslennikov, V.V., Maslennikova, S.P., Large, R.R., Danyushevsky, L.V., 2014. Mineralogy and trace-element geochemistry of sulfide minerals in hydrothermal chimneys from the Upper Cretaceous VMS deposits of the eastern Pontide orogenic belt (NE Turkey). *Ore Geol. Rev.* 63, 129–149.
- Reves-Sohn, R., Humphris, S., Canales, J.P., 2004. Cruise Report: Seismicity and Fluid Flow of the TAG Hydrothermal Mound-4. Woods Hole Oceanographic Institution, Woods Hole, Massachusetts.
- Roberts, F.I., 1982. Trace element chemistry of pyrite: A useful guide to the occurrence of sulfide base metal mineralization. *J. Geochem. Explor.* 17, 49–62.
- Roman, C., Singh, H., 2007. A self-consistent bathymetric mapping algorithm. *Journal of Field Robotics* 2, 26–51.
- Rona, P.A., 1980. TAG hydrothermal field: Mid-Atlantic Ridge crest at latitude 26°N. *J. Geol. Soc. Lond.* 137, 385–402.
- Rona, P.A., Bogdanov, Y.A., Gurvich, E.G., Rimski-Korsakov, N.A., Hannington, M.D., Thompson, G., 1993b. Relict hydrothermal zones in the TAG hydrothermal field, Mid-Atlantic Ridge 26°N, 45°W. *J. Geophys. Res.* 98, 9715–9730.
- Rona, P.A., Hannington, M.D., Raman, C.V., Thompson, G., Tivey, M.K., Humphris, S.E., Lalou, C., Petersen, S., 1993a. Active and relict sea-floor hydrothermal mineralization at the TAG hydrothermal field, Mid-Atlantic Ridge. *Econ. Geol.* 88, 1989–2017.
- Schwarz-Schampera, U., Herzig, P.M., 2002. *Indium – Geology, Mineralogy and Economics*. Springer, Berlin, pp. 257.
- Scott, R.B., Rona, P.A., McGregor, B.A., Scott, M.R., 1974. The TAG hydrothermal field. *Nature* 251, 301–302.
- Scott, S.D., Barnes, H.L., 1971. Sphalerite geothermometry and geobarometry. *Econ. Geol.* 66, 653–669.
- Sempere, J.-C., Purdy, G.M., Schouten, H., 1990. Segmentation of the Mid-Atlantic Ridge between 24°N and 30°40'N. *Nature* 344, 427–431.
- Seward, T.M., 1976. The stability of chloride complexes of silver in hydrothermal solutions up to 350 °Celsius. *Geochim. Cosmochim. Acta* 40, 1329–1341.
- Seward, T.M., Henderson, C.M.B., Charnock, J.M., 2000. Indium(III) chloride complexing and solvation in hydrothermal systems to 350 °C: an EXAFS study. *Chem. Geol.* 167, 117–127.
- Seward, T.M., Williams-Jones, A.E., Migdisov, A.A., 2014. The chemistry of metal transport and deposition by ore-forming hydrothermal fluids. In: Scott, S.D. (Ed.), *Treatise on Geochemistry*, Second Edition. vol. 13. Elsevier, pp. 29–57.
- Seyfried Jr., W.E., Seewald, J.S., Berndt, M.E., Ding, K., Foustoukos, D.I., 2003. Chemistry of hydrothermal vent fluids from the Main Endeavour Field, northern Juan de Fuca Ridge: geochemical controls in the aftermath of June 1999 seismic events. *J. Geophys. Res.* 108. <https://doi.org/10.1029/2002JB001957>.
- Slack, J.F., Shanks III, W.C., Karl, S.M., Gemery, P.A., Bittenbender, P.E., Ridley, W.L., 2005. Geochemical and Sulfur Isotopic Signature of Volcanogenic Massive Sulfide Deposits on Prince of Wales Island and Vicinity, Southeastern Alaska. USGS Professional Paper 1732-C. pp. 37.
- Sohn, R.A., 2007. Stochastic analysis of exit fluid temperature records from the active TAG hydrothermal mound (Mid-Atlantic Ridge, 26°N): I. Modes of variability and implications for subsurface flow. *J. Geophys. Res.* 112, B07101. <https://doi.org/10.1029/2006JB004335>.
- Suleimenov, O.M., Seward, T.M., 2000. Spectrophotometric measurements of metal complex formation at high temperatures: the stability of Mn(II) chloride species. *Chem. Geol.* 167, 177–192.
- Thomas, H.V., Large, R.R., Bull, S.W., Maslennikov, V.V., Berry, R.F., Fraser, R., Froud, S., Moye, R., 2011. Pyrite and pyrrhotite textures and composition in sediments, laminated quartz veins, and reefs at Bendigo Gold Mine, Australia: insights for ore genesis. *Econ. Geol.* 106, 1–31.
- Thompson, G., Mottl, M.J., Rona, P.A., 1985. Morphology, mineralogy and chemistry of hydrothermal deposits from the TAG area, 26°N, Mid-Atlantic Ridge. *Chem. Geol.* 49, 243–257.
- Tivey, M.A., Schouten, H., Kleinrock, M.C., 2003. A near-bottom magnetic survey of the Mid-Atlantic Ridge axis at 26°N: implications for the tectonic evolution of the TAG segment. *J. Geophys. Res.* 108 (B5), 2277. <https://doi.org/10.1029/2002JB001967>.
- Tivey, M.K., Humphris, S.E., Thompson, G., Hannington, M.D., Rona, P.A., 1995. Deducing patterns of fluid flow and mixing within the TAG active hydrothermal mound using mineralogical and geochemical data. *J. Geophys. Res.* 100 (B7), 12,527–12,555.
- Tivey, M.K., Mills, R.A., Teagle, D.A.H., 1998. Temperature and salinity of fluid inclusions in anhydrite as indicators of seawater entrainment and heating in the TAG active mound. In: Herzig, P.M., Humphris, S.E., Zierenberg, R.A. (Eds.), *Proc. ODP Sci. Results*, 158: College Station, TX (Ocean Drilling Program) pp. 179–190.
- Todd, E.C., Sherman, D., Purton, J., 2003. Surface oxidation of chalcopyrite ( $\text{CuFeS}_2$ ) under ambient atmospheric and aqueous (pH 2–10) conditions: Cu, Fe L and O K-edge X-ray spectroscopy. *Geochim. Cosmochim. Acta* 67, 156–172.
- Tooth, B., Etschmann, B., Pokrovski, G.S., Testemale, D., Hazemann, J.L., Grondler, P.V., Brugger, J., 2013. Bismuth speciation in hydrothermal fluids: an X-ray absorption spectroscopy and solubility study. *Geochim. Cosmochim. Acta* 101, 156–172.
- Vaughan, D.J., Craig, J.R., 1997. Sulfide ore mineral stabilities, morphologies, and intergrowth textures. In: Barnes, H.L. (Ed.), *Geochemistry of Hydrothermal Ore Deposits*, Third Edition. John Wiley & Sons, Inc., pp. 367–434.
- Von Damm, K.L., 1990. Seafloor hydrothermal activity: black smoker chemistry and chimneys. *Annu. Rev. Earth Planet. Sci.* 18, 173–204.
- Von Damm, K.L., Edmond, J.M., Grant, B., Measures, C.I., Walden, B., Weiss, R.F., 1985. Chemistry of submarine hydrothermal solutions at 21°N, East Pacific Rise. *Geochim. Cosmochim. Acta* 49, 2197–2220.
- Wang, Y., Han, X.H., Petersen, S., Frische, M., Qiu, Z., Li, H., Wu, Z., Cui, R., 2017. Mineralogy and trace element geochemistry of sulfide minerals from the Wocan Hydrothermal Field on the slow-spreading Carlsberg Ridge, Indian Ocean. *Ore Geol. Rev.* 84, 1–19.
- Wersin, P., Hochella Jr., M.F., Perrson, P., Redden, G., Leckie, J.O., Harris, D.W., 1994. Interaction between aqueous uranium (VI) and sulphide minerals: spectroscopic evidence for sorption and reduction. *Geochim. Cosmochim. Acta* 58, 2829–2844.
- Wesolowski, D.J., Ziemniak, S.E., Anovitz, L.M., Machesky, M.L., Benezeth, P., Palmer, D.A., 2004. Solubility and surface adsorption characteristics of metal oxides. In: Palmer, D.A., Fernandez-Prini, R., Harvey, A.H. (Eds.), *Aqueous Systems at Elevated Temperatures and Pressures: Physical Chemistry in Water, Steam and Hydrothermal Systems*. Elsevier, Amsterdam, pp. 493–595.
- Widlar, A., Seward, T.M., 2002. The adsorption of hydrosulphide complexes of gold(I) onto iron sulphide substrates. *Geochim. Cosmochim. Acta* 66, 85–92.
- Williams-Jones, A.E., Migdisov, A.A., 2014. Experimental constraints on the transport and deposition of metals in ore-forming hydrothermal systems. *Economic Geology Special Publication* 18, 77–95.
- Wise, A.S., Watters, R.L., 2012. Certificate of Analysis, Standard Reference Material 610. National Institute of Standards and Technology. <http://www.nist.gov/srm>.



- Wohlgemuth-Ueberwasser, C.C., Ballhaus, C., Berndt, J., Stotter, V., Meisel, T., 2007. Synthesis of PGE sulfide standards for laser ablation inductively coupled plasma mass spectrometry (LA-ICP-MS). *Contrib. Mineral. Petrol.* 154, 607–617.
- Wohlgemuth-Ueberwasser, C.C., McClung, C.R., Viljoen, F., 2014. Metamorphic alteration of the massive sulfide horizon from the Salt River VMS deposit (South Africa). *Ore Geol. Rev.* 56, 45–52.
- Wohlgemuth-Ueberwasser, Viljoen, F., Petersen, S., Vorster, C., 2015. Distribution and solubility limits of hydrothermal black smoker sulfides: an in-situ LA-ICP-MS study. *Geochim. Cosmochim. Acta* 159, 16–41.
- Wood, S.A., Samson, I.M., 1998. Solubility of ore minerals and complexation of ore metals in hydrothermal solutions. *Rev. Econ. Geol.* 10, 33–80.
- Wood, S.A., Samson, I.M., 2006. The aqueous geochemistry of gallium, germanium, indium and scandium. *Ore Geol. Rev.* 28, 57–102.
- Wu, Z., Sun, X., Xu, H., Konishi, H., Wang, Y., Wang, C., Dai, Y., Deng, X., Yu, M., 2016. Occurrences and distribution of ‘invisible’ precious metals in sulfide deposits from the Edmond hydrothermal field, Central Indian Ridge. *Ore Geol. Rev.* 79, 105–132.
- Yamamoto, M., Kase, K., Tsutsumi, M., 1984. Fractionation of sulfur isotopes and selenium between coexisting sulfide minerals from the Besshi deposit, Central Shikoku, Japan. *Mineral. Deposita* 19, 237–242.
- Ye, L., Cook, N.J., Ciobanu, C.L., Yuping, L., Qian, Z., Tiegeng, L., Wei, G., Yulong, Y., Danyushevsky, L., 2011. Trace and minor elements in sphalerite from base metal deposits in South China: a LA-ICP-MS study. *Ore Geol. Rev.* 39, 188–217.
- Yuan, B., Hongjun, Y., Yang, Y., Zhao, Y., Yang, J., Xu, Y., Lin, Z., Tang, X., 2018. Zone refinement related to the mineralization process as evidenced by mineralogy and element geochemistry in a chimney fragment from the Southwest Indian Ridge at 49.6°E. *Chem. Geol.* 482, 46–60.
- Zonenshain, L.P., Kuzmin, M.I., Lisitsin, A.P., Bogdanov, Y.A., Baranov, B.V., 1989. Tectonics of the Mid-Atlantic rift valley between the TAG and MARK areas (26–24°N): evidence for vertical tectonism. *Tectonophysics* 159, 1–23.